

## BIROn - Birkbeck Institutional Research Online

---

Enabling Open Access to Birkbeck's Research Degree output

### Spectroscopic tools for the study of voltage gated sodium channel structure, function and ligand binding

<https://eprints.bbk.ac.uk/id/eprint/45073/>

Version: Full Version

**Citation: Colledge, Matthew (2021) Spectroscopic tools for the study of voltage gated sodium channel structure, function and ligand binding. [Thesis] (Unpublished)**

© 2020 The Author(s)

---

All material available through BIROn is protected by intellectual property law, including copyright law.

Any use made of the contents should comply with the relevant law.

---

# **Spectroscopic tools for the study of voltage gated sodium channel structure, function and ligand binding**

---

*Matthew Colledge*

*Biological Sciences PhD thesis*

*Birkbeck, University of London*

## **Declaration of Authenticity of Work**

The work herein presented is the work of candidate, except where otherwise specified.  
Signed:

# Abstract

---

As the proteins responsible for the initiation and propagation of the action potential in excitable cells, voltage-gated sodium channels ( $\text{Na}_v\text{s}$ ) are crucial drug targets. Antiarrhythmics, anaesthetics, and antiepileptic drugs all target  $\text{Na}_v\text{s}$ . Yet despite the difference in  $\text{Na}_v$  subtypes affecting these diseases, the drugs used to treat them are able to act while showing little subtype specificity. This is explained by drugs displaying state-dependant binding and kinetics. Hence an understanding of the structural changes in different gating states of  $\text{Na}_v\text{s}$  is vital for structure-based drug design, of more effective and selective compounds. To date there is no atomic-resolution structure of a functional eukaryotic  $\text{Na}_v$ , although the structures of several prokaryotic  $\text{Na}_v\text{s}$  which share pharmacological characteristics with their eukaryotic counterparts have been determined. However these structures are in variety of conformations and the relationships between them remain unclear.

This study presents biophysical techniques complementary to structural ones to investigate the gating of  $\text{Na}_v\text{s}$ , using the channel from *Magnetococcus Marinus* ( $\text{Na}_v\text{Ms}$ ) as a case study. Oriented circular dichroism (oCD) spectroscopy is used to report on the orientation of the pore-lining  $\alpha$ -helices within the membrane, based on quantitative analysis of oCD data. Single molecule FRET spectroscopy is able to measure interatomic distances across biological molecules, and here is used to investigate the changes in pore diameter at the gate of  $\text{Na}_v\text{Ms}$ . Also presented is a new web-based application which uses protein structure files to define the orientation of  $\alpha$ -helices that comprise the channel.

# Acknowledgements

---

I would like to thank the friends and colleagues who have made this process easier and more enjoyable.

Claire Bagn ris and Emily McCusker for providing the initial Na<sub>v</sub>Ms constructs and advice in protein purification. Andrew Miles for his help, instruction and company in CD data collection. Lee Whitmore for his guidance in web-tool design. Benjamin Coles of the STFC for setting up and assisting with FRET measurements. Timothy Craggs of Oxford University for advice in sample preparation for FRET measurements.

The whole of the Wallace group especially Alex Henderson, Altin Sula, Elliot Drew, Giulia Montini and Jenny Booker for their companionship and friendship throughout the past four years.

My flatmates: Adriana, Charles, Freya, Francesco, Giulia, Ian, Michaela, Sarah and Sophia; from the past four years for ensuring I remembered to sleep and, eat, drink and laugh. My parents for their support and, putting up with me writing this under their feet. The rest of my friends for providing such welcome and enjoyable distractions.

My Clouds for keeping me going through the anxiety of editing this.

Ellis James, John Robbins, Matt Lees, Paul Dean and Quintin Smith for producing excellent podcasts with uplifting conversation, which made the longer hours in the lab feel shorter. Fortuna pop! for releasing music to walk to work to.

But most of all I would like to thank Professor Bonnie Wallace for giving me this opportunity and her excellent guidance and support throughout.

# Table of contents

---

Abstract.....	3
Acknowledgements.....	4
Table of contents .....	5
List of figures.....	7
List of abbreviations.....	10
Introduction to voltage-gated sodium channels.....	11
Voltage-gated sodium channels in eukaryotes.....	11
Prokaryotic Na <sub>v</sub> s as a model system.....	17
The Na <sub>v</sub> voltage sensor.....	21
The selectivity filter of prokaryotic Na <sub>v</sub> s.....	26
The Na <sub>v</sub> ion conducting pore and gating .....	33
The C-terminal coiled coil of prokaryotic Na <sub>v</sub> s .....	38
Na <sub>v</sub> ligand binding .....	40
Outlook .....	43
AnglerFish: a tool for defining the orientation of $\alpha$ -helical pores .....	45
Introduction .....	45
Methods.....	45
Definitions.....	45
Calculations.....	48
User interface.....	52
Results.....	52
Identifying the kinked helix in the NaK channel .....	52
Comparison of open and closed GLIC structures.....	55
Prokaryotic voltage-gated sodium channels.....	57
Conclusions .....	59
Expression and purification of Na <sub>v</sub> Ms constructs.....	60
Introduction to techniques .....	60
Materials and Methods.....	62
Results.....	64
Oriented circular dichroism spectroscopy of Na <sub>v</sub> Ms.....	77

Introduction to circular dichroism spectroscopy.....	77
Circular dichroism spectroscopy.....	77
Oriented circular dichroism (oCD) .....	81
Possible sources of error in oriented circular dichroism .....	84
oCD analysis of Na <sub>v</sub> Ms .....	88
Methods.....	88
Sample preparation .....	88
Film formation .....	89
Data collection .....	89
Results.....	90
Choice of support material .....	90
Buffer and concentration.....	90
Bilayer formation is non-denaturing.....	93
There is little effect from LD or LB and Films do not alter during data collection.....	95
The process of bilayer formation orients Na <sub>v</sub> Ms.....	97
Screening ligands for binding.....	99
Binding of veratridine to the Na <sub>v</sub> Ms pore .....	104
Binding of general anaesthetics to the Na <sub>v</sub> Ms pore.....	107
Quantitative analysis of oSRCD data.....	109
Oriented reference spectra for membrane proteins.....	112
Discussion.....	124
Single molecule FRET studies of Na <sub>v</sub> Ms.....	126
Introduction to smFRET .....	126
Methods.....	131
Labelling .....	131
Data collection .....	132
Data Processing.....	133
Results.....	134
Discussion.....	142
Conclusions and Future Work.....	148
Appendices.....	151
Bibliography .....	156

# List of figures

---

Introduction to voltage-gated sodium channels.....	11
Figure 1. Schematic comparison of eukaryotic and prokaryotic Na <sub>v</sub> s.....	13
Figure 2. A table of mammalian NaV isoform distribution and disease association.....	15
Figure 3. The Cryo-EM structure of the NaV from <i>Periplaneta americana</i> .....	18
Figure 4. Crystal structures from the prokaryotic NaVs .....	20
Figure 6. Alignment of prokaryotic Na <sub>v</sub> sequences .....	27
Figure 7. Structure of the Selectivity filter of Na <sub>v</sub> Ab .....	29
Figure 8. The selectivity filters of the NaVAb wildtype and I221C mutant, and NaVRh.....	32
Figure 9. A cross section through the Na <sub>v</sub> Ms pore.....	34
Figure 10. Comparison of the fenestrations of Na <sub>v</sub> Ab and Na <sub>v</sub> Ms.....	34
Figure 11. Superposition of Na <sub>v</sub> Ab and KV1.2 .....	35
Figure 12. Diagram of the proposed role of the linker and C-terminal coiled coil in gating .....	39
AnglerFish: a tool for defining the orientation of $\alpha$ -helical pores .....	45
Figure 1. The definitions of tilt and swing used in AnglerFish .....	47
Figure 2. The calculation of the pore axis by cross product .....	49
Figure 3. Calculation of the vectors required for swing determination .....	51
Figure 4. Anglerfish used to investigate the kinking of the pore helix of the NaK channel.....	54
Figure 5. Anglerfish used to investigate the gating of the GLIC ion channel.....	56
Figure 6. Anglerfish used to compare the asymmetric and symmetric NaVMs pore structures .....	58
Expression and purification of Na <sub>v</sub> Ms constructs.....	60
Figure 1. An example purification of the Na <sub>v</sub> Ms pore .....	68
Figure 2. An example purification of the Na <sub>v</sub> Ms pore A221C mutation.....	71
Figure 3. Identification of the full length NaVMs by mass spectrometry.....	73
Figure 4. The purification of the NaVMs full length A221C mutation .....	76
Oriented circular dichroism spectroscopy of Na <sub>v</sub> Ms.....	77
Figure 2. The electronic transitions that give rise to circular dichroism.....	83
Figure 3. A typical experimental set up for oCD data collection .....	85
Figure 4. The effect of buffer conditions on oCD spectra of Na <sub>v</sub> Ms.....	92
Figure 5. The CD spectra of a resolubilised Na <sub>v</sub> Ms film.....	94
Figure 6. CD spectra of oriented Na <sub>v</sub> Ms films at different rotations around the beam axis.....	96

Figure 7. CD spectra Na <sub>v</sub> Ms pore films dried from a Cymal-5 detergent solution .....	98
Figure 9. oCD spectra of The Na <sub>v</sub> Ms pore bound to different ligands .....	102
Figure 10. 228/210 nm peak ratios for the oCD spectra of the Na <sub>v</sub> Ms pore.....	103
Figure 11. The effect of veratridine binding on the oCD spectra of Na <sub>v</sub> Ms .....	105
Figure 12. 228/210 peak ratios shown for the oCD spectra of the Na <sub>v</sub> Ms pore alone and in the presence of veratridine.....	106
Figure 13. The effect of isoflurane incubation on oCD spectra of Na <sub>v</sub> Ms .....	108
Figure 14. Theoretical CD spectra for alpha helices parallel and perpendicular to the beam .....	110
Figure 15. Theoretical CD spectra for alpha helices parallel and perpendicular to the beam based on the SMP180 dataset.....	114
Figure 16. The angle of theoretical spectra generated by different reference data which best fit experimental spectra .....	116
Figure 17. Example fits of theoretical spectra generated from the DeJongh and SMP180 data sets to experimental.....	117
Figure 18. The angle of theoretical spectra which best fit experimental spectra in the presence of different ligands.....	119
Figure 19. The angle of theoretical spectra that best fits experimental data with an isotropic spectrum included .....	120
Figure 20. Fits of theoretical oCD spectra to oCD spectra of the Na <sub>v</sub> Ms pore before and after incubation with isoflurane .....	121
Figure 21. Tilt values expected from prokaryotic Na <sub>v</sub> crystal structures.....	123
Single molecule FRET studies of Na <sub>v</sub> Ms.....	126
Figure 1. UV-Visible absorbance spectra of the dye bound Na <sub>v</sub> Ms pore 221C .....	135
Figure 2. Atomic structures of FRET dyes .....	135
Figure 3. Fluorescence gels of the dye bound Na <sub>v</sub> Ms pore A221C.....	137
Figure 5. FRET efficiency stoichiometry plots for the Na <sub>v</sub> Ms pore A221C labelled separately with Cy3B and Atto647N.....	139
Figure 6. FRET data from DNA standards.....	140
Figure 7. Corrected FRET efficiency stoichiometry plots for Na <sub>v</sub> Ms.....	141
Figure 8. examples of raw photon bursts from fluorescently labelled Na <sub>v</sub> Ms .....	141
Figure 9. Simulated accessible volumes simulated for dyes conjugated to the Na <sub>v</sub> Ms pore.....	144
Figure 10. The conjugation position of the full length Na <sub>v</sub> Ms .....	147

Appendices.....	151
Appendix 1. Plasmid map of pET-15b .....	151
Appendix 2. NaVMs gene sequences.....	152
Appendix 3. Na <sub>v</sub> Ms constructs protein sequences.....	153
Appendix 3. Size exclusion chromatography standards .....	154
Appendix 5. Peak parameters for oCD ligand binding experiments.....	155

# List of abbreviations

---

A5BBZ	2-amino-5-bromo benzothiazole
AFM	Atomic Force Microscopy
Ca <sub>v</sub>	Voltage gated calcium channel
CD	Circular Dichroism
Cmc	Critical micelle concentration
Cryo-EM	Cryo Electron Microscopy
CTD	C-terminal domain
DDM	n-Dodecyl β-D-Maltopyranoside
DDT	Dithiothreitol
DMSO	Dimethyl sulfoxide
FRET	Förster resonance energy transfer
GLIC	gloeobacter ligand-gated ion channel
K <sub>v</sub>	Voltage gated potassium channel
LB	Linear birefringance
LD	Linear dichroism
NaChBac	Voltage gated sodium channel from <i>Bacillus halodurans</i>
Na <sub>v</sub>	Voltage gated sodium channel
Na <sub>v</sub> Ab	Voltage gated sodium channel from <i>Arcobacter butzleri</i>
Na <sub>v</sub> Ae1	Voltage gated sodium channel from <i>Alkalilimnicola ehrlichei</i>
Na <sub>v</sub> Ms	Voltage gated sodium channel from <i>Magnetococcus marinus</i>
Na <sub>v</sub> Rh	Voltage gated sodium channel from <i>Rickettsiales sp.</i>
NMR	Nuclear magnetic resonance
oCD	Oriented circular dichroism
oSRCD	Oriented synchrotron radiation circular dichroism
PAGE	Poly acrylamide gel electrophoresis
PCR	Polymerase chain reaction
POPE	1-palmitoyl-2-oleoyl-sn-glycero-3-phosphoethanolamine
POPG	1-palmitoyl-2-oleoyl-sn-glycero-3-phosphoglycerol
R <sub>0</sub>	Förster radius
SDS	Sodium dodecyl sulfate
smFRET	Single molecule Förster resonance energy transfer
SRCD	synchrotron radiation circular dichroism
TBS	Tris buffered saline
TIRF	Total internal reflection fluorescence
VSD	Voltage sensing domain

# Introduction to voltage-gated sodium channels

---

## Voltage-gated sodium channels in eukaryotes

The nervous system functions by the transmission of high frequency impulses along neurones ending in synapses which in turn are able to activate further neurones and other excitable cells. Neurones are able to propagate high frequency impulses via a membrane depolarisation travelling along the length of the cell. The membranes of excitable cells in muscle and the endocrine system are also able to depolarise as a signalling mechanism in response to nerve impulses. In a 'resting' cell the membrane is polarised by a potential of -70 mV created by a high concentration of extracellular  $\text{Na}^+$  ions maintained by  $\text{Na}^+/\text{K}^+$  ATPases that export 3  $\text{Na}^+$  ions for every 2  $\text{K}^+$  ions (Hille, 2001). The propagation of membrane depolarisation is made possible by voltage-gated sodium channels ( $\text{Na}_v\text{s}$ ), which open when the membrane potential drops below a threshold. This voltage-dependant activation allows  $\text{Na}^+$  ions to rapidly flow down their concentration and electrostatic gradients further depolarising the membrane, causing more  $\text{Na}_v\text{s}$  to open. This results in a positive membrane potential that is counteracted by the opening of voltage-gated potassium channels ( $\text{K}_v\text{s}$ ) followed by a refractory period where the membrane cannot be depolarised while the resting potential is re-established. The refractory period allows the propagation of the action potential to be unidirectional and is a consequence of the  $\text{Na}_v$  becoming inactive milliseconds after activation (Hille, 2001).

The features of the action potential were defined by measuring the electric potential of the axon of a giant squid at various  $\text{Na}^+$  and  $\text{K}^+$  concentrations long before the ion channels themselves were identified (Hodgkin and Huxley, 1952). The model produced from these experiments showed that the  $\text{Na}^+$  channel (termed carrier then) would have to be highly selective, activate in response to a change in membrane potential and subsequently inactivate on a millisecond timescale.

Isolated  $\text{Na}_v\text{s}$  from rat brain were shown to be composed of a 250 kDa  $\alpha$  subunit and one or more accessory 35 kDa  $\beta$  subunits (Beneski and Catterall, 1980). cDNA cloning and expression of the channels from the electric eel showed that the  $\alpha$  subunit alone is sufficient for ion conductance and gating (Noda et al., 1986), while the  $\beta$  subunit modulates the voltage dependence and inactivation rate of the channel (Isom et al., 1992). The  $\alpha$  subunits (hereafter referred to as eukaryotic  $\text{Na}_v\text{s}$ ) are

composed of 4 pseudo-repeats referred to as domains as seen in figure 1a. Each domain consists of 6 transmembrane helices termed S1-S6 of which S1-S4 form a voltage sensor domain (VSD) located on the periphery of the protein while S5 and S6 form the ion conducting pore the arrangement of which is shown diagrammatically in figure 1c (*Catterall, 2000*).

Na<sub>v</sub>s are members of the voltage-gated ion channel superfamily, a large family of related eukaryotic signal transduction proteins (*Yu et al., 2005*). This family includes the voltage gates calcium (Ca<sub>v</sub>s) and K<sub>v</sub>s which share a common topology with Na<sub>v</sub>s, but K<sub>v</sub>s consist of a single domain poly peptide which forms a homotetramer (*Hille, 2001*). The family also contains ion channels which activate in response to ligand binding rather than depolarisation such as the cyclic-nucleotide gated and transit receptor potential channels; these channels, like the K<sub>v</sub>s, are tetramers but the S1-S4 has lost the ability to change in response to changes in membrane potential (*Yu et al., 2005; Clayton et al., 2008*). Smaller channels such as the potassium conducting K<sub>ir</sub> and K<sub>2p</sub> which consist of 1 and 2 repeats of S5-S6 respectively and assemble to form pore-only proteins are also found within the family (*Yu et al., 2005*).

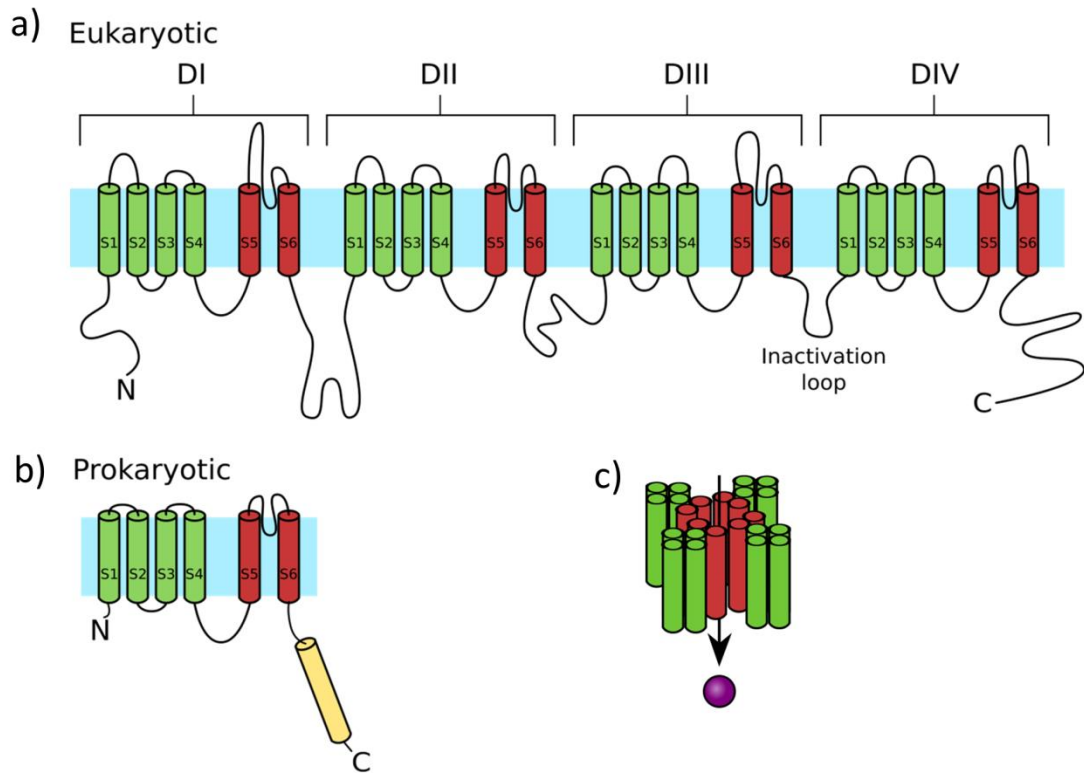


**Figure 1. Schematic comparison of eukaryotic and prokaryotic  $Na_vS$  Helices** (labelled S1-S6) are shown as coloured cylinders and the extent of the membrane in blue, with the extracellular side on top for a) an entire eukaryotic  $Na_v$  and b) a single monomer of a prokaryotic  $Na_v$ . Helices of the voltage sensing domain are coloured green, the pore red and the C-terminal prokaryotic helix yellow. The 3D arrangement of these helices within a membrane is shown in c).

In mammals at least 9 distinct Na<sub>v</sub> isoforms termed Na<sub>v</sub>1.1- Na<sub>v</sub>1.9 are present in the membranes of excitable cells and are differentially expressed in different tissues, their tissue distribution and disease associations are summarised in figure 2 (Yu *et al.*, 2003). Due to their fundamental role in action potential generation, mutations in Na<sub>v</sub>s contribute to a variety of diseases associated with excitable cells. As Na<sub>v</sub>1.5 is the predominant isoform found in cardiac muscle, responsible for the rapid upstroke in action potential require for contraction, it is not surprising there are a variety of cardiac arrhythmias associated with Na<sub>v</sub>1.5 mutation (Zimmer and Surber, 2008). Both gain-of-function and loss-of-function mutations in the gene for Na<sub>v</sub>1.1 are found to be determinants of hereditary epilepsy (Mulley *et al.*, 2005), while mutations in Na<sub>v</sub>1.2 lead to a milder form of childhood epilepsy (Misra *et al.*, 2008). Na<sub>v</sub>1.1 deletion is shown to reduce current density in some rat hippocampal interneurons (Yu *et al.*, 2006), this is believed to lead to aberrant patterns of neuronal firing depending on whether the interneurons affected are excitatory or inhibitory and if other Na<sub>v</sub> isotypes are able to compensate (Ragsdale, 2008). Na<sub>v</sub>1.7, 1.8 and 1.9 are expressed in the cells of the peripheral nervous system involved in pain signalling. Na<sub>v</sub>1.8 carries the majority of the current in the cells in which it is expressed so is largely responsible for the transmission of pain signals to the central nervous system (Wood, *et al.*, 2004). Na<sub>v</sub>1.7 is predominantly expressed in sensory neurones and thought to initiate the pain signals propagated by Na<sub>v</sub>1.8 (Wood *et al.*, 2004). This is supported by the discovery of loss-of-function mutations in Na<sub>v</sub>1.7 which lead to pain insensitivity (Goldberg *et al.*, 2007) and gain-of-function mutations associated with pain hypersensitivity which increase the Na<sup>+</sup> current from Na<sub>v</sub>1.7 and reduce the depolarisation required for activation (England and de Groot, 2009). However it is important to note the role of different Na<sub>v</sub> isotypes in pain signalling is complicated by the fact that their expression profiles are altered in during neuropathy and inflammation (Dib-Hajj *et al.*, 2009). The differential features of these isotypes could be used to more effectively guide the treatment of pain by targeting isotypes associated with different pathologies.

<b>Na<sub>v</sub> isotype</b>	<b>Tissue Distribution</b>	<b>Diseases Associated With Channelopathies</b>
<b>1.1</b>	Central nervous system	epilepsy
<b>1.2</b>	Central nervous system Peripheral nervous system	epilepsy
<b>1.3</b>	Central nervous system Peripheral nervous system Cardiac muscle	Epilepsy
<b>1.4</b>	Skeletal muscle	Periodic paralysis
<b>1.5</b>	Cardiac muscle Central nervous system	Cardiac arrhythmia
<b>1.6</b>	Central nervous system Peripheral nervous system	Epilepsy Cognitive impairment
<b>1.7</b>	Peripheral nervous system	Pain insensitivity Pain hypersensitivity
<b>1.8</b>	Peripheral nervous system	Pain insensitivity
<b>1.9</b>	Peripheral nervous system	Pain hypersensitivity

**Figure 2. A table of mammalian NaV isoform distribution and disease association.** *The information was compiled and summarised from Huang et al. 2017; Yu and Catterall 2003; and Kim 2014*

As a result of their physiological roles  $\text{Na}_v\text{s}$  are pharmacologically important as targets for drugs treating epilepsy, arrhythmia, analgesics for relieving the effects of chronic pain disorders and anaesthetics used during surgical procedures. For example, lidocaine acts as both a local anaesthetic and antiarrhythmic by binding to  $\text{Na}_v\text{s}$ , inhibiting sodium currents (*Chernoff et al., 1990*). Lamotrigine, an anticonvulsant important in the treatment of epilepsy also targets  $\text{Na}_v\text{s}$  (*Kuo and Lu, 1997*), however around 30% of epilepsy patients are unaffected by treatment with anticonvulsants (*Hemming et al., 2013*). This highlights the need for a more detailed understanding of their mechanism at the molecular level.  $\text{Na}_v\text{s}$  are also blocked off target as a side effect of the antidepressant amitriptyline (*Dick et al., 2007*), overdose of which leads to ECG traces indicative of arrhythmias seen in patients with mutations in  $\text{Na}_v1.5$  (*Akhtar and Goldschlager, 2006*). This highlights the importance of identifying interactions of future ion channel targeting drugs with different  $\text{Na}_v$  isoforms. Given the range of different pathologies associated with different isoforms it seems surprising that most drugs targeting  $\text{Na}_v\text{s}$  show little subtype specificity yet can be used to treat individual conditions, without significantly perturbing the other processes involving  $\text{Na}_v\text{s}$ . This is explained by an increased affinity of small molecule drugs for the inactive and open forms of the channel and hence will bind most efficiently to subtypes that are firing rapidly and spending the most time in these conformations (*Chernoff, 1990*). The kinetics of drug binding can also help guide preferential inhibition of aberrantly firing channels; for example lamotrigine binds to the inactivated state but with an on rate slower than the fast inactivation process (*Kuo and Lu, 1997*) so lamotrigine requires a prolonged membrane depolarisation to take effect. Prolonged depolarisations are rare in healthy neurons but common during epileptic seizures causing preferential action of lamotrigine in the neurons involved (*DeCurtis and Avanzini, 2001, England and de Groot, 2009*).

$\text{Na}_v\text{s}$  are of further importance as the targets of different classes of insecticides including organochlorines such as DDT, and pyrethroids such as deltamethrin (*Field, et al., 2017*). The use of organometallics in agriculture faded due to their toxicity towards non pest species and mammals raising concerns of environmental damage and food safety (*Field, et al., 2017*). In recent years many species have developed resistance to pyrethroids leading to their decreased use in favour of neonicotinoids which target completely different channels. Both of these effects can be explained by differences in the amino acid compositions of  $\text{Na}_v\text{s}$  leading to decreased insecticide binding (*Rinkevich, et al., 2013; O'Reilly, et al., 2006*).

## Prokaryotic Na<sub>v</sub>s as a model system

Due to their large size and complexity as yet it has not been possible for a functional eukaryotic Na<sub>v</sub> to be expressed at a homogeneity and purity required for high resolution structural characterisation by X-ray diffraction. The only structures of eukaryotic Na<sub>v</sub>s to date have been solved by cryo-electron microscopy (Cryo-EM) namely the channel from the eel *Electrophorus electricus* to a resolution of 19 Å (Sato *et al.*, 2001), and a channel from the cockroach *Periplaneta americana* at 3.8 Å shown in figure 3 (Shen *et al.*, 2017). The former is far too low a resolution to discern the central pore let alone the helices or side chain orientations. As figure 3 shows the backbone of the *Periplaneta Americana* channel fits well into the density however it has failed to yield measurable currents when studied by electrophysiology. Fortuitously smaller voltage-gated sodium channels have been found in bacteria; bacterial Na<sub>v</sub>s share the topological arrangement of their eukaryotic counterparts but are homotetramers like K<sub>v</sub>s (Nurani *et al.*, 2008) with each subunit corresponding to a pseudo-repeat of the eukaryotic protein and contain much shorter extra membranous loops. The first identified prokaryotic Na<sub>v</sub> was from *Bacillus halodurans* which was named NaChBac. Latter channels from other prokaryotes were identified by genome searches for sequences with homology to NaChBac and termed Na<sub>v</sub> followed by 2-3 letter descriptors of the organism (Ren *et al.*, 2001; Koishi *et al.*, 2004).

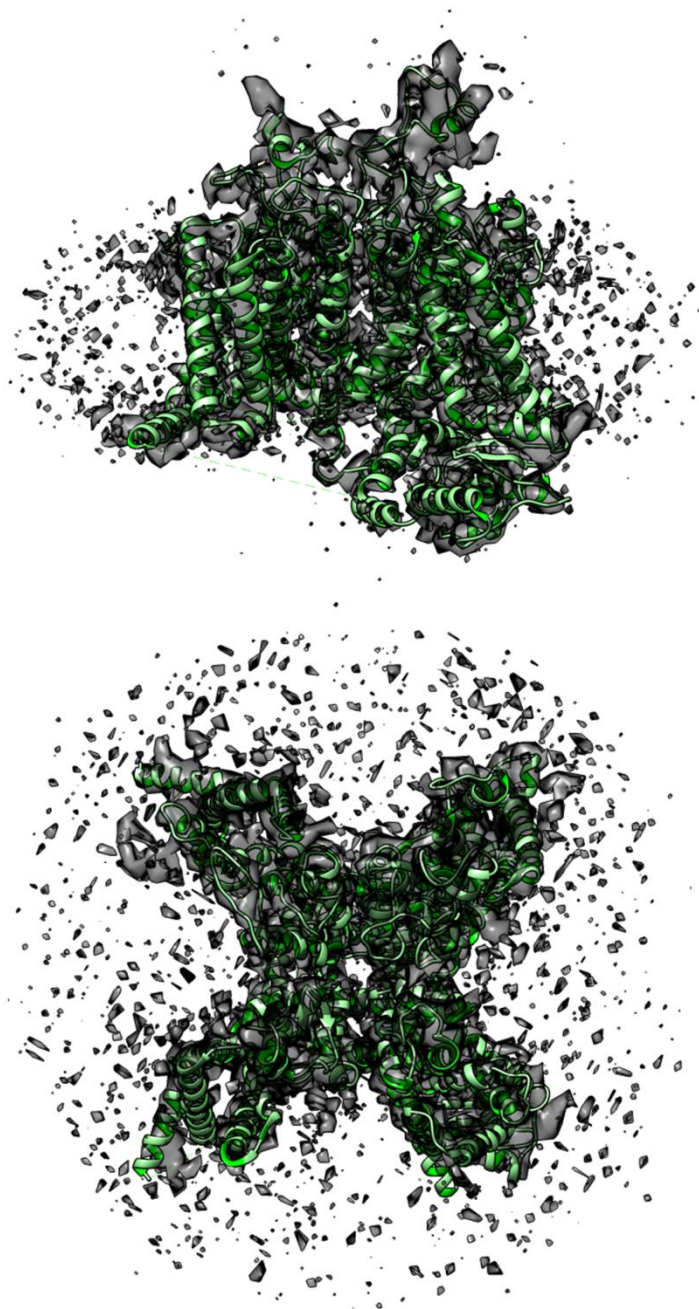


**Figure 3.** The Cryo-EM structure of the NaV from *Periplaneta americana*. The electron density is shown as a translucent grey surface containing the fitted backbone as a green cartoon. A side view with the extracellular surface at the top (top) and a top view looking from the extra cellular side (bottom) are shown. The electron density is shown at a sigma of 0.45 sigma and the data is from PDB 5X0M and EMD-6698.

Prokaryotic Na<sub>v</sub> sequences have a 15-25% sequence identity with their eukaryotic counterparts with the highest similarity in the transmembrane helices, where there is the least variation between the eukaryotic Na<sub>v</sub>s themselves (Koishi et al., 2004; Yu et al., 2003 Charalambous and Wallace, 2011). NaChBac has been successfully expressed in a variety of mammalian cell lines allowing patch clamp measurements of single channels, these include Chinese hamster ovary (Ren et al. 2001), African green monkey kidney (Kuzmenkin et al. 2004) and human embryonic kidney cells (Zhao et al. 2004a). Electrophysiological measurements of NaChBac show it to activate and conduct sodium in response to membrane de-polarisation as expected for a Na<sub>v</sub> but with activation and inactivation kinetics 10-100 times slower than eukaryotic Na<sub>v</sub>s (Ren et al. 2001).

To date the ability to overexpress and purify prokaryotic Na<sub>v</sub>s has enabled the determination of the atomic resolution structures of 4 different channels, namely Na<sub>v</sub>Ab from *Arcobacter butzleri* (Payandeh et al., 2011; 2013), Na<sub>v</sub>Ms from *Magnetococcus marinus* (McCusker et al., 2012; Bagn ris et al. 2013), Na<sub>v</sub>Rh from *Rickettsiales sp. HIMB114* (Zhang et al., 2012) and Na<sub>v</sub>Ae1 from *Alkalilimnicola ehrlichei* (Shaya et al., 2014; Arrigoni, et al., 2016). Figure 4 shows these structures with the S5-S6 section forming a conical central pore (red) surrounded by VSDs (green) in these structures as would be expected by comparison to the eukaryotic K<sub>v</sub> (Long et al. 2007). The structures provide a tantalising insight into the mechanism of Na<sub>v</sub>s as they show a variety of open and closed of the pore with and without voltage sensors attached.

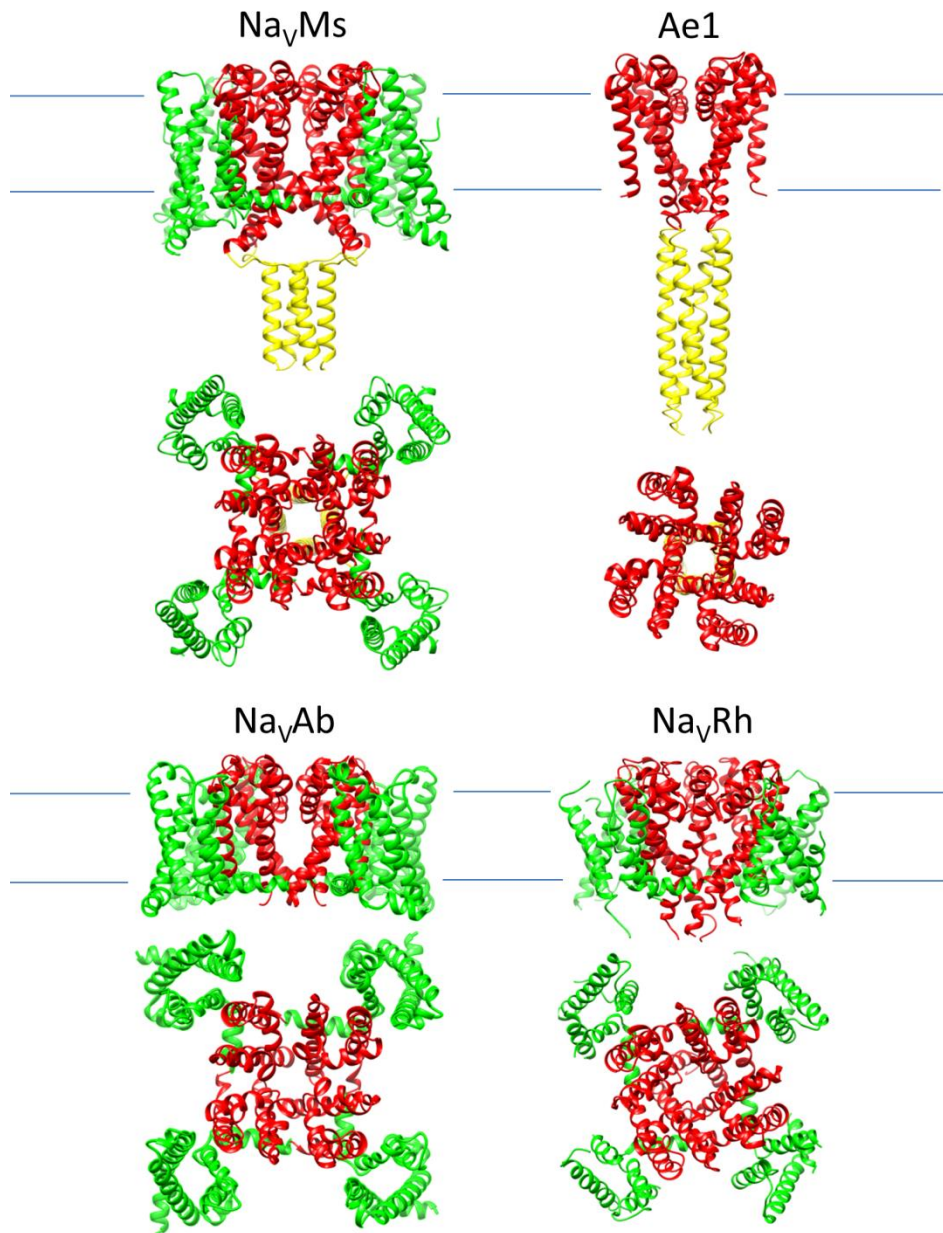


**Figure 4. Crystal structures from the prokaryotic NaVs.** The voltage sensor is shown in green, pore domain red and C-terminal domain yellow. Blue lines show the position of the membrane edges with the cytoplasmic side at the top. Side and top views are shown for each channel

While they have been studied extensively as models for eukaryotic Na<sub>v</sub>s, the physiological role of Na<sub>v</sub>s within prokaryotes is still poorly understood. The organisms prokaryotic Na<sub>v</sub>s have been found in a diverse set of largely alkiliphilic extremeophiles of which only one, *Bacillus pseudofirmus* is genetically accessible (Ito et al., 2004). The Na<sub>v</sub> from *Bacillus pseudofirmus*, Na<sub>v</sub>Bp has been used as the model for native prokaryotic Na<sub>v</sub> function, having been implicated in pH homeostasis and chemotaxis. Mutants with the Na<sub>v</sub>Bp gene deleted are unable to grow at a pH of 10.5 or above in low sodium or at any sodium concentration if the flagellar motor's Na<sup>+</sup> channel component MotPS is also deleted (Ito et al., 2004). Both Na<sub>v</sub>Bp and MotPS are thought to contribute to sodium re-entry as in the Na<sub>v</sub>Bp deletion the mutant can survive in high sodium; this implies in high sodium the sodium electrochemical gradient is high enough for MotPS to work alone. Na<sub>v</sub>Bp deletion mutants also exhibit reverse chemotaxis (i.e. away from chemoattractants) (Ito et al., 2004) and Na<sub>v</sub>Bp's role in chemotaxis is supported by its co-localisation with methyl accepting chemotaxis proteins (Fujinami et al., 2007).

An important difference between mammalian and prokaryotic Na<sub>v</sub>s is the lack of any sequence equivalent to that required for eukaryotic Na<sub>v</sub> fast inactivation. In eukaryotic Na<sub>v</sub>s the peptide sequence IFM in the intracellular loop between domains III and IV has been shown to block the channel, which is able to fold back into the intracellular pore (West et al., 1992). The only extensive intracellular structure in prokaryotic Na<sub>v</sub>s is the C-terminal domain (CTD), which is in an equivalent position to the inter-domain loops of eukaryotic Na<sub>v</sub>s; however this region forms an elongated coiled coil structure (Powell et al., 2010; Shaya et al., 2013) with functions to be discussed later. This is in contrast to the solution NMR structure of the eukaryotic inactivation gate which consists of the IFM peptide held in a rigid conformation by a short  $\alpha$  helix between 2 flexible linkers (Rohl et al., 1999). K<sub>v</sub>s which, like prokaryotic Na<sub>v</sub>s, are homotetramers undergo fast inactivation via their N-terminus which is able to block the pore from the extracellular side (Demo and Yellen, 1991), however no prokaryotic Na<sub>v</sub> has been found with N termini long enough to reach over the VSD into the pore. Hence it stands to reason that loss of conduction in prokaryotic Na<sub>v</sub>s will be due to a structural change analogous to the slow inactivation of their eukaryotic counterparts.

## The Na<sub>v</sub> voltage sensor

The Na<sub>v</sub> voltage sensor is a bundle of 4 helices connected to the pore by the S4-S5 intracellular linker (Payandeh et al., 2011). The mechanism of voltage sensing has been mapped to the movement of 4 positive gating charges, denoted R1-R4, across the membrane (Tao et al., 2010).

Charge movement was first proposed to be the mechanism of the voltage sensor when a 'gating current' was detected as a small capacitance in the membrane of the giant squid axon before the development of a sodium current (*Armstrong and Bezanilla, 1974*). The positive residues in S4 were predicted to be the gating charges from the cDNA sequence of the channel from *Electrophorus electricus* (*Noda et al., 1983*) The movement of which is shown diagrammatically in figure 5. This has since been confirmed by scanning mutagenesis where mutation of these residues to uncharged or negative amino acids reduces the steepness of voltage dependency of activation (*Kontis et al., 1997*).

The movement of S4 has been probed by chemical modification of the positions of the gating charges. The residues being studied were mutated to cysteine, the products of which still produced functional channels but with altered voltage dependence. The reaction of the cysteine side chain with reactive sulfhydryl compounds and hence its solvent accessibility could be monitored by a drastic change in gating kinetics (*Yang and Horn, 1995*). This showed the first charged residue is accessible to the extracellular side only on depolarisation and the last 4 only to intracellular side regardless of membrane potential, indicating S4 shifts up into the membrane on depolarisation (*Yang and Horn, 1995*). Interestingly two positions mutated the middle S4 appear to be accessible to either side depending on membrane polarisation indicating S4 protrudes from the membrane by most of its length (*Yang et al., 1996*). The apparent movement of S4 out of the membrane was explained by the suggestion of a ring of hydrophobic residues that could form an ionic seal within the voltage sensor, along a cavity the S4 helix travels through. This would allow the modifying sulfhydryls to diffuse to the ionic seal from either side but not pass it. This is seen in the highly conserved Ile, phenylalanine and valine residues in S1, S2 and S3, respectively, which form a 'hydrophobic constriction site' in the VSDs of the Na<sub>v</sub>Ab crystal structure (*Payandeh et al., 2011*). The role of the hydrophobic constriction site in forming an ionic seal within the VSD is supported by mutational studies where the replacement of gating charges or the residues of the hydrophobic constriction site with smaller residues caused ion leakage through the channel (*Tombola and Isacoff, 2005; Tombola et al., 2007*).

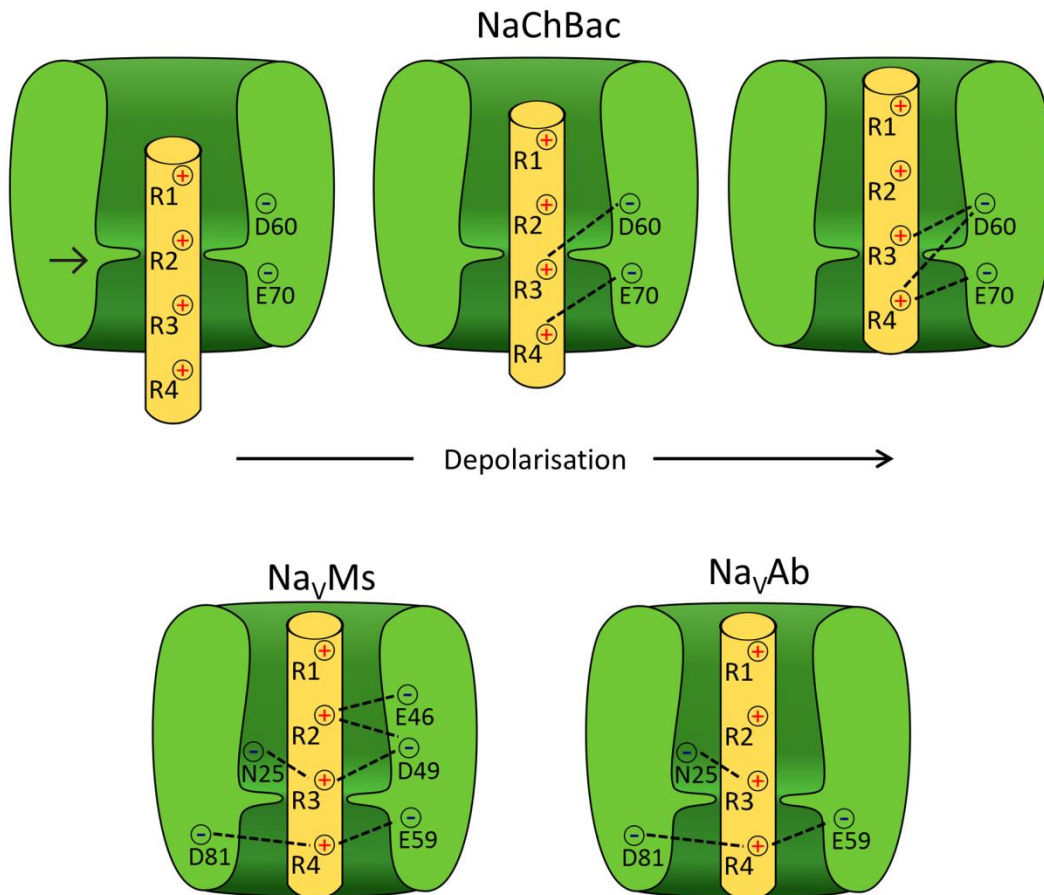


**Figure 5. Schematic diagram of the proposed movement of the S4 helix during depolarisation.** S4 is coloured yellow with the rest of the voltage sensing domain in green, gating charges are shown by red crosses and stabilising charges as blue dashes. The arrow points to the hydrophobic constriction site. The associations defined by disulphide cross linking in NaChBac are shown (top) while the salt bridges seen in the NaVMs and NaVAb crystal structures are shown (bottom) as dashed lines.

The gating charges of S4 are stabilised by interaction with negative residues in S2. This was first seen in the VSD of the Shaker K<sub>v</sub> channel where removal or reversal of the gating charges prevented the protein from being functionally expressed, seemingly due to misfolding (*Papazian et al., 1995*). The functional expression of mutants with reversed charges in S4 could then be rescued by creating double mutants with the charges of glutamate and aspartate residues in S2 also reversed (*Papazian et al., 1995; Tiwari-Woodruff et al., 2000*). This supports the idea that the energetic cost of burying the gating charges within the hydrophobic membrane environment is overcome by ion-pair formation with neighbouring helices. The movement of S4 is proposed to be achieved by sequential formation and breakage of these ion pairs (*Catterall et al., 2010*). This has been studied extensively in NaChBac by the disulphide bonding of mutants which substitute cysteine for R3, R4 and their ion pair partners D60 and E70 (*DeCean et al., 2008; 2009; 2010*). The formation of disulphide bonds provide high resolution information on the proximity of residues over time as the sulphur atoms must come within 2 Å of each other for the bond to form and this occurs on a millisecond timescale. These experiments showed R3 to come into contact with D60 on depolarisation and R4 to sequentially come into contact with E70 then D60. This was with a time course consistent with R4 forming an ion pair with E70 while R3 is paired with D60 and is summarised in figure 5.

While it is clear the voltage sensor functions by a shift of S4 across the membrane the nature of this shift is still uncertain. This is because all structures of the voltage sensor are in the active conformation, as would be expected given they are generated from protein crystals grown in the absence of an electric field (*Payandeh et al., 2011; 2012; Zhang et al., 2012; Sula, et al., 2017*). The conformation of the Na<sub>v</sub>Ab voltage sensor is however complicated by the fact it is connected to a closed pore, this has led it to be classified as a 'pre-open' state of the channel. The Na<sub>v</sub>Ab S4 helix differs by an RMSD of 1.6 Å to that from the VSD of Na<sub>v</sub>Ms which is in a fully activated conformation with respect to both the VSDs and pore domain schemes of the salt bridges seen in these crystal structures are shown in figure 5 (*Sula, et al., 2017*). The R3 and R4 gating charges form salt bridges to the same residues in both the Na<sub>v</sub>Ms and Na<sub>v</sub>Ab structures namely N25 to R3, and E59 and D81 to R4. However they differ in that the Na<sub>v</sub>Ms R3 also forms a salt bridge with D49 which is absent from the Na<sub>v</sub>Ab sequence. The R2 of Na<sub>v</sub>Ab does not form any salt bridges but hydrogen bonds to a backbone carbonyl from S3, while the R2 of Na<sub>v</sub>Ms forms salt bridges to both D49 and E46 (which is also absent from the Ab sequence) (*Sula, et al., 2017*). It should also be noted that 'the movement of S4' could be misleading as all of the gating charges are residues with positive charges at the end of long amino acid side chains so it is entirely possible for these charges to move with minimal movement from the backbone of S4. This highlights the challenge of discerning whether differences

in conformation of bacterial Na<sub>v</sub>s structures are due to their amino acid composition or crystallisation conditions.

There have been multiple attempts to model the structural transition of the NaChBac VSD (*Shafir et al., 2008; Yarov-Yarovoy et al., 2012; Vargas et al., 2012*). The Yarov-Yarovoy model used alignments of NaChBac with the VSDs in the structures of Na<sub>v</sub>Ab, the potassium channel K<sub>v</sub>AP and a chimeric K<sub>v</sub>1.2 potassium channel containing the S3-S4 linker from K<sub>v</sub>2.1 to model the activated state. The the MlotK1 closed structure was used to model the resting state. Restraints were included based on the ion pair disulphide locking experiments. MlotK1 is a prokaryotic cyclic nucleotide gated channel where the helices S1-S4 no longer function as a VSD but are predicted to adopt a conformation analogous to the resting VSD of voltage-gated ion channels. This is thought to be to keep the channel open while the C-terminal cyclic nucleotide binding domain mediates gating (*Clayton et al., 2008; Yarov-Yarovoy et al., 2012*). While the MlotK1 structure may provide useful restraints to show the conformations possible in a VSD; it should be noted the structure shows a much greater degree of association between the S1-S4 bundle and the pore than is seen in any of the voltage-gated ion channel structures shedding doubt on how applicable it is (*Clayton et al., 2008*). Other attempts to model the resting state have involved simulating hyperpolarised membranes by applying a strong electric field to the simulation so that the model would reach a resting conformation within a timescale possible for simulation. While this allows a full transition to be seen within the simulation it creates the possibility of artefacts caused by a voltage much higher than that found physiologically (*Jensen et al., 2012; Vargas et al., 2012*). While simulations create a range of possible resting states they come to some consensus in the conformational changes that includes the ability S4 sections to shift between 3<sup>10</sup> and α helical secondary structure (*Vargas et al., 2012*).

It should be noted that while structures and models of prokaryotic channels present each VSD in the same conformation this is unlikely for eukaryotic channels as each pseudo-repeat contains a distinct VSD sequence (*Shen. et al., 2017*). This is indeed the case for the cryo-EM structure of a putative cockroach sodium channel Na<sub>v</sub>PaS with each of the VSDs in a distinct conformation. They vary by the extent to which S4 is buried with S4 of DIII and DIV the lowest that of DI half a helical turn higher and DII another half turn higher. They differ in secondary structure with a 3<sup>10</sup> helix in all S4 helices except for DIV, and in the pattern of the salt bridges in part due to sequence differences in the gating charges. The orientation of the VSDs relative to the pore also differs with the inter-domain angles of the VSDs ranging from 83° to 97° (*Shen. et al., 2017*). This supports the idea that voltage sensing domains would activate sequentially in response to membrane depolarisation as suggested by the differing activation kinetics of mammalian Na<sub>v</sub> pseudo repeats.

Hence the whole range of VSD conformations found in Na<sub>v</sub> homologues could prove insightful to the various eukaryotic repeats.

## The selectivity filter of prokaryotic Na<sub>v</sub>s

The selectivity of voltage-gated ion channels is provided by the loop connecting the extracellular helices P1 and P2 located between the pore helices S5 and S6 (Hille, 2001). In structures of open K<sub>v</sub>s and Na<sub>v</sub>s this loop constitutes the narrowest part of the channel below an extracellular funnel acting as an ionic filter (Bagn ris et al., 2013; Jiang et al., 2002; Sula, et al., 2017). In K<sub>v</sub>s the selectivity filter was found to have the consensus sequence T/S-X-G-Y/F-G, and select K<sup>+</sup> by the tight coordination of the dehydrated ion by the main chain carbonyls. While the smaller Na<sup>+</sup> and Ca<sup>2+</sup> ions are excluded by the energetic barrier of dehydration (Doyle et al., 1998). The selectivity of eukaryotic Na<sub>v</sub>s and Ca<sub>v</sub>s has been shown to involve side chain interactions by the ability of Ca<sup>2+</sup> selectivity to be conferred onto rat Na<sub>v</sub> II by lysine to glutamate and alanine to glutamate mutations in domains III and IV, respectively (Heinemann et al., 1992). The side chains important in Ca<sup>+</sup> selectivity are a glutamate at the same position in each domain which together form a ring; the side chains of this ring are known to point into the pore as they are accessible to modification by sulfhydryl compounds which block the pore (Wu et al., 2000). As opposed to Ca<sub>v</sub>s the selectivity filter of eukaryotic Na<sub>v</sub>s are asymmetric with the residues in the equivalent position to the Ca<sub>v</sub> glutamate forming a ring of aspartate, glutamate, lysine and alanine (DEKA) (Armstrong and Hille, 1998), which is surprising given their apparent evolutionary origins as prokaryotic homotetramers. Simulation studies of Na<sup>+</sup> selectivity filters show that coordination from 3 electron donating groups in a narrow aperture favours binding of Na<sup>+</sup> over K<sup>+</sup> (Dudev and Lim, 2009). Within the DEKA selectivity filter it is predicted one oxygen from each of the aspartate and glutamate carboxylates and the alanine carbonyl coordinate to the permeant Na<sup>+</sup> ion while the lysine side chain constricts the pore by hydrogen bonding to the alanine carbonyl and glutamate carboxylate (Dudev and Lim, 2009).

NavRh	PSRWGDLGISLITLTFQVL <b>TLESSWET</b> -VMLPMQEIYWWSWVYFFSFIIICGITILNLVIAI	218
NaChBac	PEYFGNLQLSLLTLFQVV <b>TLESWAS</b> GVMRPIFAEVPWSWLYFVSVFLIGTFIIFNLFIGV	230
NavAb	PEWFGTLGESFYTLFQVM <b>TLESWSM</b> GIVRPLMEVYPYAWVFFIPFIFVVTFFVMINLVVAI	216
NavSheP	PEWFGTIADSFYTLFQIM <b>TLESWSM</b> GISRPVMEVYPYAWVFFVPPFILVATFTMLNLFIAI	227
NavMs	PEWFGDLSKSLYTLFQVM <b>TLESWSM</b> GIVRPVMNVHPNAWVFFIPFIMLTFTVNLNFIGI	217
NavAe	PEWFGTLGASMYTLFQVM <b>TLESWSM</b> GIARPVIEAYPWAWIYFVSVFILVSSFTVLNLFIGI	236
NavPz	PDWFGSLGKSAYSRLFQVM <b>TLESWSM</b> GIVRPVMQEYPLAWLFFVPPFILITTFAVMNLVGL	218
NavSulP	PEWFGSLPASAYSRLFQIM <b>TLESWSM</b> GIVRPVMEVYPYAWVFFVPPFILVTTFAVVNLLVGL	222
	*. :* : * :***:***.** : * : :***. *:: : :**.:::	

**Figure 6. Alignment of prokaryotic  $Na_v$  sequences.** Selectivity filter residues are shown in green. The multiple sequence alignment was performed using Clustal Omega.

The alignment of prokaryotic Na<sub>v</sub>s shown in figure 6 gives the consensus sequence at the region of the selectivity paper to be TLESWSM (residues 175-181 for the Na<sub>v</sub>Ms sequence) which is highly conserved being present in Na<sub>v</sub>Ab, Na<sub>v</sub>Ms, Na<sub>v</sub>Ae, Na<sub>v</sub>Pz, Na<sub>v</sub>SulP and Na<sub>v</sub>SheP amongst others with the exception of NaChBac which has the sequence TLESWAS (*Payandeh et al., 2011; McCusker et al., 2012; Shaya et al., 2013; Irie et al., 2010*). Of this sequence it is the glutamate which lines up with the D/E/K/A of eukaryotic Na<sub>v</sub> domains, meaning they share the selectivity ring of eukaryotic Ca<sub>v</sub>s. Na<sub>v</sub>Rh also differs from the consensus selectivity filter sequence with the sequence TLSSWE (*Zhang et al., 2012*). Na<sub>v</sub>Rh 'channels' did not yield measurable sodium current when expressed in mammalian cells or reconstituted into lipid bilayers, but is proposed to be sodium selective by the observation chimeric NaChBac channels with the Na<sub>v</sub>Rh selectivity filter are sodium selective when expressed in HEK-293 cells.

The first Na<sub>v</sub>Ab structure proposed 3 possible Na<sup>+</sup> binding sites formed by residues of the selectivity filter termed the high field strength site (Site<sub>HFC</sub>), Site<sub>IN</sub> and Site<sub>CEN</sub> shown in figure 7 (*Payandeh et al., 2011*). Site<sub>IN</sub> and Site<sub>CEN</sub> are formed by the backbone carbonyls of the threonine and leucine of the TLESWAS (T175 and L176), respectively, with a spacing of 2.5 Å, this is sufficient to accommodate a Na<sup>+</sup> surrounded by a square array of bound water molecules. Site<sub>HFC</sub> is formed by the carboxylates of the four glutamates of the selectivity filter which form an aperture of appropriate proportions to accommodate a partially dehydrated Na<sup>+</sup> ion, in an asymmetric fashion. This is with one glutamate side chain coordinating directly to the ion and 2 others accepting hydrogen bonds from waters bound to it. The selectivity filter of Na<sub>v</sub>Ab is likely to be very stable in the conformation shown due to a network of hydrogen bonds within the filter, with the P2 helix and to the P helix of the neighbouring subunit (*Payandeh et al., 2011*). Density for sodium ions within a selectivity filter was first observed in Na<sub>v</sub>Ms (*Naylor, et al., 2016*). These structures showed 3 permanent ions, one occupying the predicted Site<sub>HFC</sub> and the other two sitting above the Site<sub>IN</sub> and Site<sub>CEN</sub> positions. The bottom sodium ion is closest to the carbonyl oxygens of leucine 117 and threonine 176 but none of the Na<sup>+</sup> ions are close enough to the peptide side chains or backbone for a direct interaction so this must occur via intermediate water molecules.

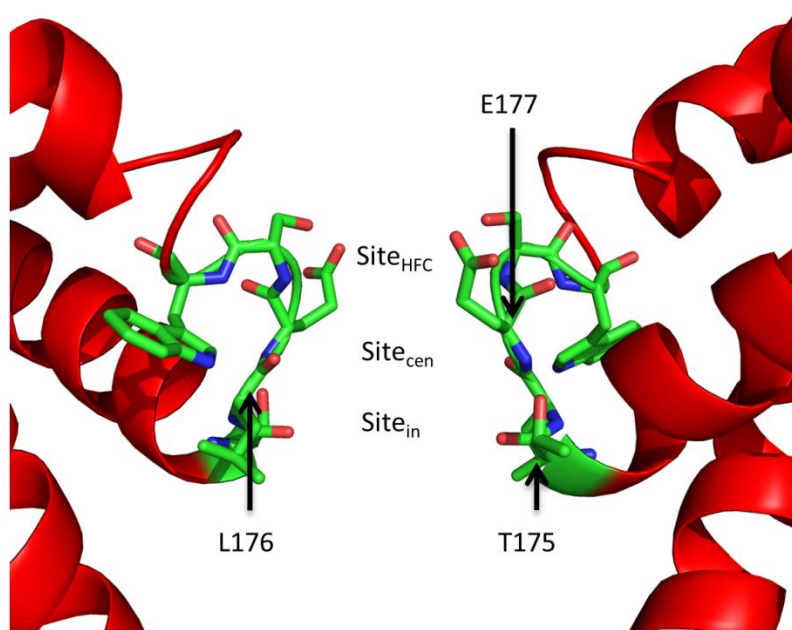


**Figure 7. Structure of the Selectivity filter of Na<sub>v</sub>Ab.** Structure is of PDBID 3RVZ with only opposite subunits visible and the proposed Na<sup>+</sup> binding sites marked. The selectivity filter residues: T175-W179 are shown in green stick representation.

These structures support Hille's model of single ion conduction where the permeating  $\text{Na}^+$  is partially dehydrated by a high field strength anion (E177) and is subsequently re-hydrated, here by the carbonyls of L176. Selectivity of  $\text{Na}^+$  over  $\text{K}^+$  by the high field strength site is thought to be due to the smaller hydrated ionic radius of  $\text{Na}^+$  allowing it to approach the anion more closely and the dehydration to occur more efficiently (Eiseman and Horn, 1983; Hille, 2001; Payandeh et al., 2011). This model is further supported by the conductance of  $\text{Li}^+$  ions by  $\text{Na}_v\text{s}$ , which while not physiological has a smaller ionic radius preventing it from being selected against (Naylor, et al., 2016).

More than 4 Å above the selectivity filter of the  $\text{Na}_v\text{Ab}$  structure are electron densities postulated to be from ion or solvent molecules arranged by the high electronegativity from the selectivity filter; this is proposed to be an outer ion binding site where permeant ions would sit before dehydration or rejection (Payandeh et al., 2011). The structure of  $\text{Na}_v\text{Ae1}$  also shows density above the selectivity filter which is identified as an outer ion binding site (Shaya et al., 2013). While the resolution of this structure is too poor (3.46 Å) to see coordinating geometry or unequivocally assign the density, it is proposed to be  $\text{Ca}^{2+}$ . This is on the basis that low resolution (6.5 Å) electron density maps from three crystals grown in no calcium showed no evidence of density in that position, whereas a second high calcium condition showed an anomalous peak in the same position (Shaya et al., 2013). However no density is seen in the  $\text{Na}_v\text{Ms}$  structures nor suggested by the electrostatic profile of the pore (Naylor, et al., 2016).

$\text{Na}^+$  over  $\text{Ca}^{2+}$  selectivity is proposed to be due to insufficient negative charge at the selectivity filter to dehydrate the divalent  $\text{Ca}^{2+}$  ions. This is supported by mutagenesis in  $\text{NaChBac}$  and  $\text{Na}_v\text{Ab}$  where residues within the selectivity filter above the high field strength site to aspartate increase the selectivity of the channel for  $\text{Ca}^{2+}$  over  $\text{Na}^+$  (Payandeh et al., 2012; Yue et al., 2002). In  $\text{NaChBac}$  mutating the filter to TLESWAD (from TLESWAS) removed  $\text{Na}^+$  selectivity, while TLEDWAS, TLEDWAD and TLDDWAD were  $\text{Ca}^{2+}$  selective with increased current for each aspartate incorporated. Interestingly the introduction of the third aspartate replaces the glutamate found in the selectivity filter of  $\text{Ca}_v\text{s}$  (Yue et al., 2002). Incorporating aspartate residues into the same positions in  $\text{Na}_v\text{Ab}$  also produced a  $\text{Ca}^{2+}$  selective channel, for which a crystal structure was solved (Tang et al., 2013). From this structure three  $\text{Ca}^{2+}$  binding sites are identified and it is proposed  $\text{Ca}^{2+}$  selectivity is achieved by the high affinity for  $\text{Ca}^{2+}$  causing at least one site to be occupied at all times blocking the channel to  $\text{Na}^+$ .  $\text{Na}_v\text{Ms}$  can be made calcium selective by mutating the selectivity filter glutamate to an aspartate (giving TLDSWAD), compared to the wild type this mutant showed no density at the site<sub>HFC</sub> position even when crystallised in the presence of calcium (Naylor, et al., 2016). This structure also showed that shortening of the glutamate to aspartate by a methylene group

moves the carboxylic acid moiety lower in the selectivity filter reducing the charge density at the site<sub>HFC</sub> offering an explanation as to why removing a residue found in calcium channels would increase Ca<sup>2+</sup> selectivity in sodium channels.

Study of the structural basis for selectivity in prokaryotic Na<sub>v</sub>s is complicated by the fact that of the crystal structures to date 3 of them have asymmetrical or collapsed selectivity filters, predicted not to be the conformations able to conduct Na<sup>+</sup>. The Na<sub>v</sub>Ms pore-only structure showed an asymmetric tetramer, the subunits of which were assigned to be in conformations found in different states of channel opening and the heterogeneity was an artefact of crystallisation (McCusker *et al.*, 2012). From this a model of the structure of the open channel was made using the conformation of the subunit that produced the widest aperture overlaid on to the positions of each of the other subunits. This model was shown to be accurate by a subsequent crystal structure of Na<sub>v</sub>Ms including the C-terminal domain which showed the pore as a symmetric tetramer with similar features (McCusker *et al.*, 2012; Bagn  ris *et al.*, 2013).

The collapsed filters seen in the crystal structures of both the wild type Na<sub>v</sub>Ab and Na<sub>v</sub>Rh are proposed to be physiological, representing channel inactivation. The wild type Na<sub>v</sub>Ab structure contains channels in 2 different conformations both of which are closed at the selectivity filter due to one pair of opposite subunits moving away from each other and the other pair moving together (Payandeh *et al.*, 2012). These are shown in figure 8 with black arrows indicating the difference to the original Na<sub>v</sub>Ab I221C structure. Both these conformations are proposed as different inactivated states, based on the fact that different lengths of depolarisation lead to different kinetics of activation in eukaryotic Na<sub>v</sub>s, indicating a range of inactivated states (Toib *et al.*, 1998). The Na<sub>v</sub>Rh selectivity filter (figure 8 top right) forms the narrowest part of the pore due to the serine 181 side chains pointing inwards and is proposed to be an inactive conformation; however it must be noted current could not be measured from Na<sub>v</sub>Rh channels (Zhang *et al.*, 2012). The role of the selectivity filter is supported by mutagenesis in eukaryotic Na<sub>v</sub>s that affect the process of slow inactivation (Xiong *et al.*, 2006) and the fact that the binding of ions to the selectivity filter impedes slow inactivation, which also suggests a movement of the selectivity filter is involved (Townsend *et al.*, 1997). While the role of selectivity filter in inactivation of prokaryotic Na<sub>v</sub>s is supported by mutagenesis of NaChBac (Pavlov *et al.*, 2005), these studies were designed to show residues in the pore rather than C-terminal domain caused inactivation. These studies were performed before a plug like mechanism as seen in eukaryotic Na<sub>v</sub>s had been eliminated as a model. Because in closed structures there is clearly a closure of the channel at the end of S6 it was hypothesised that this gate is involved in activation and the selectivity filter in inactivation (Payandeh *et al.*, 2012).

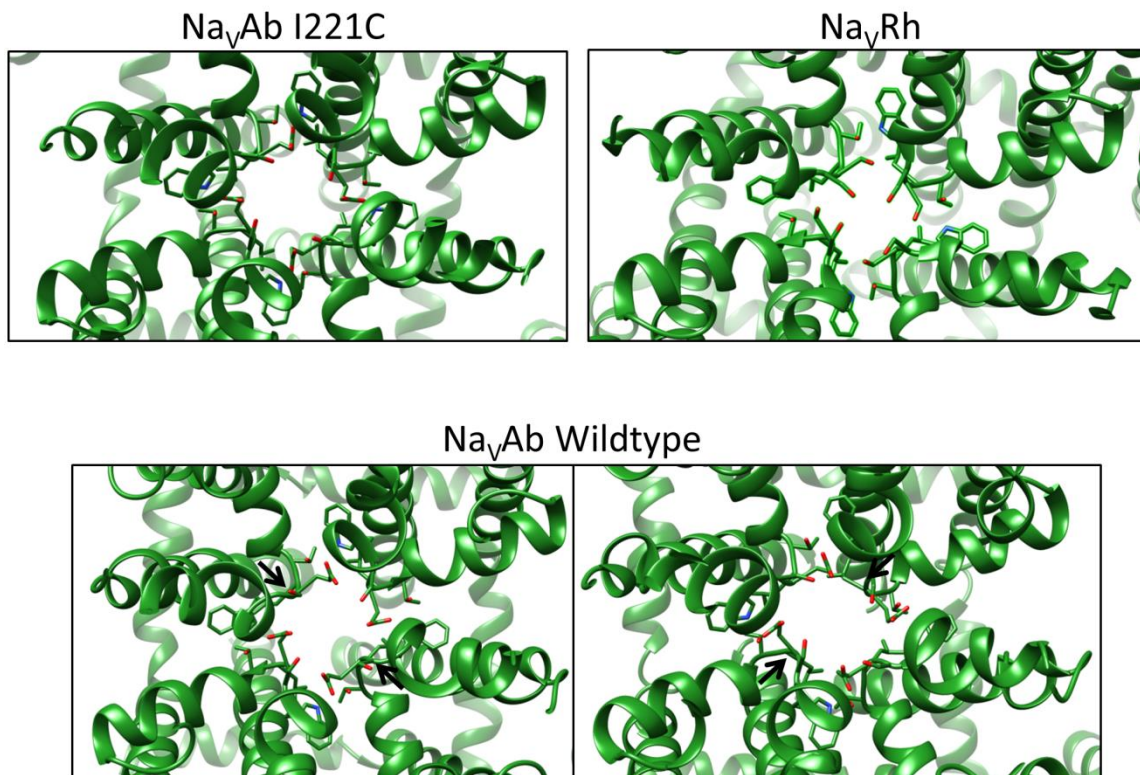


**Figure 8.** The selectivity filters of the NaVAb wildtype and I221C mutant, and NaVRh. The protein is shown in cartoon with line representation for the selectivity filter residues TLESW. For the NaVAb wildtype structures black arrows show the constriction of the pore relative to the I221C mutant. Structures are based on PDBIDs 4ekw 3rvy and 4dxw.

## The Na<sub>v</sub> ion conducting pore and gating

The S5-S6 regions of Na<sub>v</sub>s form the ion conducting pore, this region alone is able to self-assemble into a functional ion channel both as a tetramer for prokaryotic Na<sub>v</sub>s (*McCusker et al., 2011*) and as a monomer of pseudo-repeats where the VSDs are replaced with poly glycine linkers in a eukaryotic construct (*Chen et al., 2002*). As with K<sub>v</sub>s (*Chen et al., 2010*) these helices form an ‘inverted tepee’ shape narrowing at the intracellular side either fully for closed channels (*Payandeh et al., 2011*) or partially for open channels (*Bagn ris et al., 2013*). The interior of the pore forms a strongly electronegative environment allowing for rapid conductance of Na<sup>+</sup> ions as shown in figure 9 which is a cross section through the channel coloured with surface charge (*Bagn ris et al., 2013*; *Ulmschneider et al., 2013*).

At the edge of the pore is a cavity accessible to the lipid environment of the bilayer running all the way to the centre of the pore known as a fenestration. The edges of the fenestration are formed by the sides of S5 and S6 as shown in figure 10 for Na<sub>v</sub>Ab and Na<sub>v</sub>Ms (*Payandeh et al., 2011*; *Bagn ris et al., 2013*). In the Na<sub>v</sub>Ab structure this aperture measures ~8   by 10   and was found to be occupied by a density which was modelled as an acyl chain protruding into the pore blocking it. As none of the detergents in the crystallisation conditions contained acyl chains and both K<sub>v</sub>s and Ca<sub>v</sub>s are modulated by phospholipids (*Oliver et al., 2004*; *Delmas et al., 2005*), the density was proposed to be due to a physiological phospholipid from the growth conditions involved in inactivation of the channel. This led to the proposition that the opening of the channel would involve closure of the fenestrations and withdrawal of the acyl chains. While this is supported by lack of fenestration in the open K<sub>v</sub>1.2 structure (*Chen et al., 2010*), structures of Na<sub>v</sub>Ms in the open conformation contain fenestrations larger than those in Na<sub>v</sub>Ab yet lacking acyl density (*McCusker et al., 2012*; *Bagn ris et al., 2013*). The fenestrations do however provide a basis for the action of small hydrophobic drugs on Na<sub>v</sub>s as they open towards the region of the pore where residues identified as important in the drug binding of eukaryotic Na<sub>v</sub>s and Ca<sub>v</sub>s (*Payandeh et al., 2011*; *Hockerman et al., 1997*; *Ragsdale et al., 1994*). The proposed closure of the fenestrations during pore opening provided an explanation for the stronger binding of local anaesthetics to inactivated Na<sub>v</sub>s. Given the change in shape of the fenestration in the open Na<sub>v</sub>Ms structure it is feasible the fenestration itself contributes to drug binding and a conformational change in it rather than a closure is the cause of state dependant binding (*McCusker et al., 2012*).

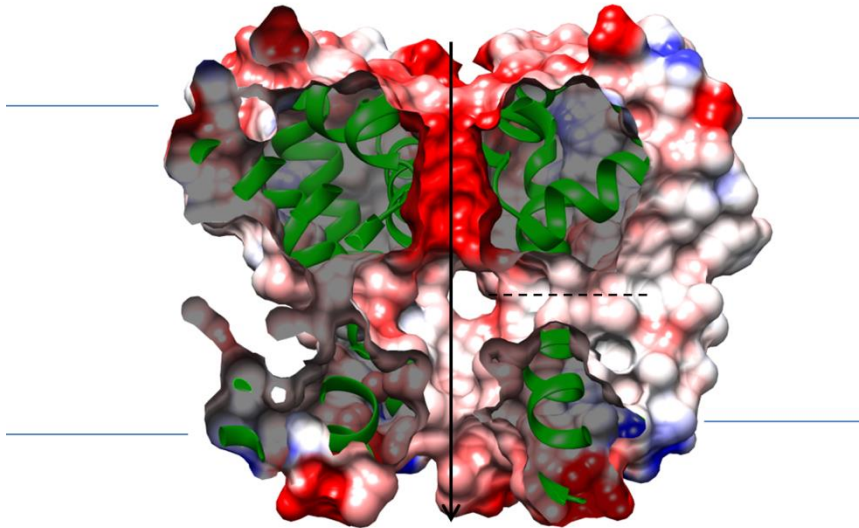


**Figure 9. A cross section through the Na<sub>v</sub>Ms pore.** *The surface charge is coloured from -5 (red) to +5 (blue) using the electrostatic potential function of chimera, which is based on APBS (Baker et al., 2001). The edges of the membrane are shown as blue lines the path of a sodium ion to the cell as a black arrow and the bilayer accessible cavity a dotted line.*

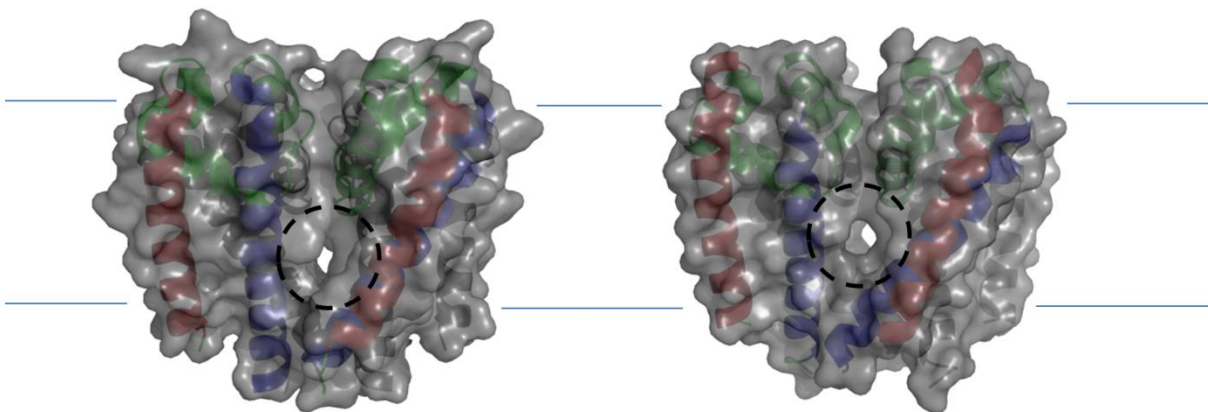


**Figure 10. Comparison of the fenestrations of Na<sub>v</sub>Ab and Na<sub>v</sub>Ms.** *Na<sub>v</sub>Ab structure (left) is PDBID 3rvy and Na<sub>v</sub>Ms (right) is 3zjz. A side view of the pore in each channel is shown with the fenestration visible as a gap in the translucent grey surface, highlighted by a dashed circle. The S5 and S6 helices of the front 2 subunits are red and blue respectively with the rest of these subunits in green and those at the back grey. The edges of the membrane are shown as blue lines with the extra cellular side top*

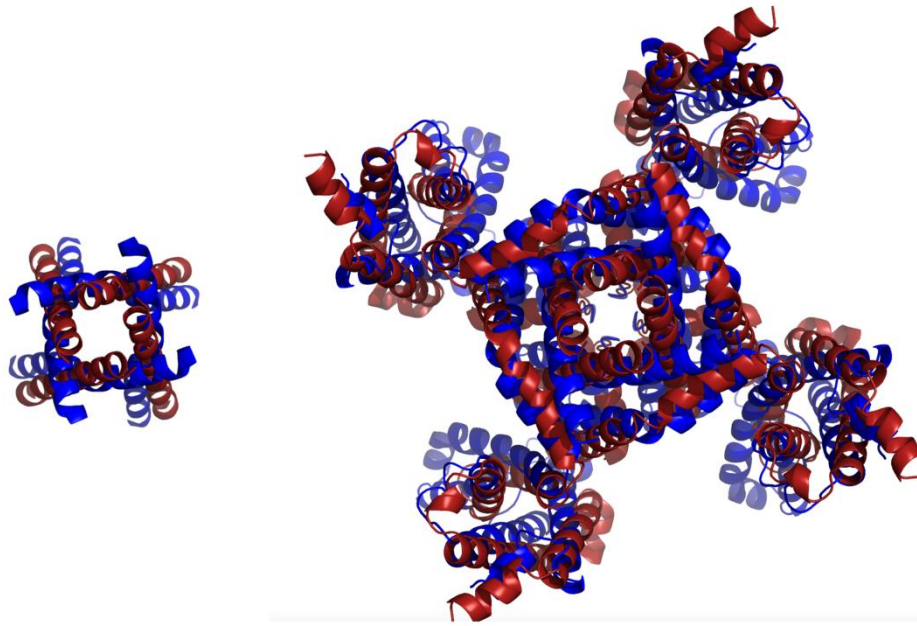


**Figure 11. Superposition of Na<sub>v</sub>Ab and KV1.2.** Na<sub>v</sub>Ab (PDBID 3rvy) is shown in blue overlaid with the KV1.2 (PDBID 2a79) in red looking down the pore axis. Channels were aligned as described in Payandeh et al., 2011 by aligning the sequence after the P-loop. The pore lining helix alone is shown left with the whole channel shown right.

The overlay of the Na<sub>v</sub>Ab and K<sub>v</sub>1.2 structures at the VSDs in figure 11 shows them diverge at the start of S5 (*Payandeh et al., 2011*), this with the assignment of the structure as ‘pre-open’ lead to a model of pore opening. In this model the activated VSD pulls S4 into the membrane, pushing the S4-S5 linker towards the pore causing a hinge at the beginning of S5 to turn shifting S5-S6 as a unit around the pore axis creating an ‘iris-like’ dilation (*Payandeh et al., 2011*). In this model the Na<sub>v</sub>Ab structure captured would represent the point after the VSDs have activated and the S4-S5 linkers translated but before the action of the S5 hinge. The capture of this transient state is believed to be due to stabilisation by a Ile to cysteine mutation in S6 induced to aid crystallisation. The mutational stabilisation of a pre-open state is supported by a more negative activation potential of the cysteine mutant compared to the wild type channel during patch clamp readings (*Payandeh et al., 2012*).

Before crystal structures of Na<sub>v</sub>s had been determined gating was thought to be achieved by a glycine hinge in S6 allowing bending within the helix opening and closing the cytoplasmic end of the pore (*Zhao et al., 2004a*). This region was identified by the difference in the structures of the pore only potassium channel MthK and KcsA, which are open and closed respectively deviating at a glycine in S6 by a kink of ~30° (*Jiang et al., 2002; Doyle et al., 1998; Zhao et al., 2004b*). A glycine in the region has been found to be highly conserved from K<sup>+</sup> channels to Na<sup>+</sup> and Ca<sup>2+</sup> channels and its’ relevance to bacterial Na<sub>v</sub>s supported by mutagenesis in NaChBac (*Zhao et al., 2004a*). When the analogous S6 glycine (G219) of NaChBac is mutated to proline a kink of 21-26° would be induced, resembling that found in the MthK structure. The activation potential of the kink mutant shifted -50mV, activation was sped up by a factor of 1200 and deactivation slowed by a factor of 2000 relative to the wild type channel (*Zhao et al., 2004a*). This is indicative of stabilisation of the open conformation of the channel supporting the proposed hinge function of G219. The characterisation of the hinge glycine residue was followed by proline scanning mutagenesis of S6; of the seven mutants that produced measurable channels, four only had modest effects on the voltage dependence and kinetics compared to the wild type (*Zhao et al., 2004a; 2004b*). The remaining three mutants are I222P, L226P and G229P and all are predicted to be on the same face of S6 as G219 and hence would induce a kink in the same direction. All three of these mutants had the surprising effect of switching the channels voltage dependence so they activate on hyperpolarisation of the membrane rather than de-polarisation. (*Zhao et al., 2004b*).

It is then surprising that while reasonably conserved through voltage-gated cation channels the ‘hinge’ glycine residue is absent from many of the prokaryotic Na<sub>v</sub>s including Na<sub>v</sub>Ab, Na<sub>v</sub>Ms, Na<sub>v</sub>BaCL, Na<sub>v</sub>RosD and Na<sub>v</sub>SheP all of which are able conduct sodium in a voltage dependant manner

typical of the family (Payandeh *et al.*, 2011; Bagn ris *et al.*, 2013; Irie *et al.*, 2010). NaChBac has a second glycine residue within S6 in the position of the 'PXP' motif of K<sub>v</sub>s which induces a kink in K<sub>v</sub>1.2 and has been suggested as critical for K<sub>v</sub> gating (Chen *et al.*, 2010). This second glycine is shared by other prokaryotic Na<sub>v</sub>s yet mutation of it in NaChBac, Na<sub>v</sub>BacL and Na<sub>v</sub>RosD has no effect on activation, only speeding inactivation (Irie *et al.*, 2010). There are also still fully functional prokaryotic Na<sub>v</sub>s like Na<sub>v</sub>Ab and Na<sub>v</sub>SheP with no glycine residues within S6.

It then seems inconsistent that mutations within S6 should affect inactivation when the collapse of the selectivity filter has been attributed to inactivation, while S6 is implicated in channel opening (Payandeh *et al.*, 2012; Zhang *et al.*, 2012). One possible explanation for this is the stabilisation of the selectivity filter, by interactions with S6 at the position of the hinge glycine as is seen in KcsA (Blunck *et al.*, 2006). Hence mutation of residues in this region could de-stabilise the open conformation of the selectivity filter allowing it to collapse more easily speeding inactivation. While the pre-open structure of Na<sub>v</sub>Ab shows a network of hydrogen bonds stabilising the selectivity filter they are not particularly associated with this region of S6 (Payandeh *et al.*, 2011). It could then be that any mutations causing significant movement of residues at the top of the pore disrupt the ability of this network to form as whole.

Superposition of the open Na<sub>v</sub>Ms onto the 'pre-open' Na<sub>v</sub>Ab structure show a good alignment of the positions of C<sub>α</sub> atoms up until threonine 209 where the structures deviate by a rotation of ~25° around the ψ bond of this residue (McCusker *et al.*, 2012). The rotation is small enough to maintain the α-helix in this region yet results in a ~2.5 Å displacement of the intracellular end of S6. This displacement creates an aperture of diameter 8 Å which is sufficient for a hydrated sodium ion to pass and consistent with Na<sup>+</sup> traversing the pore hydrated after leaving the selectivity filter. In the crystal structure of the full length Na<sub>v</sub>Ms further along the S6 is visible continuing past the pore to interact with the S4-S5 linker and S3 of the VSD while maintaining the same pore architectures as the Na<sub>v</sub>Ms pore structures (Sula, *et al.*, 2017). These interactions are mediated by a network of salt bridges and hydrogen bonds between the charged residues at the end of S6 and the S4-S5 linker and also by an aliphatic stacking interaction with tryptophan 77 in S3. This tryptophan residue is highly conserved in prokaryotic and eukaryotic sodium channels but absent from other ion channels. This network of interactions suggests conformational changes can be transmitted from the VSDs not only via the S4-S5 linker backbone to S5, but also by direct interaction of the VSDs with the end of S6.

## The C-terminal coiled coil of prokaryotic Na<sub>v</sub>s

The C-terminal domain of prokaryotic Na<sub>v</sub>s consist of a heptad repeat characteristic of a coiled-coil structure connected to S6 by a linker predicted to be disordered (Powl *et al.*, 2010). Synchrotron radiation circular dichroism (SRCD) spectroscopy of truncated NaChBac constructs predict the last 22 residues to be helical in nature and connected to S6 by a 14 residue linker that forms a disordered random coil (Powl *et al.*, 2010). From this it was proposed the C terminus forms a bundle of 4 helices of structure similar to that seen in the KcsA C terminal domain despite only having a modest sequence identity of around 10% (Uysal *et al.*, 2009).

The structure and dynamics of a prokaryotic Na<sub>v</sub> pore and CTD were studied by electron paramagnetic resonance, using mutants incorporating cysteine in the CTD derivatised with nitroxide spin labels (Bagnéris *et al.*, 2013, Arrigoni, *et al.*, 2016). Continuous wave (cw-EPR) measurements are able to show the mobility of the labelled residue, and hence indicate the flexibility in that region of the protein. The residue at the end of S6 showed little mobility as would be expected in a rigid transmembrane helix, while the label in the middle of the predicted linker region showed a high mobility, and labels within the predicted 4 helix bundle had restricted mobility but were still more mobile than those in S6. These observations are consistent with an ordered coiled coil which is mobile by virtue of connection to the pore by a flexible linker. Interestingly the residues at either end of the linker each seemed to experience 2 different states suggesting the ends of the helices may incorporate these residues some of the time (Bagnéris *et al.*, 2013). Pulsed double electron-electron resonance (DEER) spectra are able to give distributions of the distances between spin labels. The DEER spectra for the labels within the coiled coil segment are consistent with the spin label on each of the subunits forming a square as would be expected in a symmetric 4 helix bundle whereas the spectra for the labels within the linker region are reminiscent of a highly flexible but not disordered structure (Bagnéris *et al.*, 2013). The EPR measurements were used to build a model of the 4 helix bundle based on the KcsA CTD structure connected via a flexible linker to the pore which had been solved by x-ray crystallography. The dimensions of this model were consistent with the CTD coiled coil occupying the regions between the pores in the crystal structure, rendered invisible in the structure due to the flexibility of the linker preventing them from ordering in the lattice (Bagnéris *et al.*, 2013).

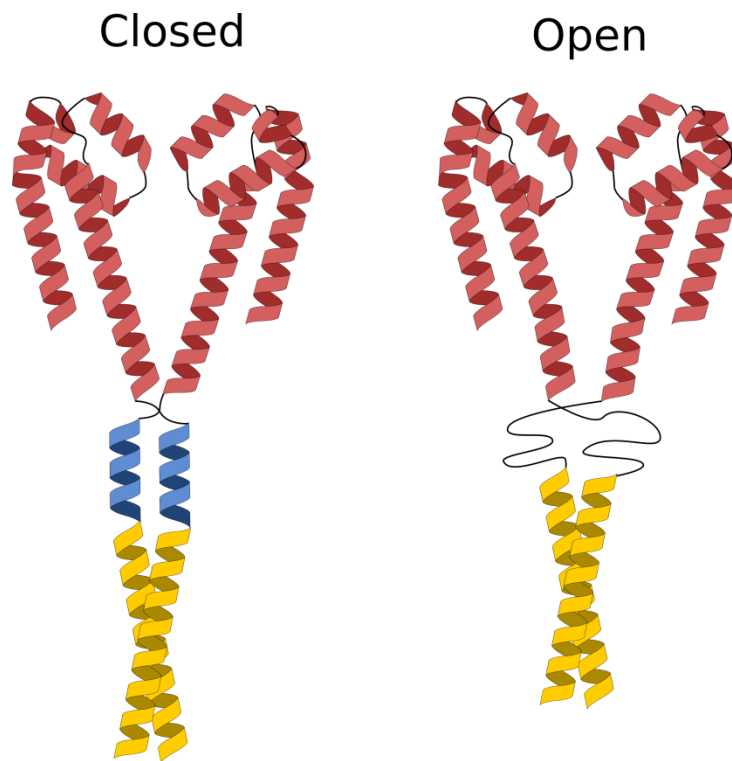


**Figure 12. Diagram of the proposed role of the linker and C-terminal coiled coil in gating.** The pore helices are shown in red, the coiled coil in yellow and linker in blue when in a helical conformation, this diagram is based on PDBID 3zjz

The function of the C-terminus of prokaryotic Na<sub>v</sub>s is still little understood. In NaChBac and Na<sub>v</sub>Ms the pore can assemble without the C-terminus (Milo *et al.*, 2010; McCusker *et al.*, 2012) but as would be expected from a domain with an extensive surface of inter-domain interactions it stabilises the tetramer in NaChBac (Powl *et al.*, 2010; Milo *et al.*, 2010). Deletion of the NaChBac C-terminus does not seem to significantly reduce the protein levels of the whole cell lysate when expressed in *E.coli* but does reduce the amount of protein in the membrane fraction indicating the C-terminus may be involved in correct folding and membrane insertion (Powl *et al.*, 2010). Direct structure determination of a prokaryotic Na<sub>v</sub> C-terminus was first seen in Na<sub>v</sub>Ae1 which seems to have a much more rigid linker region, constricting the movement of the C-terminus allowing it to become visible in the crystal structure and showing the linker to form an  $\alpha$ -helix (Shaya *et al.*, 2013). The coiled coil is also seen in the full length Na<sub>v</sub>Ms structure where the end of S6 may be stabilised by its interaction with the VSD in turn constraining the CTD. Interestingly the expression of Na<sub>v</sub>Ae1 in mammalian cells did not yield functional channels yet mutation of 3 residues within the linker to glycine produced functional voltage-gated channels suggesting channel opening is linked to a loss of helical nature in the linker. This with the observation that the more glycine residues mutated into the linker region of Na<sub>v</sub>Sp the more negative the voltage dependence of activation became, indicates that reducing the ability of the neck region to form a helix destabilises the closed conformation of the pore. These observations with the cw-EPR spectra suggesting linker residues can switch between helical and loop conformations (Bagn ris, *et al.*, 2013; Nurva, *et al.*, 2016), leads to a possible role of the CTD where a loop to helix transition of the linker regions occurs during channel closure and the 4 helix coiled coil tethers the linkers together (Shaya, *et al.*, 2013). The variation in different species linker sequences would then lead to variation in the voltage dependence of activation by the ability of the sequence to become helical.

## Na<sub>v</sub> ligand binding

The homology between eukaryotic and prokaryotic sodium channels within the pore domain makes bacterial Na<sub>v</sub>s a good model for investigating the binding of small molecules to the local anaesthetic site in this region. Na<sub>v</sub>Ms was found to be inhibited by the eukaryotic channel blockers lidocaine and lamotrigine (Bagn ris, *et al.*, 2014), however the identification of a bound structure was hindered by the four-fold symmetry of the channel giving four identical binding sites which if mutually exclusive would give a maximum occupancy of 25% in a crystal structure. To overcome this Na<sub>v</sub>Ms was crystallised with a brominated lidocaine analogue which still binds with a 25% occupancy but the anomalous scattering of the bromine atom allowed its position to be determined. Figure 13

shows the bromine atom to be near the fenestration of Na<sub>v</sub>Ms, which is proposed for drug entry in the Na<sub>v</sub>Ab structure (Payandeh, et al., 2011; Bagn ris, et al., 2014). Docking of the rest of ligand revealed a consensus binding mode with the rest of the molecule leading up into the vestibule of the pore and making contact with a T207 and F214, the equivalent residues to these in DI-IV of eukaryotic channels have an important role in local anaesthetic binding and state dependant block (Desaphy, et al., 2010; Hanck, et al., 2009; Bagn ris, et al., 2014).

While the homology between prokaryotic and eukaryotic sodium channels in this region provides a useful tool it also highlights a problem in pharmacology, there is little variation in this region between mammalian Na<sub>v</sub> subtypes leading to low subtype specificity for compounds targeting it (Ragsdale, et al., 1996; Bagal, et al., 2015). In contrast Na<sub>v</sub> targeting toxins show a much greater degree of subtype selectivity with the human Na<sub>v</sub>s initially classified by their sensitivity to the small molecule tetrodotoxin from puffer fish which binds to the extracellular pore (Lipkind and Fozzard, 1994). A variety of cysteine rich peptide based toxins from spider, snail, centipede and scorpion venoms bind to the extra cellular loops of eukaryotic Na<sub>v</sub>s where subtype homology is lowest and prokaryotic channels resemble the eukaryotic the least (Xiao, et al., 2010; Bagal, et al., 2015).

Prokaryotic Na<sub>v</sub>s are known to be inhibited by general anaesthetics (Ouyang et al., 2007). The possible role of Na<sub>v</sub> inhibition in general anaesthesia of eukaryotes is unclear as several other classes of ion channels are inhibited by general anaesthetics, including K<sub>v</sub>s (Annika et al., 2011) and ligand gated ion channels (Cacheaux et al., 2005). In recent years the inhibition of Na<sub>v</sub> channels has been highlighted as a major contribution to the changes in neurotransmitter release seen in general anaesthesia (Herold and Hemmings, 2012). This is supported by NMR studies and molecular dynamics simulations that highlight several putative binding sites for the general anaesthetics isoflurane and sevoflurane binding to NaChBac (Barber et al., 2014; Kinde et al., 2016; Raju et al., 2013). While binding is predicted around the local anaesthetic site, there are also putative binding site across the protein including the S4-S5 linker, and extra cellular P-loops. The only commonality between these sites is their amphipathic nature. Given the range of different proteins affected by general anaesthetics and the range of binding sites it is unclear how specific these interactions are.

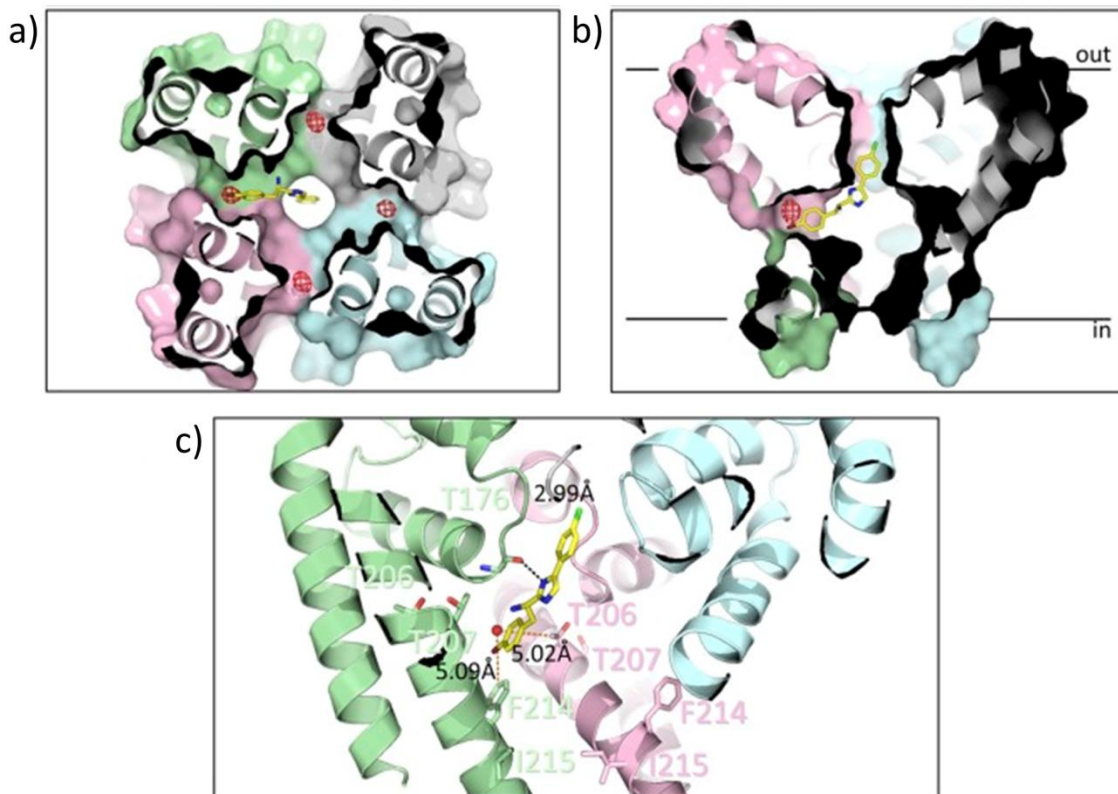


**Figure 13. The anomalous scattering of a brominated  $\text{Na}_v\text{Ms}$  ligand and subsequent docking result.** The docked PI1 molecule is shown as a yellow line model with the anomalous bromine peak red mesh spheres in a) and b). The distances to interacting side chains are shown in c) figure reproduced and adapted from Bagneris et al. 2014

In recent years there have been numerous patents have been submitted by Pfizer and AstraZenica for small molecule compounds showing significant subtype selectivity (*Bagal, et al., 2015*). Of particular interest are the aryl sulphonamides one of which has been crystallised bound to a chimeric fusion of the Na<sub>v</sub>1.7 VSD<sub>IV</sub> to the Na<sub>v</sub>Ab pore. This shows the ligand binding into the extracellular pocket of the voltage sensor between S2 and S4 (above the hydrophobic constriction site) with the molecule extending down S4 to make an ionic interaction with the R4 gating charge (*Ahuja, et al., 2015*). Electrophysiology has shown the aryl sulphonamide to trap the voltage sensor in an activated state, as it binds in a region with high variation between subtypes which undergoes a significant structural rearrangement on gating. This work shows how the binding of ligands to novel sites can give both subtype and state dependant binding.

## Outlook

While recent structural studies on voltage-gated sodium channels have greatly increased our understanding of their function and pharmacology there are still many questions to be answered before the process of voltage-gated ion conduction can be understood to an atomic level. The main hindrance is in the lack of structures of the same channel in different functional states, this makes any inference on why a channel is in a given conformation difficult as it could be due to sequence or crystallisation conditions. Crystal structures also are only able to give static views of conformations able to be crystallised requiring detergents which remove physiological lipids or lipidic cubic phase, which are unseen in nature. As seen by the recent 3.8 Å structure of a cockroach Na<sub>v</sub> and 4 Å structure of the related channel TRPV2 (*Zubcevic et al., 2016*) cryo-EM is fast developing as an excellent structural tool for studying sodium channels. However like X-ray diffraction cryo-EM is only able to give snap shots of individual states. While cryo-EM is able to differentiate multiple states as separate classes this could be difficult as gating is proposed occur by small movements of helices inside the channel. This is further complicated by the crystal structure of Na<sub>v</sub>Ab which show out of the membrane environment voltage sensors can appear to be in the opposite state to the pore. Hence the development of high resolution biophysical measurements to assess the properties of sodium channels in a range of conditions unamenable to crystallography will greatly increase our understanding of Na<sub>v</sub> function and gating. Independent assays of gating will be highly complementary to other structural techniques such as cryo-EM to define the predominant states within given experimental conditions or protein constructs. This study aims to investigate biophysical tools which could be used to achieve this. The use of oriented circular dichroism to assay the state of Na<sub>v</sub>s by the conformations of pore α-helices is investigated. While the applicability of single molecule Förster resonance energy transfer to measuring movements of the gate is also

tested. Due to its' ability to be expressed in *E.coli* and the wealth of structural data available for it the prokaryotic channel  $\text{Na}_v\text{Ms}$  is chosen as a case study.

# AnglerFish: a tool for defining the orientation of $\alpha$ -helical pores

---

## Introduction

Integral membrane proteins make up 30% of the human genome (*Arinaminpathy et al., 2009*); many of these are comprised of transmembrane helical segments whose alignment with respect to each other controls the translocation of ions or molecules across the membrane. Despite the functional importance of transitions between open and closed states of channels, or outward and inward facing states of transporters, there is no universal system or tool for defining the angles associated with helix movement. Such changes tend to be quantified indirectly by differences in pore diameter (*Smart et al., 1996*) or as changes in the  $\phi$  and  $\psi$  angles of individual residues (*McCusker et al., 2012*). While those approaches can inform on some features associated with gating by comparisons of 'open' and 'closed' structures, they do not reflect quantitative changes associated with the orientation of an  $\alpha$ -helix. Presented here is AnglerFish, an easy-to-use webserver for defining the angles of transmembrane helices published in bioinformatics (*Colledge and Wallace, 2016*). Anglerfish is designed to quantify differences of conformation for related proteins in different functional states. This acts as a complementary method to analysing torsion angles and pore diameter. The use of Anglerfish is then shown in defining the kinking of a helix on the gating of the NaK channel, quantifying the contributions of GLIC transmembrane helices to gating and analysing the asymmetry of a Na<sub>v</sub>Ms pore structure. These are sample examples of the application of Anglerfish to ion channels; the method is also applicable to any protein with 3-fold or above symmetry that undergoes a conformational change involving an  $\alpha$ -helix.

## Methods

### Definitions

AnglerFish models a helical bundle as a rotationally symmetric arrangement of helices around a central pore of any size, shown as the dotted line in figure 1a. The orientations of the helices are defined by two angles, tilt and swing, which describe the helical axis relative to the pore axis (or the axis of rotational symmetry for the helices). The pore axis is defined as the normal to a plane containing the C $\alpha$  atom of the same residue number from each helix, this can be seen as the blue triangle in figure 1a which intersects the example residue A in each helix. Hence the separate chains must be aligned with equivalent residue numbering. The N and C-terminal ends of the helices

(denoted N and C) are defined as averages of the first and last 4 C $\alpha$  co-ordinates respectively, while the helical axis is defined as the line connecting them.

Tilt is defined as the angle between the pore axis and the helix axis at N ( $\theta_t$ , Figure 1c). Changes in  $\theta_t$  can dilate a pore in the manner of limbs of an umbrella as it opens (Figure 1b). Swing ( $\theta_s$ , Figure 1d) is the angle perpendicular to the pore axis between the line connecting N and the pore axis (blue line) and, the line connecting the component of the helix axis perpendicular to the pore axis (orange line). In other words swing is the angle the helix axis must be rotated around the pore axis in order the helix axis would intersect with the pore axis. This is defined such that a swing value of 0° indicates the C-terminal and of the helix is closest to the pore axis and 180° that the N-terminal end is closest to the pore axis. Changes in  $\theta_s$  can dilate a pore in a similar fashion to double doors opening in opposite directions (Figure 1b). As the pore axis is only dependent upon the protein coordinates,  $\theta_t$  and  $\theta_s$  are independent of the orientation of the protein within the membrane, i.e. the planes representing the lipid bilayer are not taken into account for the calculation of  $\theta_s$  and  $\theta_t$ . Hence the method may be applied to structures solved by nuclear magnetic resonance (NMR), crystallography or electron microscopy independent of the need for data indicating the bilayer position. This also means that while designed for use with membrane pores this method is not limited to them. It is possible for AnglerFish to characterise any rotationally symmetric arrangement of alpha helices, such as those found at the vertices of virus particles.

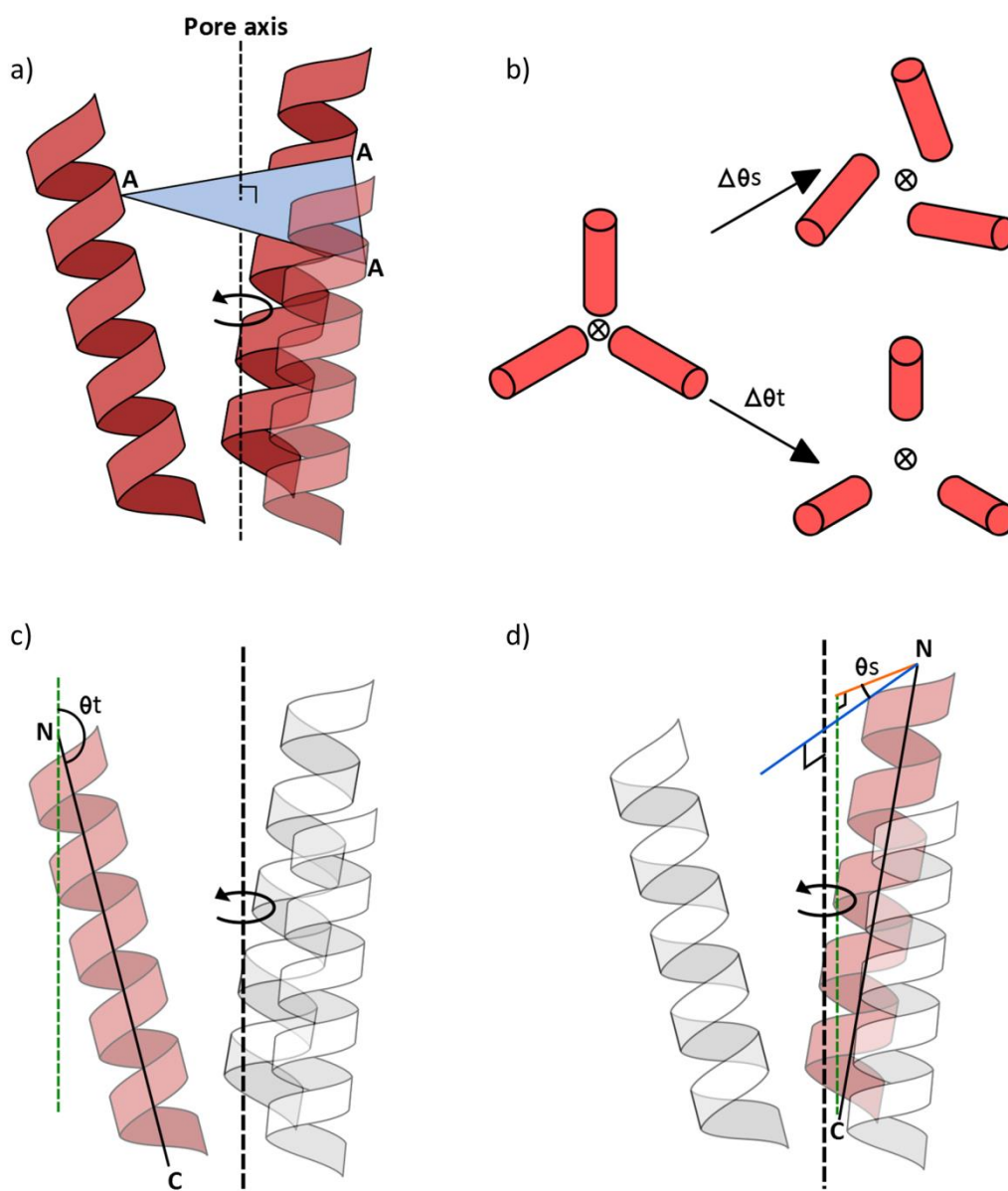


**Figure 1. The definitions of tilt and swing used in AnglerFish.** a) The pore axis (black dashed line) is shown as perpendicular to a blue plane containing the same residue number (labelled A) from each chain. b) changes in tilt ( $\theta_t$ ) and swing ( $\theta_s$ ) are shown to dilate a pore from above with the pore axis shown as a circled cross. c)  $\theta_t$  is shown as the angle between the helical axis (black line between N and C and, a parallel to the pore axis (green dashed line). d)  $\theta_s$  is shown as the angle between the shortest line between the N end of the helix and pore axis (blue line) and, the component of the helical axis that is perpendicular to the pore axis (orange line).

## Calculations

AnglerFish is available at <http://anglerfish.cryst.bbk.ac.uk>, and the source code is available via GitHub (ID number: 23099800).

As stated the pore axis is defined as the normal to a plane containing the residue of the same number ( $A_{xi}$ ) from each chain. The coordinates of each residue are read in as the positions of the  $C\alpha$  atoms. Figure 2 shows how the axis is defined, the plane containing the  $A_{xi}$  residue is defined by vectors from  $A_{xi}$  of one chain (A) to two others (B and C). The normal to this plane is calculated as the cross product of these two vectors ( $\underline{AB} \times \underline{AC}$ ). As this only considers three chains this is repeated for every combination of three chains in the structure. However the cross product  $\underline{AB} \times \underline{AC}$  will be equal and opposite to  $\underline{AC} \times \underline{AB}$  so if the normal to all combinations were averaged they would cancel out. To overcome this, the result of  $\underline{AB} \times \underline{AC}$  is stored to define 'up' for the protein and any set of chains which produce a normal greater than  $90^\circ$  from this is discarded (the red vector in figure 2). For this purpose A, B and C are the first 3 chains being considered and are independent of chain naming. The remaining normals are averaged to give the pore axis vector  $\underline{Ax}$ .

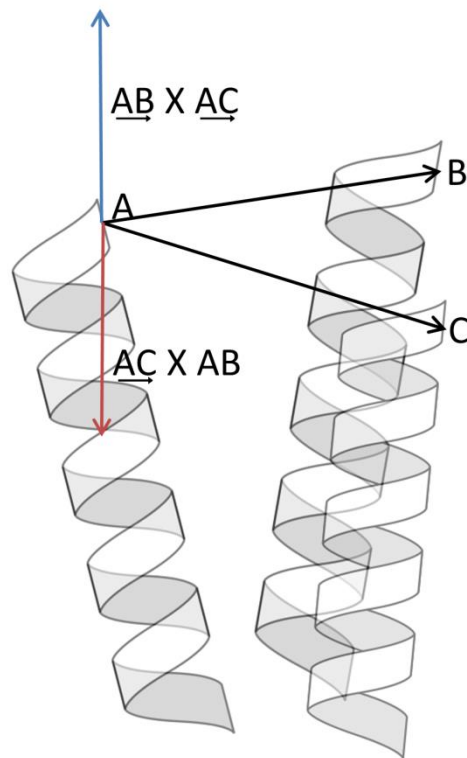


**Figure 2. The calculation of the pore axis by cross product.** Vectors from the Ca coordinate of a residue in A to the equivalent residues in chains B and C are shown as black arrows. The cross products of these vectors are shown in blue and red, with the red opposite to the blue so discarded for axis calculation.

Anglerfish may be run in this fashion with the user defining which residue to define the pore axis however in most cases it will not be obvious which residue is best suited to this. To automatically select a residue to calculate the pore axis, each residue is considered. The range of x, y and z values for the axis unit vectors obtained from each subset of chains. The residue which has the lowest total range (sum of the ranges of x, y and z) is selected. This means the residue is picked with the most similar normals from the subsets of chains, and that the residue is picked where its' copies in each chain conform closest to a uniform plane.

The helical axis is defined as the vector  $\underline{NC}$  where N and C are the averages of the  $C\alpha$  coordinates of the first and last 4 residues in the helix. The tilt angle  $\theta_t$  is calculated using the dot product relationship:

$$\underline{NC} \cdot \underline{Ax} = |\underline{NC}| \cdot |\underline{Ax}| \cos\theta$$

$$\text{Or: } \theta = \cos^{-1} \left( \frac{\underline{NC} \cdot \underline{Ax}}{|\underline{NC}| \cdot |\underline{Ax}|} \right)$$

Where  $\underline{NC} \cdot \underline{Ax}$  is the dot product between vectors  $\underline{NC}$  and  $\underline{Ax}$  and,  $|\underline{NC}|$  and  $|\underline{Ax}|$  are the magnitudes of these vectors. This is done separately for the defined helix in each chain which is reported along with an average.

The calculation of the swing angle  $\theta_s$  requires the centre of the pore (Cen) be defined, this is done as an average of the  $Ax_i$  coordinates in each chain.  $\theta_s$  itself is the angle between vectors from N to the pore Axis ( $\underline{NAx}$ ) and the component of the helical axis perpendicular to the pore axis ( $\underline{NC}_\perp$ ), figure 3 shows how these are found. The point on the axis that is closest to N is one end of  $\underline{NAx}$  this can be found using the vector projection of  $\underline{CenN}$  onto the pore axis which is calculated using:

$$(\underline{CenN} \cdot \underline{Ax}) \underline{Ax}$$

Where  $\underline{Ax}$  is the pore axis unit vector. As this is the vector from Cen to closest point on  $\underline{Ax}$  to N the vector from N its closest point on  $\underline{Ax}$  is given by:

$$\underline{NAx} = \underline{N} - \underline{Cen} + (\underline{CenN} \cdot \underline{Ax}) \underline{Ax}$$

The same process can be used to obtain  $\underline{CAx}$  the shortest vector from C to  $\underline{Ax}$ . As  $\underline{NAx}$  and  $\underline{CAx}$  are both by definition perpendicular to the pore axis  $\underline{NC}_\perp$  is simply  $\underline{NAx} - \underline{CAx}$  as shown in figure 3.  $\theta_s$  itself is calculated using the dot product of  $\underline{NAx}$  and  $\underline{NC}_\perp$  as described for  $\theta_t$ .

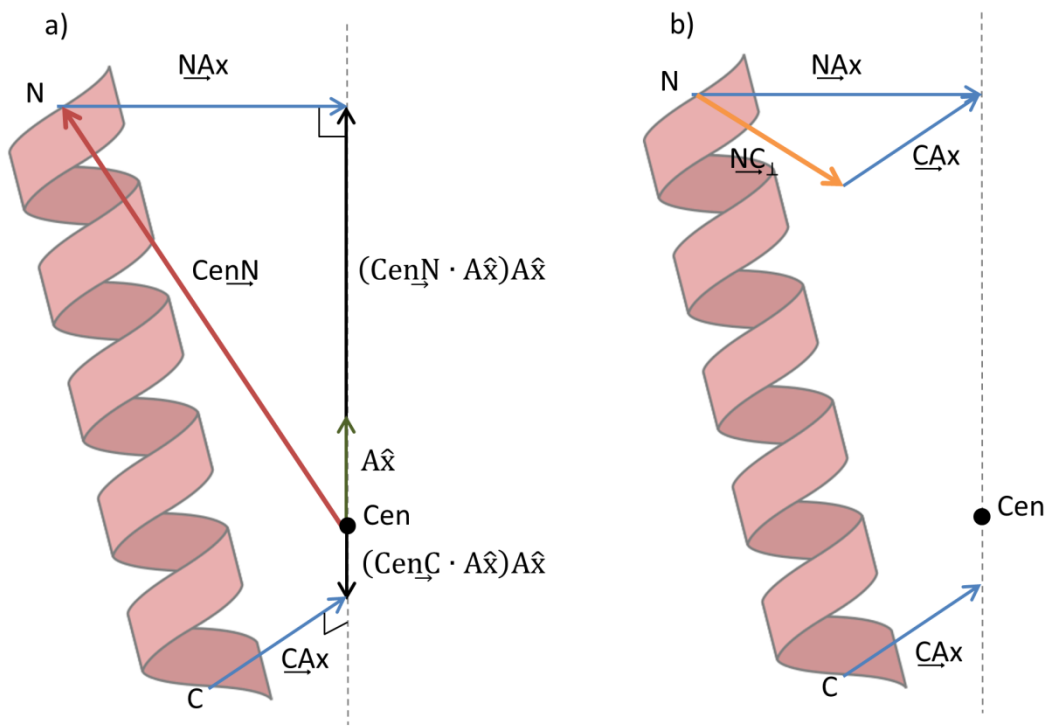


**Figure 3. Calculation of the vectors required for swing determination.** a) The shortest vectors from the ends of the helix ( $\underline{N_{Ax}}$  and  $\underline{C_{Ax}}$ , blue arrows) to the pore axis (grey dashed lines) are shown. These are calculated using the vector projection of the vector from the centre of the pore ( $Cen$ ) to the helix ends (red arrow) onto the pore axis. The vector projections for each end of the helix are shown as black arrows with the unit vector for the axis ( $A\hat{x}$ ) shown as a green arrow. b) The component of the helical axis perpendicular to the pore axis ( $\underline{N_{C_{\perp}}}$ , orange arrow) is displayed with its' derivation by subtracting  $\underline{C_{Ax}}$  from  $\underline{N_{Ax}}$ .

## User interface

AnglerFish is a web-based tool where users upload the file of interest (in protein data bank (PDB) format (*Berman et al., 2000*) and enter the residue numbers of the ends of the transmembrane helix of interest. In order to maintain the symmetry required for axis definition, the PDB file must be of a homo-multimer with each of the different chains containing corresponding residues numbered in the same way. The user is provided with the tilt and swing angles for the defined helix in each of the polypeptide chains in the file and an indication of which residues were used to define the pore axis.

There are several extra options to aid the systematic analysis of related structures. The user may manually select the residue to use for pore axis definition, to ensure the same residue is used between structures. Under the 'advanced options' tab, there are extra fields for 'model number' to use when the coordinates file contains multiple structures. By default if a best model remark is present in the header that model number will be used, in the absence of this the first model is used. The optional 'chains to use' field can be used to specify which of the chains to include in the calculation, in case the file contains chains that do not comprise the pore. The chains to use field also defines the order the chains are considered, so changing the order of the first three chains may be used to switch the definition of 'up' for the pore (see axis calculation above). If the calculation fails, a warning page is displayed detailing any co-ordinates specified from the input that could not be found within the file.

## Results

### Identifying the kinked helix in the NaK channel

The sodium and potassium conducting (NaK) channel is a homotetramer (*Shi et al., 2006*) for which open and closed structures available (*Alam and Jiang, 2009*). It is gated by changes around a hinge residue, glycine 87, in the pore-lining helix, which induce a kink, leading to opening of the pore. To parameterise and visualise (figure 4) the kink in the NaK channel, tilt and swing values were calculated for the helical segments before and after the kink in the open and closed structures (PDBIDs 3e83 and 2ahy, respectively). The largest difference in tilt (of 22.6° and 60.3° [green highlight]) before and after the kink is seen when the kink is defined between residues 87 and 88, showing this is the position of the kink. It should be noted that when comparing helical segments before and after a kink in the same helix, only the tilt should be considered. This is because swing is affected by the proximity of the helix to the centre of the pore, so will be different at different

positions within a completely straight helix. Comparison of the post kink helical segment with the corresponding section in the closed structure shows the opening is associated with a change in tilt of  $33.6^\circ$  and a change in swing of  $31.6^\circ$  [red vs. green overlays]. In comparison, analysing the internal surface (Figure 4b) using HOLE (*Smart et al., 1996*) indicates the dilation of the internal pore. This reveals the dilation in the activation gate occurs further down the protein from the kink. This shows the complementarity of AnglerFish to existing methods with AnglerFish giving the changes in helical orientation which lead to changes in pore diameter calculable by methods such as HOLE.

a)

Structure	Helix Residues	Chain								Average	
		A		B		C		D		$\theta_t$	$\theta_s$
		$\theta_t$	$\theta_s$	$\theta_t$	$\theta_s$	$\theta_t$	$\theta_s$	$\theta_t$	$\theta_s$		
2ahy closed	74-102	25.92	22.19	26.21	21.24	25.92	22.19	26.21	21.24	26.06	21.72
	74-87	24.93	18.88	24.96	17.87	24.93	18.88	24.96	17.87	24.94	18.38
	88-102	26.37	42.32	26.94	40.69	26.37	42.32	26.94	40.69	26.66	41.51
3e83 open	74-102	44.09	37.21	44.09	37.21	44.09	37.21	44.09	37.21	44.09	37.21
	74-87	22.63	24.25	22.63	24.25	22.63	24.25	22.63	24.25	22.63	24.25
	88-102	60.34	73.84	60.34	73.84	60.34	73.84	60.34	73.84	60.34	73.84

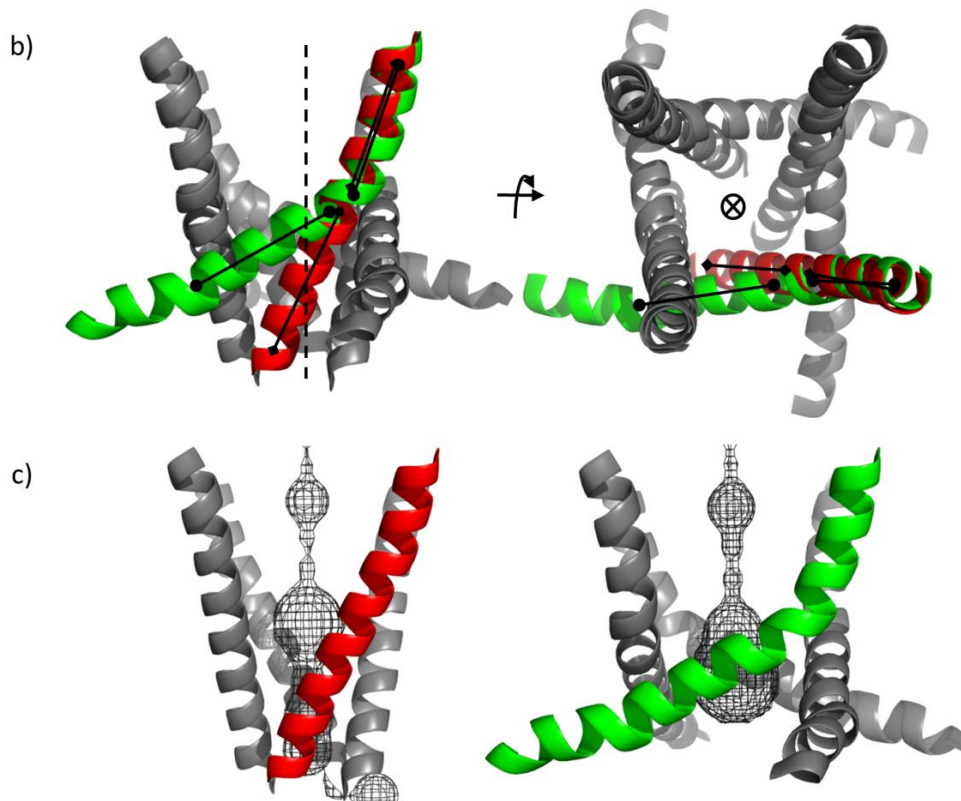


**Figure 4. Anglerfish used to investigate the kinking of the pore helix of the NaK channel.** a) Tilt ( $\theta_t$ ) and swing ( $\theta_s$ ) values for the NaK channel pore helix and its' pre and post helix sections. These were calculated for the closed (PDB 2ahy) and open (3e83) crystal structures. b) Pre- and post- kink helix axes are plotted on an overlay of the open (one chain is depicted in green with circular capped axes) and closed (one chain is depicted in red with diamond capped axes) NaK structures. The superposition was performed using the PyMol "super" command. The pore axis is shown as a dotted line in the left panel and a crossed circle in the right panel (90 degree view). c) The internal surface dimensions of the NaK channel pore as calculated using HOLE (Smart et al., 1996), and depicted as a wire mesh inside the closed and open structures, with the chains coloured as in b).

## Comparison of open and closed GLIC structures

The prokaryotic ligand gated ion channel (GLIC) is a homopentamer which forms a proton-gated cation channel. GLIC is of particular interest because of its homology to eukaryotic acetylcholine receptors; like acetylcholine receptors GLIC is a target of general anaesthetics. Co-crystallization of GLIC with the general anaesthetic Xenon produced a closed form of the channel (PDBID 4zzb) which can be used for direct comparison with the open channel (PDBID 4zzc) to investigate the structural changes involved in gating (*Sauguet et al., 2016*). AnglerFish was used to calculate (Figure 5) tilt and swing values for all four helices of the GLIC channel in the closed and open conformations. Comparisons show that the second helix (residues 221-241) in all monomers undergoes the greatest change between the open and closed structures (the difference between red and green highlights). The difference is primarily a change in swing of the helix of  $86.5^\circ$ . This shows the importance of defining the orientation of the helices by both tilt and swing, as the modest difference in tilt between the structures would not fully explain the channel opening. It is possible this structural change is being achieved by a change in tilt as a helix that changes tilt past the pore axis by the angle of the original tilt will have the same tilt value as it started with. This is because tilt does not take into account the relative position of the helix. Such a helix will however have a swing that differs by  $180^\circ$  as the opposite end of the helix will now be closer to the center of the pore.

a)

Structure	Helix Residues	Chain										Average	
		A		B		C		D		E		$\theta_t$	$\theta_s$
		$\theta_t$	$\theta_s$										
4ZZB	202-217	14.0	-66.0	14.9	-66.6	14.9	-66.0	15.0	-68.3	15.2	-65.0	14.0±0.5	-66.0±1.2
	221-241	170.6	73.4	170.7	72.0	170.8	73.8	170.5	71.8	170.7	74.3	170.7±0.1	73.3±1.1
	254-281	16.0	-53.0	16.8	-53.2	16.7	-52.6	16.9	-53.7	17.1	-52.5	16.9±0.4	-53.0±0.5
	285-314	161.5	135.7	161.6	136.7	161.7	137.1	161.6	135.3	161.1	135.7	161.5±0.2	136.1±0.8
4ZZC	202-217	12.5	-67.8	12.4	-67.4	12.5	-67.5	12.2	-67.8	12.4	-68.9	12.4±0.1	-67.9±0.6
	221-241	174.7	157.0	174.5	157.4	174.5	158.6	174.7	161.2	174.8	159.3	174.6±0.1	158.9±1.6
	254-281	17.1	-45.1	16.0	-45.1	17.1	-44.5	16.0	-44.5	16.8	-45.3	16.0±0.6	-44.9±0.4
	285-314	160.8	146.3	160.8	146.4	160.6	146.8	160.6	147.4	160.9	146.5	160.8±0.1	146.7±0.4

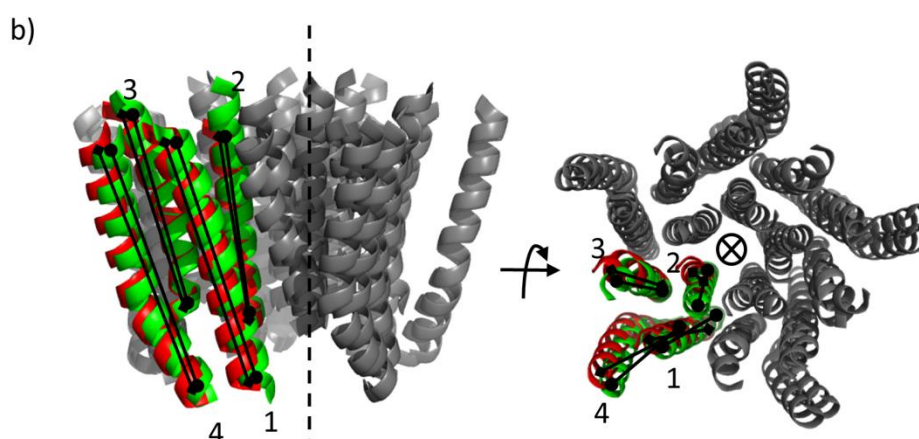


**Figure 5. Anglerfish used to investigate the gating of the GLIC ion channel.** a) Tilt ( $\theta_t$ ) and swing ( $\theta_s$ ) values for the four transmembrane helices of GLIC. These were calculated for the closed (PDBID 4zzb) and open (3e83) crystal structures. Averages are stated with errors of two standard deviations of the mean. b) Helical axes plotted on the overlaid closed (in red with diamond capped axes) and open (in green with circle capped axes) structures; the helices are numbered as in order from N to C termini. Superposition was performed using the Pymol "super" command. The pore axis is shown as a dotted line and circled cross.

## Prokaryotic voltage-gated sodium channels

The first open structure sodium channel structure (*McCusker et al., 2012*) solved that was of the Na<sub>v</sub>Ms pore. This structure showed the pore to be asymmetric, with the gate partially open, as a consequence of a different psi angle in one (chain A) of the S6 helices monomers. From this a model of the fully open pore was made by creating a tetramer of subunits in the conformation of chain A. A later structure of the Na<sub>v</sub>Ms pore (*Bagnéris et al., 2013*) depicted the symmetric conformation of a fully open pore. In order to demonstrate the asymmetry of the partially-open pore (PDBID 4f4l), tilt and swing values were calculated for each chain. Because chain A corresponded to the altered conformation, chains B, C and D were used to define the pore axis; had all chains been used, they would have skewed the orientation of the axis. Tilt and swing values for chain A were 141.0° and 27.2°, respectively, which fall outside two standard deviations of the mean for chains B, C and D ( $142 \pm 0.9^\circ$  and  $22.3 \pm 0.8^\circ$ ), confirming that chain A is significantly different. The symmetric open pore (PDBID 3zjz) gave tilt and swing values 140.1 and 26.7, respectively, for all 4 chains. This shows that chain A of the partially open pore is more representative of the fully open conformation, validating the initial fully open model. This can be seen in figure 6 where in a superposition of the partially and fully open pores chain A of 4f4l shows the best overlay with its' equivalent in 3zjz. This shows AnglerFish's utility in characterising an asymmetric pore, as tilt and swing values are returned for each chain individually. This will work as long as there is a set of at least 3 chains with a region ordered with respect to the pore axis, i.e. contains a residue number that forms a plane perpendicular to the pore axis.

a)

Structure	Helix Residues	Chain							
		A		B		C		D	
		$\theta_t$	$\theta_s$	$\theta_t$	$\theta_s$	$\theta_t$	$\theta_s$	$\theta_t$	$\theta_s$
4f4l	70-90	141.0	27.2	142.1	23.0	143.3	22.3	141.6	21.5
3zjz	70-90	140.1	26.7	140.2	26.7	140.1	26.7	140.2	26.7

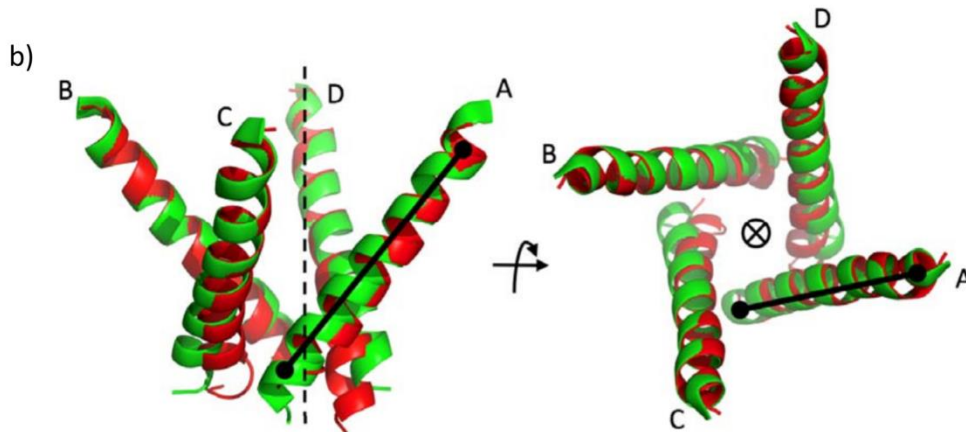


**Figure 6. Anglerfish used to compare the asymmetric and symmetric NaVMs pore structures.** a) Tilt ( $\theta_t$ ) and swing ( $\theta_s$ ) values for the S6 helix of NaVMs. These were calculated for the partially (PDBID 4f4l) and fully (3zjz) open crystal structures. Partially (red) and fully (green) open NaVMs structures overlaid, with the chains letters as in a). The helical axis for chain A is shown as the solid black line, the other chains are lettered at their N termini showing their deviation compared to chain A. The superposition was performed using the Pymol "super" command. The pore axis is shown as a dotted line in the left panel and a circled cross in the right panel.

As there are multiple prokaryotic Na<sub>v</sub> crystal structures in different conformations Anglerfish may be used to assess the difference in tilt and swing expected upon gating. Tilt and swing values were calculated for the S5 and S6 helices of the Na<sub>v</sub>Ms pore (Bagnéris *et al.*, 2013), full length Na<sub>v</sub>Ms (Sula *et al.*, 2017), Na<sub>v</sub>Rh (Zhang *et al.*, 2012), Na<sub>v</sub>Ae (Shaya *et al.*, 2014), Na<sub>v</sub>Ab (Payandeh *et al.*, 2011) and, constitutively open and closed mutants of Na<sub>v</sub>Ab (Lanaeus *et al.*, 2017). Of these the Na<sub>v</sub>Ms pore, Na<sub>v</sub>Ms full length and the truncation mutant of Na<sub>v</sub>Ab contain open pores while the rest are closed. The plotted tilt and swing values in figure 5 show there is little correlation between the orientation of S5 and gating. This stands to reason as S5 is further from the ion conducting pore and does not contain the gate, and while it may be expected to transfer motion from the voltage sensors this information may be lost with the information available as the Na<sub>v</sub>Ms pore and Na<sub>v</sub>Ae structures lack voltage sensors and, the Na<sub>v</sub>Ab structure contains the voltage sensor in a different functional state to the pore. The S6 tilt and swing values show channel closing is correlated with a change decrease in tilt (of ~ 5-15°). There is a less clear trend in swing indicating the tilt is the dominant change. It should however be noted that as the calculation of swing is strongly dependent on the start and end positions of the helices it may be less relevant comparing structures of different sequences. This is because while different structures may have their corresponding helical axes in the same direction but the value for swing could differ with secondary structure. This would be if their secondary structure was different such that a helix started or stopped closer to or further from the centre of the pore.

## Conclusions

AnglerFish provides a useful tool for parameterising helical geometry in membrane proteins, especially for defining structural differences associated with conformational changes. It can be used to define the orientation of a helix about a defined axis in the protein, and can be used on multimeric proteins to probe both symmetric and asymmetric changes that occur in different subunits. It therefore provides a novel quantitative means of defining parameters associated with predominantly helical membrane proteins, such as channels and transporters. The method is however not universally applicable to  $\alpha$ -helices as it requires at least 3-fold rotational symmetry, not including helical symmetry excluding many Helicases and other DNA binding proteins. The approximation to find the axis of an  $\alpha$ -helix also means that the system will be inaccurate for any helix less than 8 residues, both excluding short helices and helices that kink in sections of 8 or fewer residues.

# Expression and purification of Na<sub>v</sub>Ms constructs

---

## Introduction to techniques

The main advantage in using bacterial Na<sub>v</sub>s is their ability to be expressed and purified heterologously from laboratory *E.coli* strains (*Charalambous et al., 2011*). This allows the cells to be grown quickly, in a manner that can be easily scaled up. Extra constructs can be produced, including the addition of affinity tags by simple cloning and mutagenesis of plasmid vectors. The overexpression of membrane proteins in *E.coli* has been shown to cause toxicity by overloading the Sec-translocon which disrupts the insertion of host proteins and causes misfolded proteins to aggregate in the cytoplasm (*Wagner et al., 2008*). Strains for membrane protein over-expression have been developed including C41 and C43 derived from BL21(DE3) cells which are more tolerant of a range of membrane proteins (*Miroux and Walker, 1996*).

When a protein is expressed using *E.coli* as a host organism it can be purified from one of four fractions, soluble in the cytoplasm, secreted into the growth medium, insoluble in inclusion bodies or associated with the membrane. As Na<sub>v</sub>s are membrane proteins this limits their location to the membrane or misfolded in inclusion bodies. Due to the increase in purification steps required to refold proteins and the difficulty of assessing if a native fold has been achieved, it is preferable to purify from the membrane fraction where possible (*Rogl et al., 1998*). In order to purify proteins from a membrane they must first be solubilised. This is usually achieved using amphipathic detergents (*Arachea et al., 2012*). In aqueous solution, detergents exist in an equilibrium between individual detergent molecules and micelles with the hydrophobic tails inside and the polar/ionic head-groups exposed to water. When solubilising membrane proteins this allows the transmembrane segments to be exposed to a hydrophobic environment while the extra membranous regions are solvent-exposed outside of the micelle. As the lipid environment can alter the properties of membrane proteins including the activity of ion channels (*D'Avanzo et al., 2013*), the selection of a suitable detergent is vital in ensuring downstream applications are characterising native properties of a channel. A suitable detergent can ensure this either by mimicking the properties of native lipids or by only partially dilipidating proteins leaving functionally important lipids bound (*Kalipatnapu et al., 2005*). Detergents vary in shape and charge of their hydrophobic head groups as well as their hydrophobic tails. These affect the physical properties of the detergent including the aggregation number (number of detergent molecules per micelle) and critical micelle concentration (cmc, concentration above which detergent molecules will form micelles). These

factors will affect how a detergent will solubilise a membrane protein. While solubilising the protein of interest is required; detergents that solubilise very efficiently are also likely to disrupt the fold of membrane proteins by disrupting complexes, the hydrophobic packing or required native lipids (Seddon *et al.*, 2004). Non-ionic detergents including the maltosides have been shown to solubilise a wide range of membrane proteins non-disruptively compared to harsher ionic detergents. These can be used at high concentration to allow efficient solubilisation before reducing the detergent level to decrease the proportion of free micelles (Seddon *et al.*, 2004).

The addition of a polyhistidine tag allows the use of immobilised metal affinity chromatography, which can be performed either in batches or under a flow system using sepharose beads with bound  $\text{Ni}^{2+}$  ions. This is a versatile technique as the interaction persists in a wide range of pHs and buffers, including those with high concentrations of detergent, and is easily reversible by the use of a buffer containing imidazole. The addition of a terminal polyhistidine sequence rarely disrupts the structure or function of a protein and due to its hydrophilic nature can often aid solubility (Hengen *et al.*, 1995). Inclusion of a protease cleavage site between the tag and protein facilitates the tag's removal, which, in addition to confirming the tag has no significant effects on the protein, allows further removal of contaminants. This is possible as the major contaminants from the first step will have some affinity for  $\text{Ni}^{2+}$  so can be bound to the  $\text{Ni}^{2+}$  matrix while the de-tagged protein remains mobile (Hengen *et al.*, 1995).

Size exclusion chromatography is able to separate proteins based on their effective size in solution. This is achieved using beads consisting of a porous matrix where smaller molecules are able to freely diffuse into the matrix while larger molecules are excluded. The more freely a molecule can enter the matrix the larger the effective volume it will have to travel through, hence the later it will elute. Columns are available with beads of a range of different pore sizes, altering the range of protein dimensions which the column will separate (Barth *et al.*, 1994). As the technique separates on size rather than chemical nature it can be used to check the protein is in a single oligomeric state, by the presence of a single peak containing the target protein. Size exclusion is also an effective means of buffer exchange as any small molecules (such as imidazole reducing agents) present in the buffer the sample is loaded in but not the elution buffer will elute much later than the target protein; with the possible exception of any strong ligand interactions. This is of particular importance for voltage-gated sodium channels, checking that any changes to the purification or construct are not disrupting tetramer formation or causing the aggregation membrane proteins are prone to.

## Materials and Methods

Both the full length and pore-only Na<sub>v</sub>M channels had been cloned into the pET-15b vector (see appendix 1 for plasmid map) previously with and without the C-terminal coiled coil region. The vector contains an ampicillin resistance site and a lac promoter inducible by Isopropyl β-D-1-thiogalactopyranoside (IPTG).

Point mutagenesis was performed using the Quickchange method (Stratagene) using 1 μl Pfu Turbo polymerase (Thermo Scientific), the supplied manufacturer's buffer, 125 ng of each primer (synthesised by Eurofins Genomics), 1 μl of dNTP mix giving a final concentration of 200 μM (Thermo Scientific) in a 100 μl total reaction volume. The mixture was incubated with the following PCR temperature steps in a kryatech supercycler thermal cycler.

Temperature / °C	Duration / min:sec	Cycles
95	3:00	1
95	0:50	18
60	0:50	
68	7:00	
68	7:00	1
4	>10:00	Hold

The PCR reaction product was used to transform DH5α supercompetant cells (New England Biosciences) which were plated out onto LB agar plates containing 100 mM ampicillin. Single colonies were picked for growth and plasmid purification by miniprep (using a Quiagen kit). The desired mutations were verified by sequencing from myGATC using their pET-RP primers. Full DNA and protein sequences for the constructs used are shown in appendices 2 and 3.

The construct-containing vectors were used to transform C41 (DE3) expression cells. In a typical purification, 160 ml of starter culture was grown overnight and used to inoculate 16 l of LB broth containing 100 mM ampicillin. Cells were grown to an OD<sub>600</sub> of 0.8 to 1 at 37 °C before induction with 500 μM IPTG. The induced culture was grown for a further 3 hrs before pelleting the cells by centrifugation for 10 minutes at 5000 x g at 4 °C. Cell pellets were frozen at -80 °C before use.

Defrosted cell pellets were resuspended in 100 ml of tris buffered saline (TBS) pH 7.5 with 200  $\mu$ M PMSF, DNase1 and 250  $\mu$ M  $Mg_2SO_4$ , then lysed by 3-4 passes through an Emulsiflux C3 homogeniser. The lysis was performed keeping the sample on ice and cooling the Emulsiflux outlet by immersing a metal coil in ice water. Unlysed cells were removed by centrifugation for 30 minutes at 10,000 x g before pelleting the membranes at 131,000 x g for 3 hours both at 4 °C.

The membranes were resolubilised in 80 ml 1.5% DDM (n-Dodecyl-beta-Maltoside Detergent), 20 mM Tris, 200 mM NaCl with a hand held homogeniser and incubated at 4 °C for 1 hour with rotation before filtering with a 0.45  $\mu$ m filter (Cole-Parmer). The filtered sample was loaded onto a 1 ml Histrap column (GE life sciences) in the presence of 20 mM imidazole using a peristaltic pump (P-1 GE life sciences) at 1 ml/min to pass over the column twice at 4 °C. The protein bound to the Histrap was separated on an Äkta chromatography system washed by a gradient of 8 to 100 mM imidazole over 10 column volumes and held until all contaminants at that concentration have unbound before eluting the protein with 500 mM imidazole all in pH 7.5, 20 mM Tris, 200 mM NaCl with the detergent at 2 times its critical micelle concentration. The 500 mM imidazole elutions are then pooled and the imidazole removed by concentrating to < 0.5 ml and diluting with imidazole-free buffer to 15 ml before concentrating back to < 1 ml in a 50 kDa molecular weight cut off spin concentrator (Millipore). Spin concentration was performed at 4 °C and 3,800 x g

So that the molecular weights of proteins eluting from the size exclusion step could be estimated the Gel Filtration Molecular Weight Markers 12-200 kDa (Sigma Aldrich) proteins were run on the same set up. A plot of their elution volumes against their molecular weights is shown in Appendix 4.

The His tag was removed by thrombin cleavage for 1 day at room temperature with 40  $\mu$ l of thrombin (50 Units) (Novagen) with the manufacturer's buffer in a 2 ml total volume. The products of the cleavage reaction were then bound to a second Histrap again by peristaltic pump on ice. The sample eluted with 40 mM imidazole while the contaminants remained bound using an Äkta chromatography system. Finally the sample is concentrated as before to a volume of < 200  $\mu$ l. on the concentrated sample was loaded onto a 24 ml S200 sephadex size exclusion column (GE life sciences) by injection from a 500  $\mu$ l loop and run at 0.5 ml/min. The peak fractions were pooled to ensure the sample consists of tetramer but not aggregated protein.

SDS poly acrylamide gel electrophoresis (SDS-PAGE) was performed to check for sample purity. 10  $\mu$ l samples were mixed with 5  $\mu$ l of 3 x loading dye containing 10 mM DTT (bio-rad) and heated to 90 °C for 10 minutes before loading onto 4-12% Bis-Tris gels (Novex). These were run at 200 V for 45 min in MES buffer (Thermo Scientific) for the full lengths and 200 V for 35 min in MOPS

buffer (Thermo Scientific) for the pore. Gels were stained using InstantBlue coomassie stain (Expedeon) for at least 30 minutes and destained in deionised water for at least 2 hours.

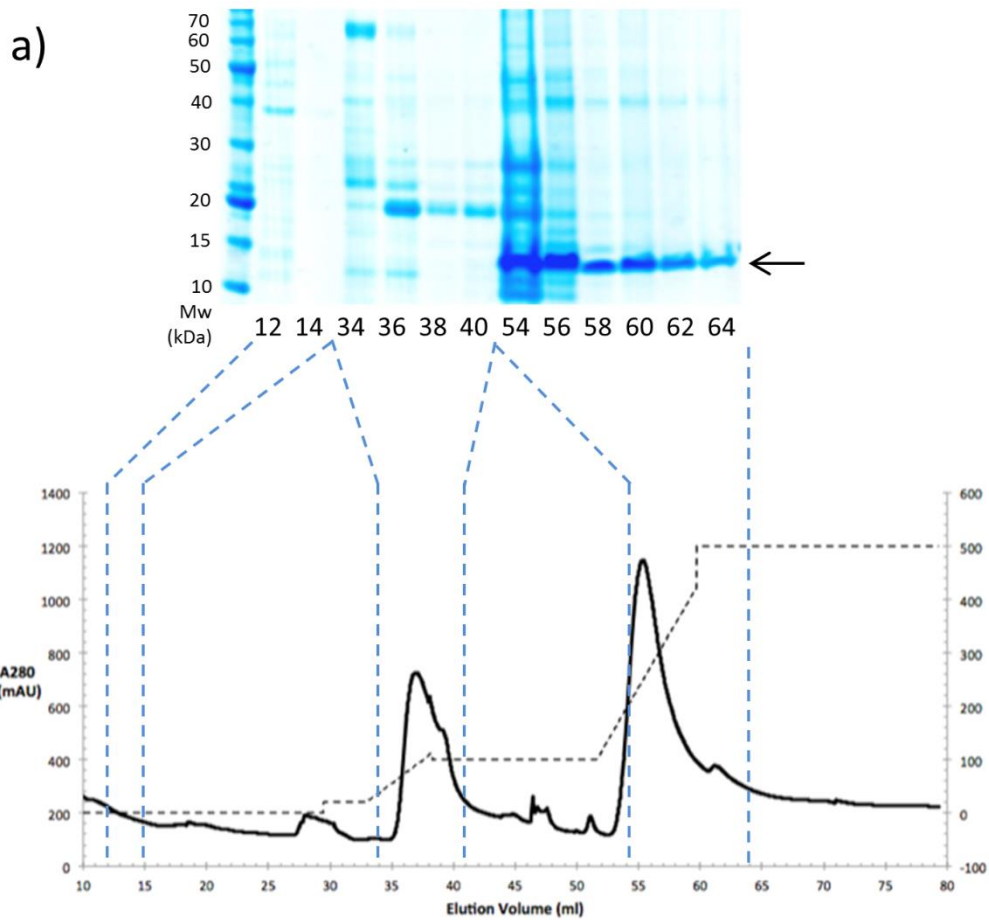
Western blots were performed using the iBlot system (Invitrogen) to transfer proteins to polyvinyl difluoride membranes. After transfer the membranes were blocked with a 5% rehydrated milk solution for 1 hour. The blocked membranes were then incubated with monoclonal anti-polyhis-alkaline phosphatase antibody (Sigma-Aldrich) in TBS, 0.1% Tween, 0.5% rehydrated milk overnight at 4 °C. Membranes were then developed using BCIP/NBT FAST alkaline phosphatase substrates (Sigma-Aldrich), according to the manufacturer's instructions.

Mass spectrometry was performed (by the PNAC Facility, University of Cambridge) on bands excised from SDS-PAGE Gels.

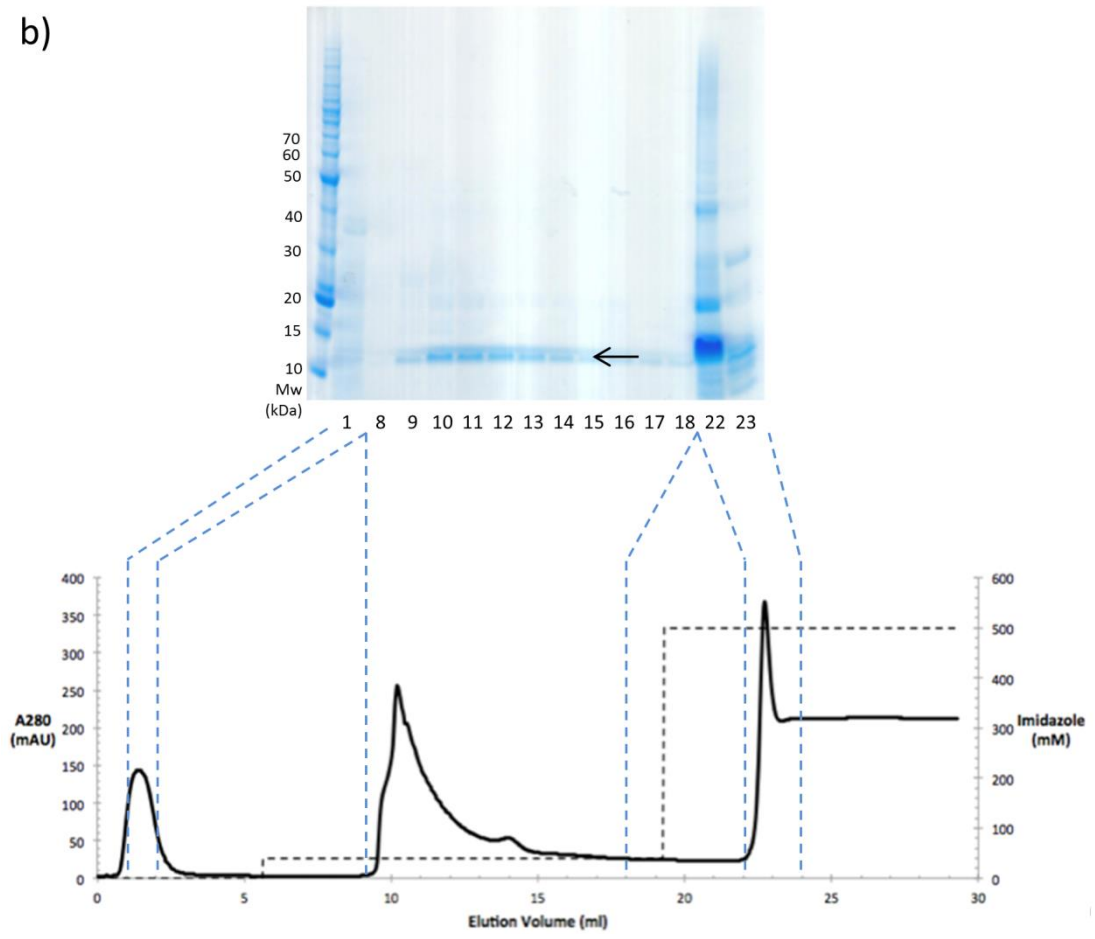
## Results

The Na<sub>v</sub>Ms pore (residues 130-274) was successfully expressed and purified as previously described (*Bagneris et al. 2013*). A truncation of the Na<sub>v</sub>Ms pore was also created by mutation of glutamate 238 to a stop codon which could also be purified to single band purity as shown in Figure 1. After cell lysis and re-solubilisation of the membranes in DDM this purification starts with nickel affinity chromatography where nickel binding contaminants are eluted with a 100 mM imidazole wash and then the protein is eluted by a gradient to 500 mM imidazole (figure 1a bottom). After this step the SDS-PAGE gel (figure a) top shows a strong band between 10 and 15kDa corresponding to the Na<sub>v</sub>Ms pore but many contaminants also. This is followed by a thrombin cleavage step to remove the His tag, in the figure 1a) example fractions from 55-67 ml would be pooled and concentrated. After thrombin cleavage the protein was re-bound to a nickel column and eluted as shown in figure 1b). Here the fraction at 1 ml represents the unbound protein and the fractions from 10-14 ml would be pooled for size exclusion. On close examination of the Na<sub>v</sub>Ms band it looks as if it may be doublet indicating the thrombin cleavage is incomplete. As the higher band is much fainter than the lower monomers with a His tag are a small minority, so unless thrombin cleavage is cooperative it is very unlikely for a Na<sub>v</sub>Ms tetramer to have more than one His tag if any. This explains why His tagged Na<sub>v</sub>Ms would elute at a much lower imidazole concentration in the second affinity step as with few histidine rich sequences it will have a lower avidity. The cleaved Na<sub>v</sub>Ms pore elutes from a size exclusion column at a volume of 12.75 ml (figure 1c) with a shoulder from a faint 20 kDa contaminant (figure 1c top) at 11-12 ml. The peak at 12.75ml is equivalent to a molecular weight of 148 kDa as determined by molecular weight standards (appendix 4), this is much higher than the 50

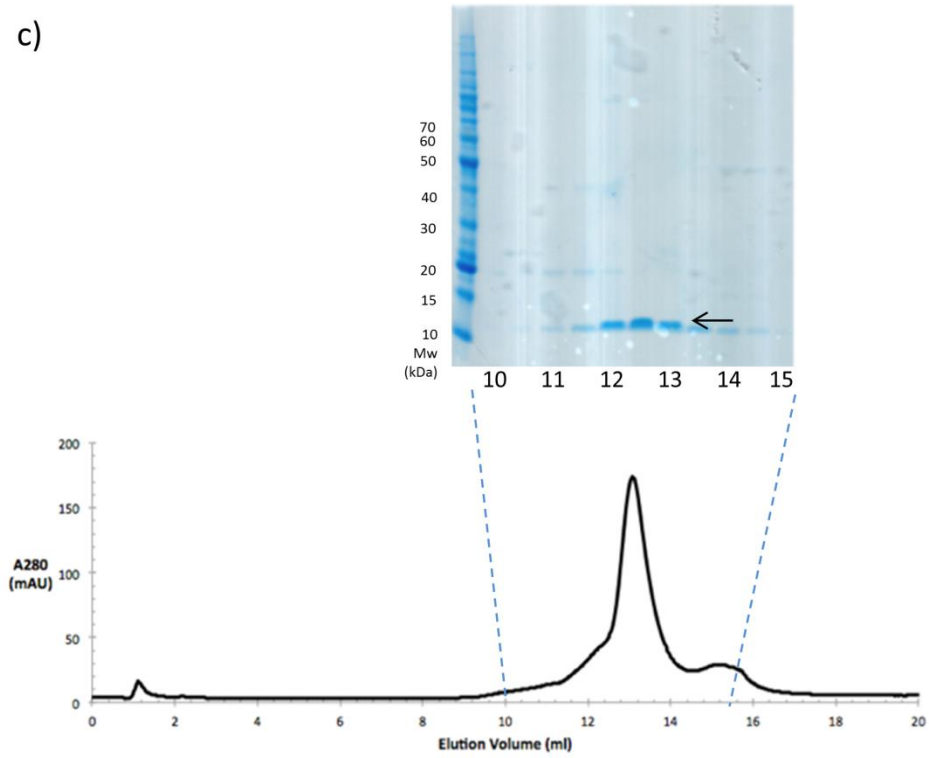
kDa expected for a tetramer of this construct, this could reflect the shape of the protein in a detergent micelle giving it a much larger effective hydrodynamic radius. While the mass of a micelle could usually be added to the protein to estimate this HEGA-10 does not have a reported aggregation number (Anatrace detergent properties data sheet) indicating it is very low (below 10). For HEGA-10 to effectively solubilise a membrane protein there would need to be detergent covering the external hydrophobic surfaces indicating more detergent molecules would associate to the protein than the detergent's aggregation number; this makes the effective mass and dimensions of  $N_{AV}Ms$  associated to HEGA-10 very difficult to estimate. There is a further peak at 15.5 ml with no corresponding protein band on the SDS-PAGE gel, this is odd as you would expect that and imidazole (the only buffer component used that absorbs at 228 nm) to elute at the end of the column's volume of 24 ml. It is possible that this peak represents micelles containing imidazole but this too seems unlikely as imidazole is water soluble and the detergent is free to exchange between micelles.



b)



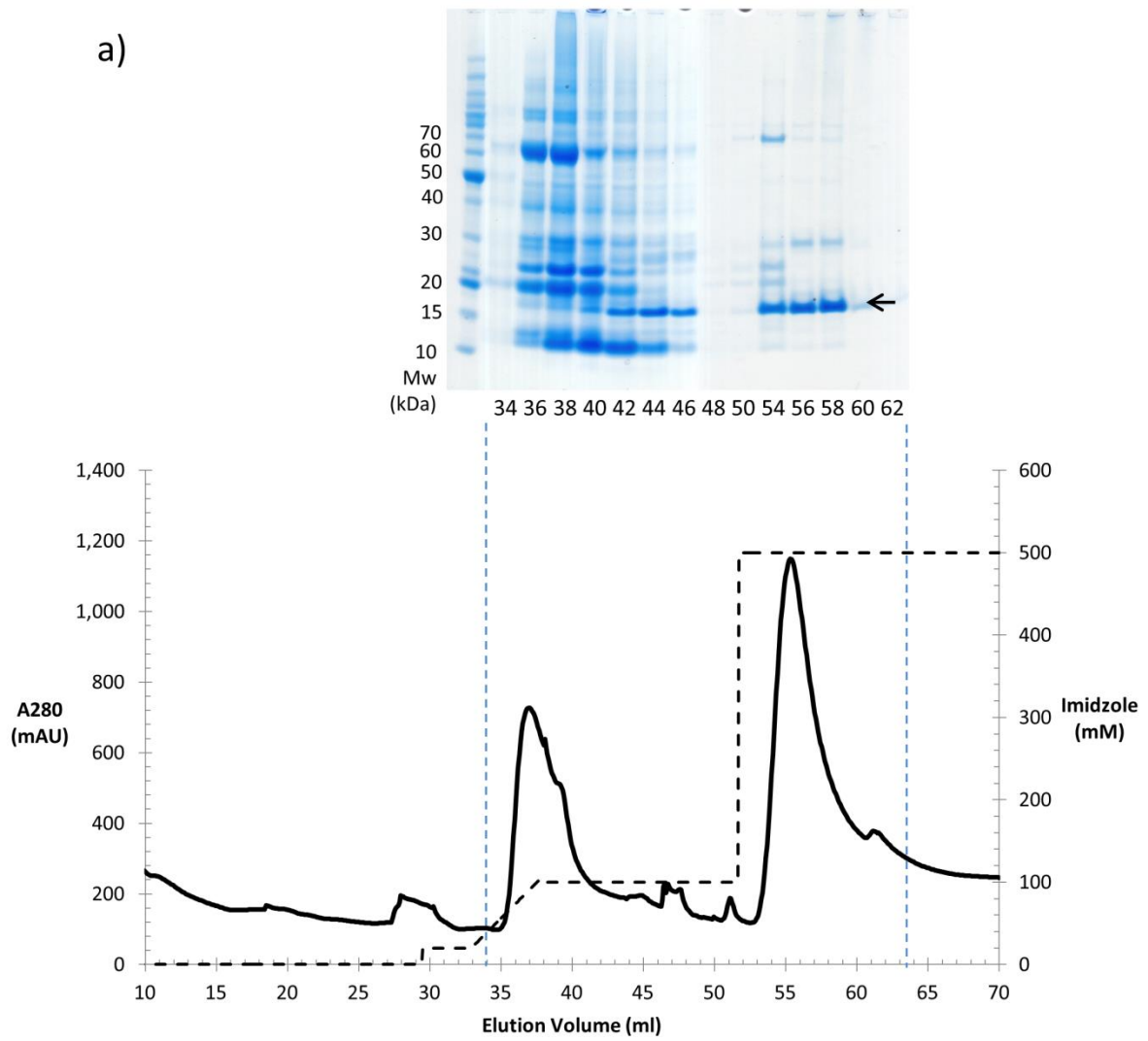
c)



**Figure 1. An example purification of the Na<sub>v</sub>Ms pore.** Chromatograms (left) and reducing SDS PAGE gels (right) are shown for a) the initial elution from a nickel column, b) the rebinding and elution from a nickel column after thrombin cleavage and c) the separation from an S200 size exclusion column. The UV absorbance at 280 nm and imidazole concentration are shown as solid and dashed lines, respectively. Lanes in the SDS PAGE gels are marked with the elution volume of the sample from the corresponding chromatogram and the Na<sub>v</sub>Ms pore is the band present at ~11 kDa and marked by an arrow.

The mutation A221C was created to introduce a cysteine to the bottom of S6 (in a construct without the glutamate 238 truncation), this was to create an anchor point for the conjugation of dye species to monitor the gating of the channel by single molecule FRET. This mutant was purified (figure 2) without the thrombin cleavage step in order to leave the His tag for purification from excess compounds used for cysteine labelling. When the SDS-PAGE gel of the final size exclusion step for this mutant is compared with that of the wild type, the lack of a reverse IMAC step has led to some minor contaminants within the preparation. Namely a minor band above the 15 kDa band of the sample and a fainter band at 25-30 kDa are visible. The contaminant at 15 kDa is reminiscent of the doublet in figure 1 indicating it may not be caused by incomplete thrombin cleavage. For the minor contaminants to affect the FRET experiments they would either need to contain sterically accessible cysteine residues that become labelled, or interact with Na<sub>v</sub>Ms. The labelling of contaminants was checked for by fluorescence gel prior to FRET measurements (see FRET chapter). As single molecule FRET experiments occur at the picomolar concentration range for an interacting protein to be an issue it would have to be a protein with a very strong and specific interaction with Na<sub>v</sub>Ms. No such protein is known within the *E.coli* proteome and as *E.coli* has no voltage gated sodium channels of its' own this seems unlikely (UniProt proteome ID UP000000625).

a)



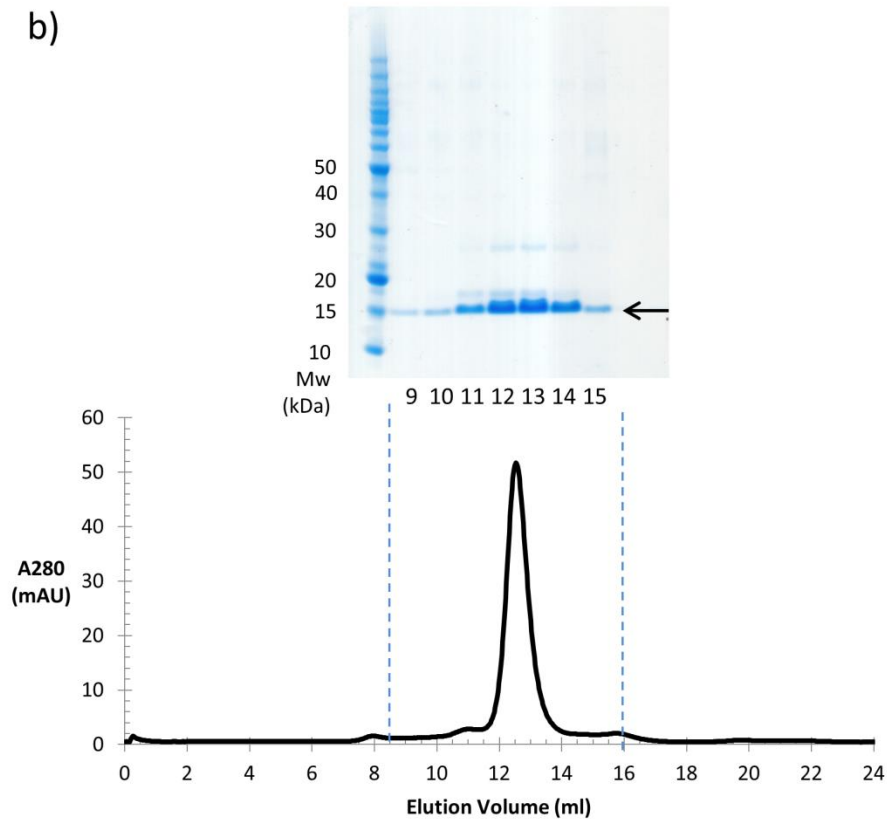
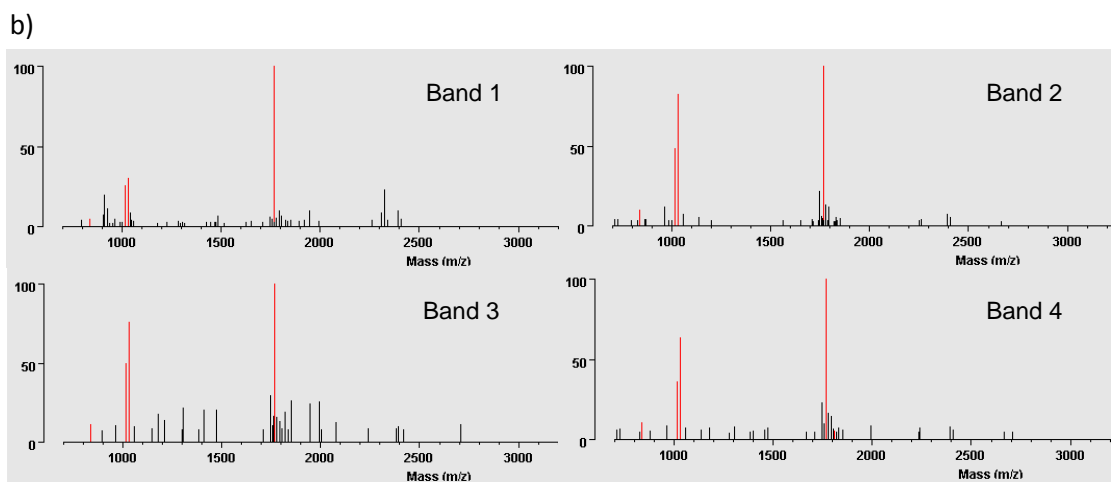
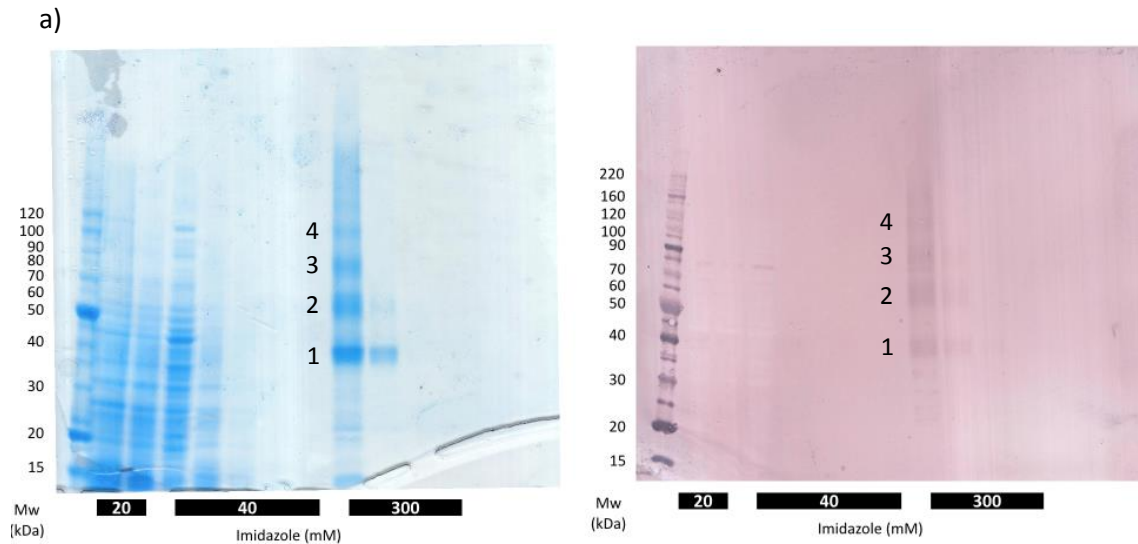


**Figure 2. An example purification of the  $Na_vMs$  pore A221C mutation.** Chromatograms (left) and reducing SDS PAGE gels (right) are shown for a) the elution from a nickel column and b) the separation from an S200 size exclusion column. The UV absorbance at 280 nm and imidazole concentration are shown as solid and dashed lines respectively. Lanes in the SDS PAGE gels are marked with the elution volume of the sample from the corresponding chromatogram and the  $Na_vMs$  A221C is the band present at ~15 kDa and marked by an arrow.

Purification of the full length Na<sub>v</sub>Ms (with the voltage sensor domain) was attempted using the same strategy as the pore construct. While some positive bands were present on a western blot using an anti-poly histidine antibody. These were not at the expected molecular weight or reproducible. These bands were likely due to non-specific binding of histidine rich *E.coli* proteins to the Ni<sup>2+</sup> beads and anti-poly his antibody. The purification was optimised to prevent enzymatic degradation of the protein after lysis. This was achieved by performing the purification at 4 °C and adding a protease inhibitor cocktail (cOmplete mini EDTA-free Roche) tablet (1 per 500 ml) to the buffers until the sample was bound to Ni<sup>2+</sup> and washed with 20 mM imidazole. This yielded reproducible bands on a western blot as shown in figure 3a.

While these bands were consistent between purifications it is odd that bands at several molecular weights appeared, as a protein in a reducing SDS PAGE gel would be expected to be denatured to a monomeric protein. It is also odd that the lowest molecular weight band appears around 40 kDa while the Na<sub>v</sub>Ms monomer should be ~30 kDa. In light of this each of the 4 bands visible on the western blot appearing in the 300 mM imidazole fractions were sent for identification by MALDI fingerprint mass spectrometry of the trypsin digest. Each gave 4 peaks corresponding to masses expected from a trypsin digest of Na<sub>v</sub>Ms (red lines in figure 3) and did not match those from known *E.coli* host proteins. These four peaks corresponded to peptides with less than a 50% coverage of the expected tryptic digest of Na<sub>v</sub>Ms, as shown on the sequence in figure 3. To confirm the identity of the bands as arising from Na<sub>v</sub>Ms, the sequence of the fragment expected to be “RLVSVIPTMRR” was checked by ESI mass spectrometry, which gave ions confirming this sequence.



1: **M**GS**S**HHHHHHSSGLV**P**RG**S**HMS**R**K**I**RD**L**IES**K**R**F**Q**N**V**I**T**A**  
 41: **I**IV**L**NG**A**VL**G**LL**T**DT**T**LS**A**SS**Q**N**L**LER**V**D**Q**L**C**L**T**I**F**I**V**E**I**  
 81: **S**L**K**I**Y**A**Y**G**V**R**G**FF**R**SG**W**N**L**FD**F**V**I**V**A**I**A**LM**P**A**Q**G**S**L**S**V**L**R  
 121: **T**FR**I**FR**V**M**R**L**V**S**V**I**P**T**M**R**R**V**V**Q**G**M**L**L**A**L**P**G**V**G**S**V**A**ALL**T**V  
 161: **V**F**Y**I**A**AV**M**AT**N**LY**G**AT**F**PE**W**FG**D**LS**K**S**L**Y**T**L**F**Q**V**M**T**LES**W**  
 201: **S**M**G**IV**R**P**V**M**N**V**H**PN**A**W**V**FF**I**P**F**IM**L**TT**F**TV**L**N**L**FI**G**I**I**VD  
 241: **A**MA**I**T**K**E**Q**EEEE**A**K**T**G**H**H

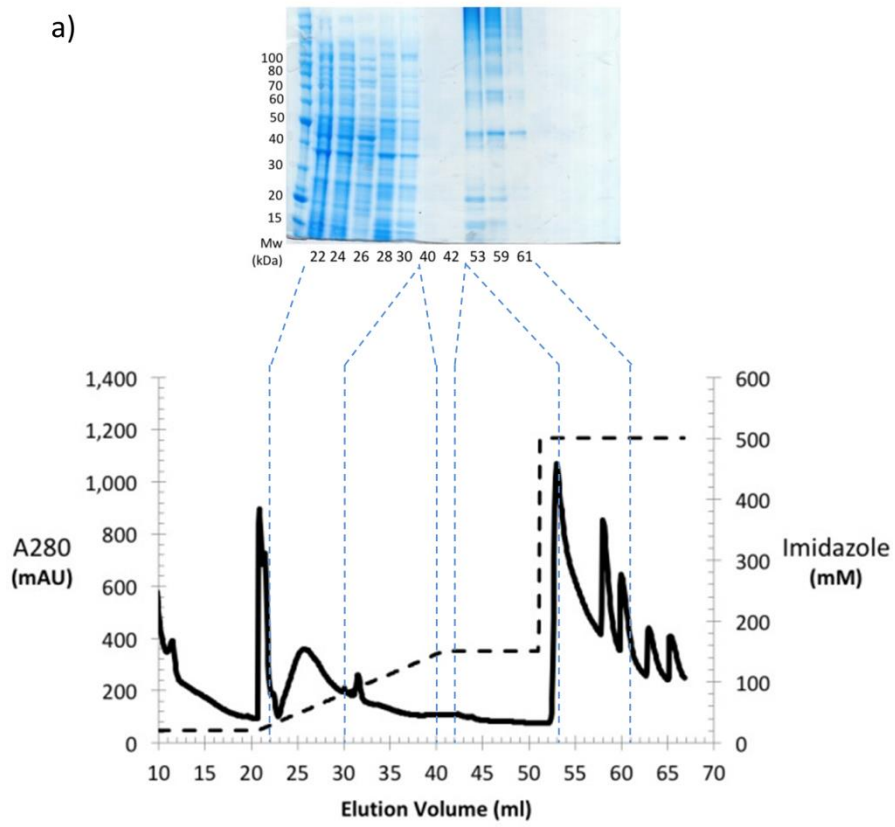
**Figure 3. Identification of the full length Na<sub>v</sub>Ms by mass spectrometry** a) coomassie stained SDS PAGE gel (left) and using an Anti-poly His western blot (right) of a Na<sub>v</sub>Ms batch purification using Nickel sepharose beads washed in buffer containing the indicated imidazole concentrations. Bands sent for mass spectrometry are numbered 1-4. b) Tryptic digest MALDI fingerprint spectra of the bands numbered above with peaks corresponding to Na<sub>v</sub>Ms fragments coloured red (above) and trypsin peaks omitted. Na<sub>v</sub>Ms sequence coloured to show coverage possible tryptic digest fragments with observed fragments shown in red, fragments too small large or acidic blue, and expected unobserved fragments shown in yellow.

Given the positive identification of Na<sub>v</sub>Ms by mass spectrometry, it is reasonable to assign the four bands as monomers, dimers trimers and tetramers of Na<sub>v</sub>Ms. This shows the tetramer is stable enough to partially resist denaturation by SDS. Incomplete denaturation of membrane proteins by SDS is common (*Rath et al., 2009*) and also explains why the protein does not migrate its' molecular weight. This is because incompletely denatured protein will provide a smaller surface area for the binding of SDS molecules giving a lower number of negative charges per mass. However on full purification of the full length Na<sub>v</sub>Ms seen in the SDS-PAGE gel in figure 4b there appear to be further bands of a molecular weight larger than the tetramer. It is possible these are minor contaminants or higher order aggregates formed during the boiling step in SDS.

The cysteine mutation A221C was also introduced to the full length Na<sub>v</sub>Ms by PCR. This could be purified without thrombin cleavage, an example of which is shown in figure 4. The spikes in the elution of the Na<sub>v</sub>Ms full length from the nickel column (figure 4a) are caused by pausing the elution for half hour incubation times before resuming elution to minimise the total volume of the eluted protein sample. The majority of the full length Na<sub>v</sub>Ms elutes from the size exclusion column (figure 4b) at 9.5 ml shoulders at 8 and 11.5 ml, neither of these shoulders have corresponding bands on the SDS-PAGE gel indicating they are not protein contaminants. As this column was run under non-reducing conditions it is possible the 11.5ml shoulder represents the tetramer and the other two peaks cysteine crosslinking of channels. These volumes give masses of 330, 263 and 118 kDa which is plausible for crosslinking however the difficulties in estimating the size of the surrounding detergent mentioned above and the fact all three of these values are outside the range of the standards used should be noted. If cross-linking is occurring it would be undone during the labelling of the sample (see chapter 5).

Here 3 constructs of Na<sub>v</sub>Ms suitable for biophysical characterisation were purified. The specific sample conditions for the different downstream applications are discussed in the coming chapters.

a)



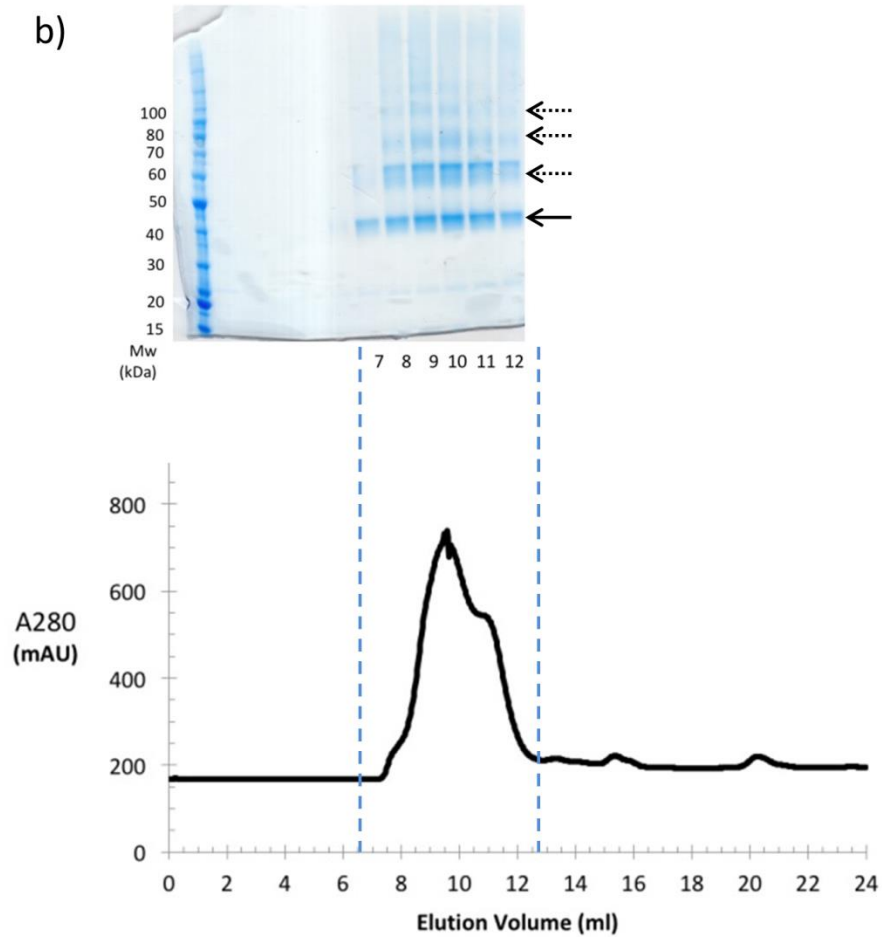


**Figure 4. The purification of the NaVMs full length A221C mutation.** Chromatograms (left) and reducing SDS PAGE gels (right) are shown for a) the initial elution from a Nickel column and b) the separation from an S200 size exclusion column. The UV absorbance at 280 nm and imidazole concentration are shown as solid and dashed lines respectively. Lanes in the SDS PAGE gels are marked with the elution volume of the sample from the corresponding chromatogram. The Na<sub>v</sub>Ms forms the distinctive ladder of bands at 40, 50, 80 and 100 kDa.

# Oriented circular dichroism spectroscopy of NavMs

---

## Introduction to circular dichroism spectroscopy

### Circular dichroism spectroscopy

Circular Dichroism (CD) spectroscopy is a well-established technique for studying the secondary structure of protein in a near-native environment at a physiological concentration range. This has many applications in observing the differences in secondary structure as proteins undergo state changes as facilitated by ligands or changes in buffer composition. The ability to monitor secondary structure directly in real time also facilitates the study of the stability of a protein by monitoring its' CD as a function of temperature (*Kelly et al., 2005; Wallace and Janes, 2009*).

A CD spectrum is measured as the differential absorption of left and right circularly polarized light across a range of wavelengths. This is in contrast to circular birefringence, which is the differential refraction of left and right circularly polarized light, as birefringence would also contribute to a CD measurement it is vital any cuvettes or cells used to mound samples do not have this property. For the study of protein secondary structure far-UV light in the region of 170-270 nm is used as this is where the absorption bands of peptide bonds fall. While near UV-region of 250-300 nm has a CD signal dependent on aromatic amino acids, the magnitudes are much smaller and the peaks broader than those from the backbone (*Kelly et al., 2005; Wallace and Janes, 2009*). The signal from an aromatic residue is also very dependent on local electric field causing a large degree of spectral overlap from multiple aromatic residues (*Craig et al., 1989*). This usually limits the study of this region is to a single aromatic residue at a time but can give insights into the tertiary fold of a protein unobtainable from lower wavelengths (*Woody and Woody, 2003; Boxer et al., 2004*). The CD of proteins is due to their chiral nature causing differential absorption of left and right circularly polarized light; in the case of aromatic residues this is the chirality local to the side chain, while the peptide bond CD is due to the chiral alignment of the backbone into secondary and tertiary structural elements (*Kelly et al., 2005*).

Practically a CD instrument is set up so that an intensive light source is reduced to a narrow range of wavelengths (the band width), linearly polarised before being circularly polarised by a piezo electric modulator, and passing through the sample chamber into the detector (*Sutherland, 2009*).

The detector consists of a photomultiplier tube which amplifies then detects the light signal giving a voltage that varies over time. This system is shown diagrammatically in figure 1. Experiments are set up so that this output voltage is always within a given range, the signal is boosted to this range regardless of the absorption of the sample by varying a high tension voltage (HT) applied to the photomultiplier. In a sample with a higher absorbance the incident light will be attenuated more and hence a higher HT will need to be applied to the photomultiplier (*Sutherland, 2009*). This means that during a CD experiment the HT can be recorded as a function of wavelength so that regions with a HT too high for accurate data can be identified. This HT cut off can be determined for a given instrument and is the voltage equivalent to an absorbance of 1.5 AU (*Miles and Wallace, 2016*).

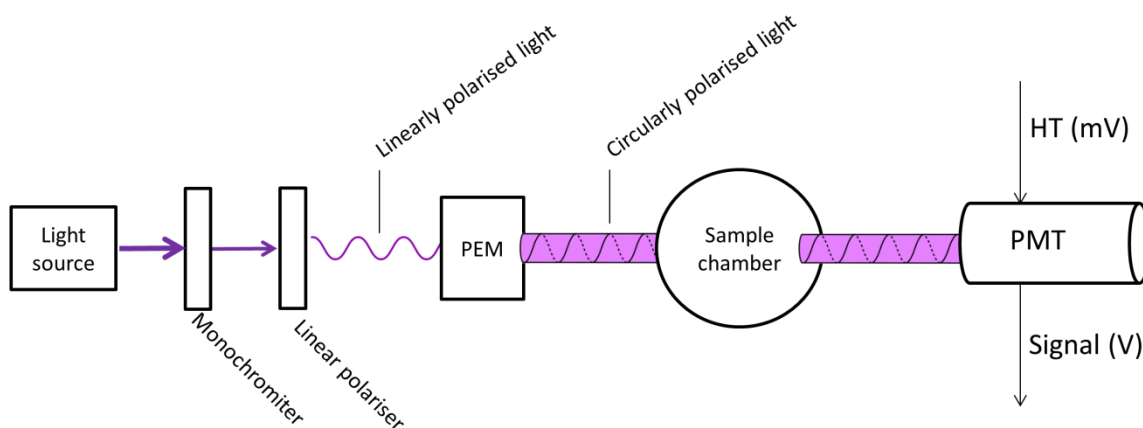


**Figure 1. Set up of a typical CD experiment.**

Protein secondary structures are defined by patterns of hydrogen bonding and specific ranges of  $\varphi$  and  $\psi$  torsion angles of the peptide bond (*Kabsch and Sander, 1983*). This restriction gives different secondary structures different chiral alignments of the peptide bonds and hence different characteristic CD spectra. The CD spectrum of a protein can be considered a linear combination of multiple component spectra created by the different secondary structures present within the protein (*Whitmore and Wallace, 2008*). Early methods for secondary structure determination by CD spectroscopy were focused around trying to calculate or observe ideal spectra for the different secondary structures (*Chang et al., 1978*). This approach is limited by the lack of proteins (natural or synthetic) covering each structural element that adopt a single stable secondary structure throughout.  $\beta$ -sheet proteins require turns between the strands by definition and other secondary structures, such as turns or the  $\pi$ -helix require a scaffold of other secondary structures for stability. Established methods for estimating the secondary structure of a protein make use of large reference datasets of CD spectra obtained from proteins with their structures available to atomic resolution by X-ray crystallography (*Whitmore and Wallace, 2008; Sreerama and Woody, 2000*). This has the advantage of being able to take into account any secondary structure found within the reference dataset and does not require any *ab initio* assumptions to be made about the spectral properties of the secondary structures (*Provencher and Glockner, 1981*). The most widely used algorithms estimate secondary structure by matching the experimental spectra to a linear combination of the reference set (*Provencher and Glockner, 1981*), use matrix methods to find singular value decomposition (SVD) solutions (*Sreerama and Woody, 1993; Compton and Johnson, 1986*) or, use neural networks trained on a reference dataset (*Andrade et al., 1983*). These methods have been further improved using variable selection, whereby solutions are found which satisfy multiple subsets of reference spectra and other restraints (*Manavalan and Johnson, 1987; van Stokkum et al., 1990*). The 3 most used algorithms (CONTINLL, CDSSTR and SELCON3) have been aggregated for use with a series of different reference datasets within the Dichroweb webserver (*Whitmore and Wallace, 2008*). A reference dataset of particular importance to this study is SMP180 as this is comprised of membrane proteins. Membrane proteins are composed of the same secondary structural motifs but there are different restrictions on the secondary structure of the transmembrane regions (*Abdul-Gader et al., 2011*). Transmembrane  $\alpha$ -helices are significantly longer at around 25-30 residues compared to the average of 10-12 in soluble proteins, this is due to the requirement of a length sufficient to span the lipid bilayer. The only stable transmembrane  $\beta$ -sheet is the  $\beta$ -barrel, which is composed of significantly more strands than the average  $\beta$ -sheet in solution and has a greater degree of curvature (*Miles and Wallace, 2016*). The CD spectra of membrane proteins have also been shown to differ from those of soluble proteins by the wavelengths of the peak maxima (*Wallace et al., 2003*). This is due to the difference in dielectric constant of a lipid

environment such as the interior of a micelle or the bilayer of a liposome compared to that of water (Wallace et al., 2003; Abdul-Gader et al., 2011). This effects the different peaks within a CD signal by varying ammounts (Chen and Wallace 1997) so a membrane protein spectra cannot simply be wavelength shifted to suit a reference set of spectra from soluble proteins. The solvent dielectric is able to shift CD peaks as the polarizability of the chromophore's local environment will alter the stability of its' ground an excited states differently and hence the energy required (and wavelength of photon) to promote an electron to the excited state (Wallace et al., 2003). This affects the transitions that give rise to a CD spectrum differently and hence the change relative peak positions. This will also affect the same transitions but in different parts of the protein differently as they may be buried in the low dielectric of a micelle or exposed to the high dielectric of an aqueous environment, hence the importance of the different structural motifs (e.g. transmembrane  $\alpha$ -helices and  $\beta$ -barrels) being well represented within a reference dataset (Wallace et al., 2003; Miles and Wallace, 2016).

### **Oriented circular dichroism (oCD)**

The estimations of protein secondary structure described above all require the protein be dispersed isotropically in solution in order that the spectra are representative of the proteins' conformation. This is because the absorption from chromophores within the protein have a directional dependence, hence for a protein oriented relative to the incident beam the CD spectra will be dependent on the orientation of the secondary structure elements within the protein. So given a protein of known secondary structure its' oCD spectra will be able to give information on its' orientation relative to the beam. Any changes in relative orientation of the secondary structural elements in response to experimental conditions can then be monitored. The electronic transitions of the peptide that give rise to CD within the 170-260 nm region are from non-bonding orbitals to excited  $\pi$  orbitals, namely the  $\pi_{nb} \rightarrow \pi^*$  and  $n \rightarrow \pi^*$  transitions as shown in figure 2 (Wallace and Janes, 2009). Within the context of an  $\alpha$ -helix the  $\pi_{nb} \rightarrow \pi^*$  undergoes excitation splitting into three transitions, this is due to the interaction of the electric field along the axis of the helix with the excited state (Moffit et al., 1957). One of the tansitions' dipole moments is polarized parallel with respect to the helical axis and the other two perpendicular, the first gives rise to a negative CD band at  $\sim 208$  nm and the others a positive band at  $\sim 190$  nm respectively. The  $n \rightarrow \pi^*$  transition gives rise to a further negative band at  $\sim 220$  nm which has a dipole moment oriented around the helical axis (Moffit et al., 1957; Bürck et al., 2016).

The amplitudes of the bands created by  $\pi_{nb} \rightarrow \pi^*$  moment are strongly dependent on their orientation relative to the propagation polarized beam. With a helix parallel to the beam the 190 transitions are additive giving a strong positive peak at  $\sim 195$  nm, while when perpendicular the

transitions are degenerate shifting the peak to  $\sim 190$  nm and lowering its' amplitude (*Wu et al., 1990; DeJongh et al., 1994*). In contrast the peak at 208 becomes less intense as the direction of the beam moves from parallel to perpendicular to the beam (*Wu et al., 1990; DeJongh et al., 1994*). If we assume the beam is oriented at a normal to a membrane this information alone would give a fingerprint spectra for an  $\alpha$ -helical peptide aligned to the surface or penetrates transmembrane. Moffit theory states that the CD of a material at a given angle ( $\theta$ ) can be calculated with the equation:  $CD_{\theta} = CD_{\parallel} \cos^2\theta + CD_{\perp} \sin^2\theta$  where  $CD_{\parallel}$  and  $CD_{\perp}$  represent the CD spectra of the material at  $\theta = 0^{\circ}$  and  $\theta = 90^{\circ}$  respectively (*Moffit et al., 1957*). Hence from a pair of reference spectra of helices oriented parallel and perpendicular to a membrane the spectra of any angle of insertion can be predicted (*Wu et al., 1990; DeJongh et al., 1994*). It is important to note as a CD spectrum is a linear combination of the spectra of the structural elements found within, it is impossible to distinguish a sample of tilted peptide (one oriented neither parallel or perpendicular to the beam) from one containing populations of peptides oriented parallel and perpendicular to the beam. (*DeJongh et al., 1994; Bürck et al., 2016*). It also follows that the spectra of an oriented  $\alpha$ -helical membrane protein will be formed of a linear combination of peptides at the angles of each individual  $\alpha$ -helix.

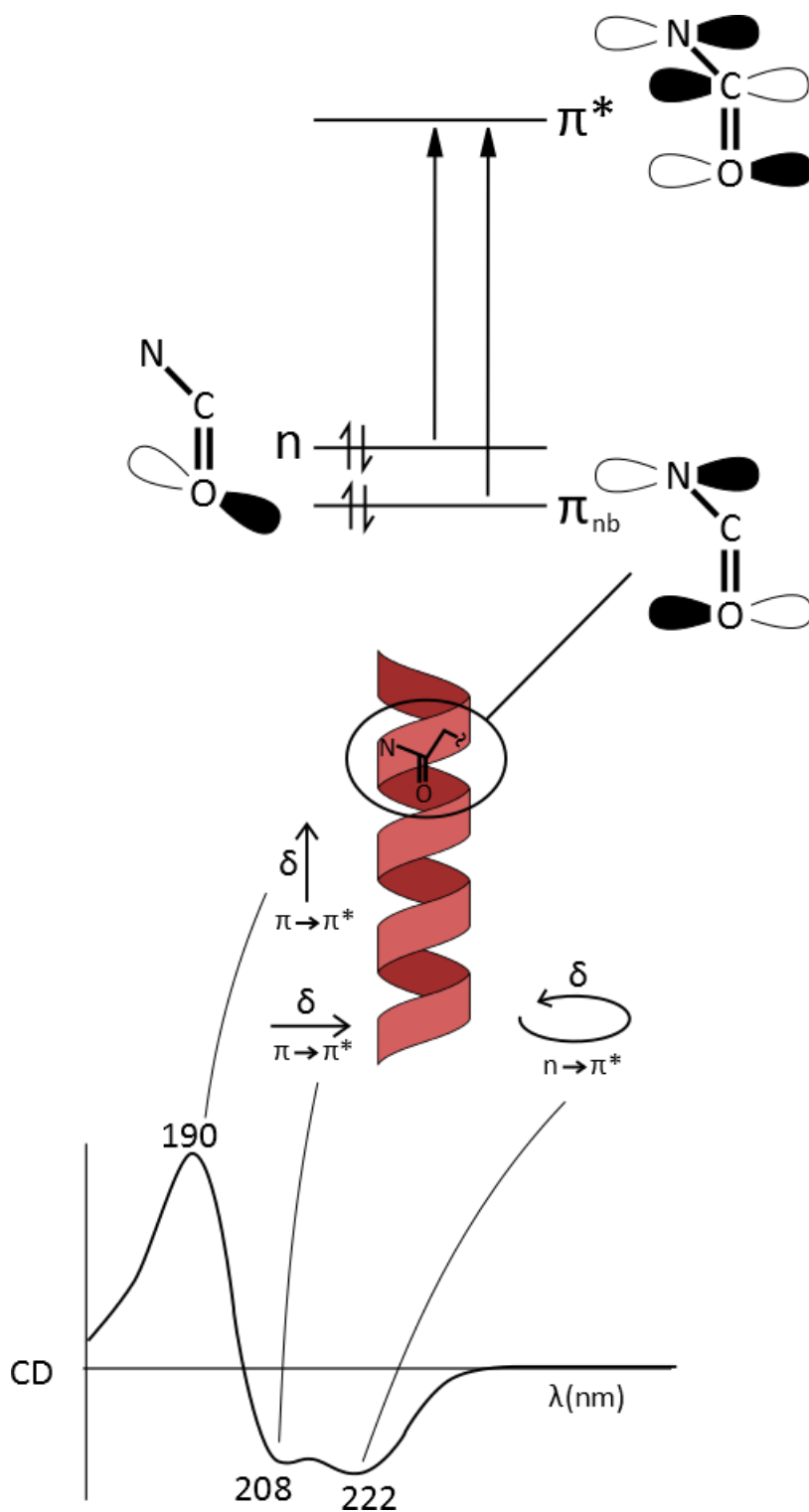


**Figure 2. The electronic transitions that give rise to circular dichroism.** An energy level diagram is shown (above) showing the orbitals of electronic transitions which give rise to UV-CD in an amide bond are shown. The directions of the electronic moments of these transitions is shown for an  $\alpha$ -helix (middle) and the CD peaks that these give rise to (bottom).

## Possible sources of error in oriented circular dichroism

Practically the largest source for error in an oCD experiment will be the ability to produce homogeneous well oriented protein lipid films. When measuring an oCD spectrum in a spectrometer the obtained data will also have contributions from linear dichroism (LD) and linear birefringence (LB) (*Wu et al., 1990*). LD is the difference in absorption of two planes of polarization of light at right angles to each other. The LD of a sample is maximal at an angular frequency of polarization twice where CD is maximal so most of the LD contribution is eliminated by instrumentation optimized for CD measurements (*Sutherland, 2009*). It should still be noted that anisotropy of a sample in the plane normal to the beam can still give rise to LD artefacts within an oCD spectrum (*Bürck et al., 2016*). It has been shown that the magnitude of this distortion is limited in thin uniform samples where the planes of the bilayers are as close to normal to the beam as possible (*Wu et al., 1990; Bürck et al., 2016 supplementary*). It has also been shown that the magnitude of this distortion is equal and opposite when the sample is rotated by 180° about the axis of the beam propagation (arrow in figure 2); hence it is best practice to take spectra at many rotations about this axis for averaging (*Wu et al., 1990; Bürck et al., 2016 supplementary*). LB is the property of a material having a different refractive index for beams of light of different polarizations and has been shown in some ordered lipid systems (*Wu et al., 1990*). The LB of a sample is directly proportional to its thickness and angle between the incident light and refracting interfaces; so like the LD effect LB is minimized in thin samples with the interfaces (bilayer planes) oriented normal to the beam (*Wu et al., 1990*). The orientation of lipid bilayers to an incident beam is also dependent on the phase of the lipid system, hence it is important to choose a lipid mixture that will be in a lamella phase at the temperature and humidity the experiment is being conducted at. This also shows the necessity to tightly control the humidity of the system to keep the phase of the lipids constant (*Bürck et al., 2016 supplementary*). Figure 2 shows the general set up of an experiment optimized for oCD as first devised by Chen (*Chen et al., 2002*) and refined by Bürck (*Bürck et al., 2016*).

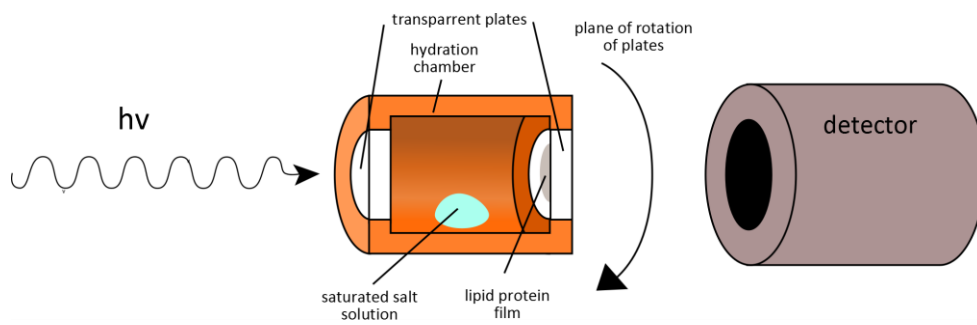


**Figure 3. A typical experimental set up for oCD data collection**

## The study of membrane proteins by circular dichroism

Circular Dichroism has already shown its' utility in the study of membrane proteins including ion channels. In assaying a membrane protein's stability CD offers advantages over other standard methods. Fluorescent approaches are either based on the change in fluorescence of a probe molecule as it binds to the unfolding protein or change in intrinsic fluorescence of tryptophan residues. In the case of the thermofluor assay this is the increase in fluorescence of the dye as it associates to the exposed hydrophobic core of a protein (*Reinhard et al., 2013*). This has two problems when applied to membrane proteins: first membrane proteins have external hydrophobic regions and second the hydrophobic nature of the detergents used to solubilise membrane proteins will create a very high baseline fluorescence for the assay. Another type of dye used is the thiol specific CPM which increases in fluorescence once reacted with an exposed cysteine residue, hence it is based on the increasing accessibility of internal cysteine residues as a protein unfolds (*Alexandrov et al., 2008*). This method along with intrinsic tryptophan fluorescence is limited by requiring specific residues within the protein and hence only measuring the unfolding of regions of the protein with that residue (*Zheng and Brennan, 1998*). For example the only cysteine residue within Na<sub>v</sub>Ms is in the voltage sensor so any CPM assay would be insensitive to the unfolding of the pore domain. In contrast CD is dependent on the entire sequence of the protein. Prior to the use of SRCD it was unclear whether the difference in stability of the NaK-ATPase found in pig and shark was due to the protein sequence or the differences in bulk lipid in the membrane's they are present in. SRCD thermal denaturation experiments on reconstituted NaK-ATPase showed the higher stability of the pig enzyme was down to the protein sequence rather than lipid environment (*Miles et al., 2011*). In addition for proteins with multiple domains it is possible to determine if they unfold sequentially and cooperatively (*Miles and Wallace, 2016*).

The wide range of buffers and pHs available for CD also makes it excellent for trialling conditions to be used in further biophysical studies. For example various detergents and amphipol solutions have been tested for their ability to stabilise Na<sub>v</sub>Ms for use in structural studies (*Ireland et al., 2017*). Here the higher the T<sub>m</sub> of Na<sub>v</sub>Ms in a given solubilising environment the more stable it is. This increased stability means it is less likely to precipitate out of solution rather than crystallise and so aids structure determination by X-ray diffraction. The more stable a protein is the more likely it is to be homogeneously distributed in solution and not undergo aggregation. This makes making particle picking easier within Cryo-EM structure determination as grids frozen will have particles spread more evenly with less aggregates to avoid.

In addition to trialling solubilisation conditions for membrane proteins CD thermal melts are also able to study ligand binding. This is because a bound ligand is likely to stabilise a protein, this has been extensively to study the drug binding of soluble proteins. However it must be noted that if a ligand will dissociate at a much lower temperature than the protein starts unfolding no effect will be seen. FsrC is a transmembrane histidine kinase involved in the quorum (bacterial density) sensing pathway of *Enterococcus faecalis*. Here SRCD shows no stabilisation of FsrC when its pheromone ligand is bound (*Patching et al., 2012*). However this study shows how the far UV region of a CD spectrum varies on ligand binding, if the binding event is specific to an aromatic residue. It is even easier to detect the binding of a ligand if it is correlated with a change in secondary structure, this was seen when CD was first used to detect ligand binding of a membrane protein with protein kinase C. Here ligands that promoted activity of the enzyme were seen to reduce the  $\alpha$ -helical and increase the  $\beta$ -sheet content of the protein (*Bosca and Moran, 1993*).

In addition to the order that secondary structures melt within proteins CD can also be used to assess the secondary structure of specific regions by obtaining the spectra of various truncations. The secondary structure of the CTD within NaChBac was first determined by CD spectroscopy of truncated mutants, revealing the last 22 residues to be helical with the next 16 (up until the end of S6) to be a disordered random coil (*Powl et al., 2010*). This first led to the model of a coiled coil connected to the base of the channel via a flexible linker.

While oriented circular dichroism is an emerging technique it has also already shown its utility in the study of membrane proteins. oCD's use thus far has largely been limited to peptides however it can still give valuable insights into membrane proteins (*Burck et al., 2016*). oCD was first used to study the insertion of amphipathic cytotoxic peptides into membranes. These peptides are  $\alpha$ -helical and their toxicity comes from their ability to spontaneously insert into the membrane and form channels lysing cells (*Huang et al. 1991*). For the peptides alamethicin, PGLa, MSI-103 and MAP were found to lie with their helical axis parallel to the membrane at low protein to lipid ratios and then switch to perpendicular at high ratios (*Huang et al. 1991; Burck et al., 2008*). This reveals the concentration dependant manner that these amphipathic helices are able to insert into the membrane.

A good example of studying a membrane protein rather than peptides by oCD is the twin arginine translocase component TatA (*Lange et al., 2008*). TatA forms the pore through which translocation occurs, oCD spectra of the N terminal helix show an orientation perpendicular to the membrane whereas the C terminal amphipathic helix lies parallel to the membrane. This shows that in the membrane the protein would adopt a right angle conformation with the C-terminal section

lying on the surface of the membrane and the N-terminal helix protruding into it. It's important to note that oCD spectra of the entire TatA protein are reminiscent of a single tilted  $\alpha$ -helix showing that the spectra from multiple helices in a linear combination of the spectra of the individual helices (Lange *et al.*, 2008). These results are in contrast to the receptor component of the translocase TatC which consists of 6  $\alpha$ -helices and gives a spectrum indicative of helices perpendicular to the membrane for the full length protein (Nolandt *et al.*, 2009).

## **oCD analysis of Na<sub>v</sub>Ms**

The rest of this chapter details the oCD experiments performed on Na<sub>v</sub>Ms in order to assay if the tilts of the pore helices of change on gating. This would be a distinct conformational change to the iris-like dilation proposed in Payandeh *et al.*, 2012. First it must be established if oriented films of Na<sub>v</sub>Ms can be formed. A 3:1 mix of POPE:POPG (1-palmitoyl-2-oleoyl-sn-glycero-3-phosphoethanolamine and 1-palmitoyl-2-oleoyl-sn-glycero-3-phosphoglycerol) was chosen for film formation as it showed the maximal activity and voltage dependence of the channel in D'Avanzo *et al.*, 2013. In order to assay structural changes in gating oCD was performed in the presence of various known bacterial sodium channel ligands. To maximize the change in oCD signal on gating a construct consisting of the pore domain (from S133 to H237) was selected as the voltage sensors and C-terminal domain are not predicted to significantly change tilt on gating (Sula *et al.*, 2016). These omitted regions would still contribute to oriented  $\alpha$ -helical CD spectra suppressing the magnitude of the spectral difference due to changes in pore helix tilt.

## **Methods**

### **Sample preparation**

The Na<sub>v</sub>Ms pore-only construct was purified as described in Chapter 3. After the size exclusion chromatography step the protein was concentrated to ~5 mg/ml in a 10 kDa molecular weight cut off spin concentrator (Millipore) before dilution to 2 times the desired concentration in 0.52% HEGA-10 200 mM NaCl / 20 mM Tris buffer.

Liposomes were a 3:1 mixture (determined gravimetrically) of POPE:POPG formed by pipetting 100  $\mu$ l of a 25 mg/ml lipid solution dissolved in chloroform into a glass vial, then evaporating the chloroform. The deposited lipids were resuspended in de-ionised water by sonication at 25°C (in a Grant XUBA bath sonicator). This gave a solution with a 50:1 lipid-to-protein molar ratio. Vesicles were formed by further rounds of sonication at 25°C until the solution was cloudy and homogeneous (~45 min).

Na<sub>v</sub>M pores were mixed 1:1 by volume with the liposome solution in a 20 µl dialysis button sealed with 10,000 kDa snakeskin dialysis membrane (ThermoFisher). These were dialysed in two stages against at least a 5,000 times excess of buffer (100 ml) in order to remove the HEGA-10 detergent. The first stage was against a 100 mM NaCl / 20 mM Tris base solution and the second stage was against a 10 mM NaCl / 10 mM Tris base in the final method used; all buffers were at pH 7.5. Different buffers trialled for the second stage of dialysis are specified in the relevant results section. The first dialysis step was overnight and the second for at least 3 hours all with mixing using a magnetic stirrer at 4°C.

Samples with bound ligand were formed by dissolving ligands in DMSO (dimethyl sulfoxide) to 100 mM, 2 µl of DMSO drug solution was added to 100 µl of the liposome solution to give a 10 times molar excess over the protein prior to dialysis. The apo protein samples for comparison with ligand bound spectra had the equivalent amount of pure DMSO added to the liposomes.

## **Film formation**

15 µl from each dialysis button were pipetted onto the centre of a 22mm suprasil quartz plate (Helma). These drops were spread using a pipette tip to make the sample as thin as possible with a diameter of ~12 mm. The films were dried under vacuum overnight (at least 12 hrs) at 22°C. The dehydrated films were subsequently re-hydrated in 64ml rehydration chambers sealed with parafilm in the presence of 1 ml of saturated K<sub>2</sub>SO<sub>4</sub> to give 98% humidity for at least 12 hours.

Na<sub>v</sub>M films in the presence of general anaesthetic were formed by incubation in a sealed 64 ml rehydration chamber with 1 ml of saturated K<sub>2</sub>SO<sub>4</sub> and 100 µl of isoflurane for 5 hours.

## **Data collection**

Initial spectra were collected on the AU-CD beamline of the ASTRID2 synchrotron, ISA, University of Aarhus, Denmark. The second veratridine comparison and isoflurane comparisons were collected on the UV-CD-12 beamline at the ANKA synchrotron, Karlsruhe Institute of Technology, Germany. Quartz plates containing hydrated films were placed in a demountable cell holder with the side containing the film facing the centre. 50 µl of saturated K<sub>2</sub>SO<sub>4</sub> is pipetted in the cell holder to maintain the hydration level before the other end is sealed with a clean quartz plate. For spectra in the presence of isoflurane, 20 µl of isoflurane was also included with the saturated K<sub>2</sub>SO<sub>4</sub> in the cell holder. Spectra were collected in continuous wave mode at a 1 nm interval with a 3 second averaging time and a 1 nm bandwidth from 280 to 180 nm at a temperature of 22°C. The oriented spectra presented are an average of 8 individual spectra taken of the same film at 45° increments around the beam axis. Films were rotated mechanically using the beamlines' own stages. For the initial ligand screen POPE POPG only films made under the same procedure as those containing

protein were used as a baseline. For the veratridine and isoflurane binding experiments baselines of POPE POPG films incubated with the relevant ligand by the same procedure as those containing protein were used.

## **Results**

### **Choice of support material**

Films were dried on both quartz and calcium fluoride ( $\text{CaF}_2$ ) plates to try and produce oriented samples. The surface tension of the sample on  $\text{CaF}_2$  caused it to form a raised droplet, which was resistant to spreading. Despite the use of a constant volume and extensive cleaning of the plates, the sample would not form a drop of consistent diameter making uniform films difficult to produce. In contrast the 15  $\mu\text{l}$  sample on quartz plates could be reproducibly spread to a diameter of 12 mm. For this reason all further experiments were conducted on quartz plates.

### **Buffer and concentration**

Due to the very low effective path length expected, an initial concentration of 3 mg/ml of protein prior to film drying was tried. This was more than sufficient giving a 228 nm peak of -70 millidegrees which is much more than required for assaying the difference in 210 and 228 nm peaks as shown in figure 4a. Lowering the concentration of the sample is desirable not only because it uses less material but would mean fewer stacked bilayers, as the lipid-to-protein ratio is kept constant. A lower number of stacked bilayers would mean there is less scope for distortion of the layers that are further from the quartz support. This would also mean a narrower width of sample limiting the effects of LD and LB.

In order to use a lower initial protein concentration of 1 mg/ml, NaF was trialed in place of NaCl in the dialysis buffer to limit the UV absorption from the chloride ions. A much lower concentration of NaCl at 10 mM was also tried to see if the protein was stable in a low salt environment during dialysis. The averaged spectra (from at rotations about the beam axis) for films dried from 100 mM NaCl, 100 mM NaF and 10 mM NaCl (all with protein at 1 mg/ml) are shown in Figure 4b. Also shown is the spectra normalised to their minima in order to account for any difference in amount of protein in the beam path between the films. The presence of NaF shifted the 228 peak to 233 nm and showed a suppressed 190 nm peak. Visually the NaF sample also looked less uniform than the NaCl appearing to contain crystals. The shift in the 228 peak could be due to the NaF crystals allowing a different level of rehydration to the NaCl containing films changing the dielectric around the protein. These crystals seem to be scattering the beam, shown by the increased HT values at long wavelengths where there should be little absorption of the beam by the

sample. The suppressed 190 nm peak is indicative of absorbance flattening. This would be caused by the protein being inhomogeneously distributed by the NaF crystals. This clustering of protein within the film will cause some light paths to contain very little protein, lowering the total absorbance and hence the absorbance difference that gives rise to CD.

Comparison of the spectra when normalised to their 228 nm minima showed that lowering the NaCl concentration does not significantly perturb the spectra so the protein is still stable. This is advantageous as while in solution 100 mM is a reasonable salt concentration, the effective concentration within a film will be very high due to the small volume left after dehydration. As the peaks were still of more than sufficient amplitude, it was decided the protein concentration could be lowered further. This is essential in order to maximise the amount of information obtainable from the spectra as with the conditions shown in figure 4 useable data is only available down to 204 and 190 nm for the 100 and 10 mM concentrations respectively. Lowering the concentration will lower the absorbance of the sample and hence the HT voltage required, while leaving large enough CD peaks to characterise the spectra. Final conditions of 0.5 mg/ml protein in 10 mM NaCl 10 mM Trizma base at pH 7.5 with a 50:1 lipid-to-protein molar ratio were chosen.

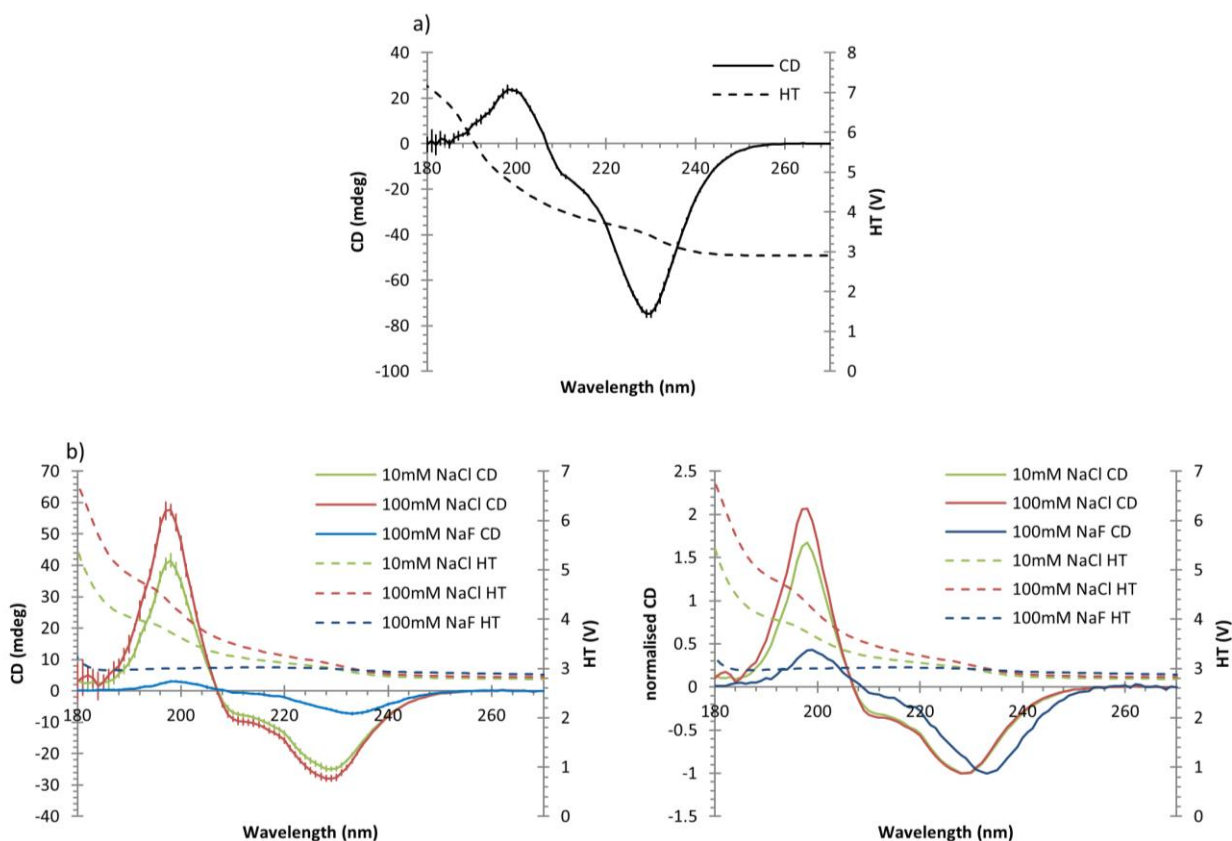


**Figure 4. The effect of buffer conditions on oCD spectra of  $Na_vMs$ .** CD spectra (solid lines) and HT curves (dashed lines) from films dried from different buffer conditions. The HT cut off for reliable data was 3.8 V in these experiments. a) protein was dried from 3 mg/ml in 100 mM NaCl 10 mM trizma base at pH 7.5. b) protein was dried from 1 mg/ml in 10 mM trizma base at pH 7.5 with different salt conditions indicated by colour. The spectra are shown in millidegrees (left) and with their minima scale to -1 for comparison. Spectra in millidegrees are shown with error bars of 2 standard errors.

## **Bilayer formation is non-denaturing**

While the 210 nm and 228 nm peaks are indicative of tilted  $\alpha$ -helices as would be expected of oriented  $\text{Na}_v\text{Ms}$  pores, this does not confirm that the process of bilayer formation retains the native fold of the protein. It is possible that the tertiary fold would be lost with the remaining  $\alpha$ -helical secondary structure lying at a tilted angle within the bilayers. To assay the effect bilayer formation has on the  $\text{Na}_v\text{Ms}$  pore, the hydrated protein–lipid film was solubilised with a 1% DDM solution after oCD spectra had been collected from it. The resolubilisation was performed by pipetting on 8  $\mu\text{l}$  of the DDM solution to cover the film then agitating the film by pipetting up and down until the film could no longer be seen taking care not to aspirate bubbles into the solution. The other half of a demountable CD cell was then placed over the quartz baseplate to form a cell of path length 50  $\mu\text{m}$ . Spectra from these solubilisations varied in amplitude presumably due to differences in proportions of protein solubilised however some overlaid well with spectra of the  $\text{Na}_v\text{Ms}$  pore in DDM that had not been subject to bilayer formation as shown in figure 5. Comparison of the resolubilised spectrum with the film spectrum (figure 5 left) shows peak shifts from an oriented alpha helix to isotropically distributed helices indicating the helices are stable outside of the bilayer environment and hence not an artefact of dehydration. Superposition of the resolubilised spectrum with that from a  $\text{Na}_v\text{Ms}$  sample in DDM micelles that had never undergone film formation (figure 5 right) shows good alignment of the spectra except for the 190 peak; which is suppressed in the resolubilised spectrum. While this suppression may be due to a change in secondary structure (loss of  $\alpha$ -helix), it would also occur if the resolubilisation was partially incomplete as if  $\text{Na}_v\text{Ms}$  channels remained associated they would be clustered within the solution causing absorbance flattening. This suggests that the protein has retained its' fold, as if it had denatured it is unlikely that upon resolubilisation the protein would return to its' native fold. However due to the miss-match in 190 nm peaks we cannot be certain the fold has not changed at all.

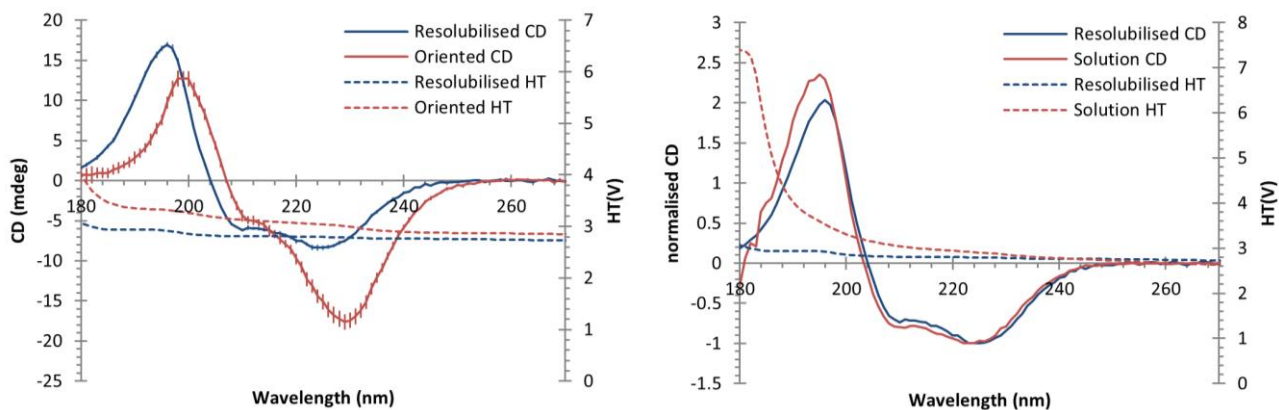


**Figure 5. The CD spectra of a resolubilised  $NaVMs$  film.** CD spectra (solid lines) and HT curves for the  $NaVMs$  pore resolubilised in 1%DDM overlaid with the oriented  $NaVMs$  pore film before resolubilisation (left) with error bars of 2 standard errors. The CD spectrum for the  $NaVMs$  pore resolubilised in 1%DDM overlaid of the  $NaVMs$  pore in solution purified in DDM (right) normalised to the 224 nm minima. For both spectra the HT cut-off is 3.8V

## **There is little effect from LD or LB and Films do not alter during data collection**

As described previously (*Bürck et al., 2016*) to minimise spectral distortions from LD and LB reported spectra are an average of 8 of the film around the beam axis. As the beams are rectangular (6 x 2 mm) this also has the effect of increasing the area of the sample data is recorded from. Figure 6a shows the spectra from each individual rotation of the oriented Na<sub>v</sub>Ms pore, these overlay very well indicating there is little distortion due to LD or LB. To further explore this spectra minima (at 228nm) are plotted against angle in figure 6b. Here repeats 180° apart should be sampling the same portion of the film so have the same spectra. The largest difference between these pairs is between -7.89 at 0° and -7.68 at 270°, so 0.2 or 2.5% of the signal which seems to be within the noise level of the individual spectra (as these are not averaged). The greatest difference between any rotation is between 0° and 90° and is 10% of the signal, this means the protein is distributed slightly unevenly across the sample as some regions of the film give rise to more CD than others. This effect is small enough it can be accounted for by averaging across all 8 rotations (*Burck et al., 2016*). While taking 8 spectra at different rotations helps to check for and reduce any artefacts it leads to a long time for data each sample to be recorded. Even at a synchrotron light source, data collection takes 5 minutes per spectra with time for the monochromator to reset and stage to rotate, this leads to at least 35 min between the first and last spectra collected. In order to check that the films do not significantly change hydration state or distort with rotation the initial rotational position had a second spectra recorded at the end of a rotational series. The CD spectra and HT are shown for the first and last spectra taken in a data set in figure 5b. These overlay nearly exactly showing there is very little if any change in the sample in the 45 min between the first and last spectra collected.

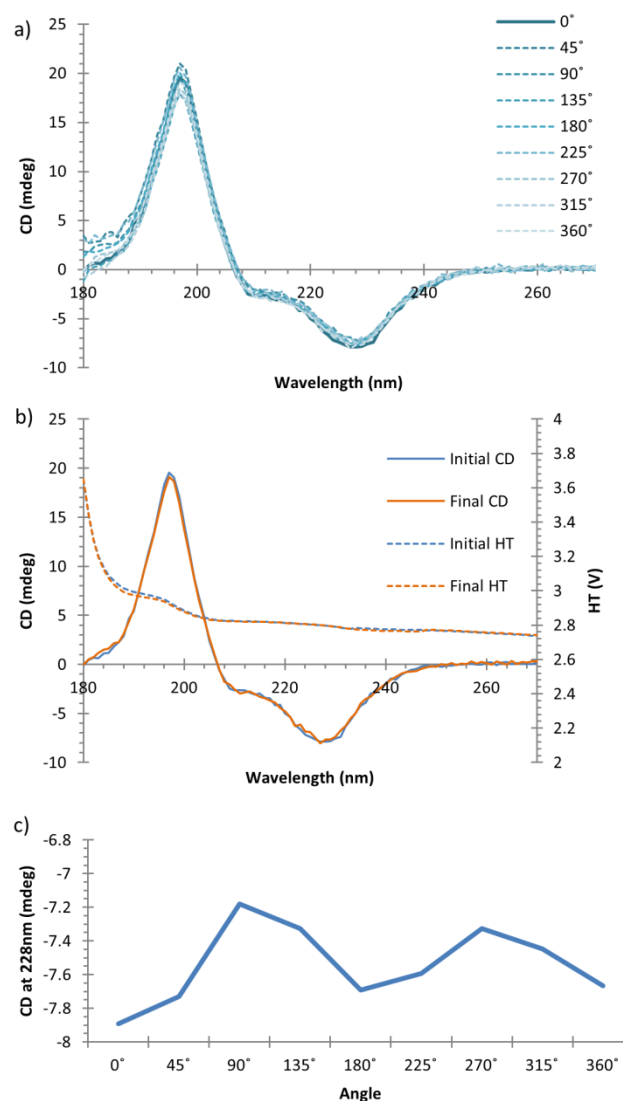


**Figure 6. CD spectra of oriented  $\text{Na}_v\text{Ms}$  films at different rotations around the beam axis.** Each angle recorded is shown in a. with the initial angle shown as a solid dark blue line and subsequent rotations as lighter blue dashed lines. Only the first angle and its' repeat at the end of data collection are shown in b) with their respective HT curves shown as dashed lines. A plot of CD at 228nm against angle is shown in c) for the data presented in a)

## **The process of bilayer formation orients Na<sub>v</sub>Ms**

In order to ascertain that the 228:210 nm peak ratio is indicative of Na<sub>v</sub>Ms orienting in bilayers, films of Na<sub>v</sub>Ms were formed from a detergent solution. This checks that the 'oriented' spectra are not only due to the orientation bias of the protein depositing on the surface. Spectra for Na<sub>v</sub>Ms dried from a Cymal-5 detergent solution are shown in figure 7 with an oriented spectra, and the resolubilised spectra from figure 5 for comparison. All 3 peaks from the protein-detergent film shift to the wavelengths of the solubilised spectra. The proportions of the negative peaks are also closer to those of the resolubilised protein. This indicates in the absence of phospholipid liposomes, films of Na<sub>v</sub>Ms are deposited anisotropically. Hence the process of proteoliposome dehydration creates a lipid phase with embedded oriented Na<sub>v</sub>Ms.

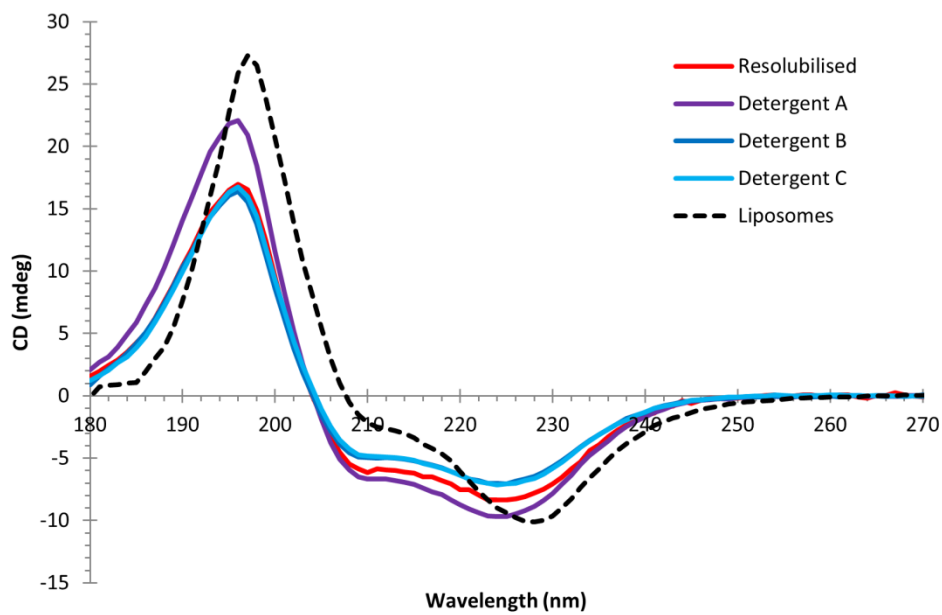


**Figure 7. CD spectra  $Na_vMs$  pore films dried from a Cymal-5 detergent solution.** The CD spectra from 3 films dried from Cymal-5 micelles in the same condition are shown (shades of blue) overlaid with the spectra dried from  $Na_vMs$  pore POPE/POPG proteoliposomes (black dashed line) and a solution CD spectra  $Na_vMs$  pore resolubilised in 1% DMM from POPE/POPG films (red line)

## Screening ligands for binding

To see if oSRCD is able to detect the binding of ligands to the Na<sub>v</sub>Ms pore a series of ligands were chosen that had either shown block by single channel electrophysiology (*Bagn ris et al., 2015, D. Clapham unpublished data*) or a reduction in radioactive Na<sup>+</sup> flux in a liposome assay (*Penny, 2017*). This flux assay tested various possible ligands' ability to inhibit the uptake of radioactive Na<sup>+</sup> by proteo liposomes containing Na<sub>v</sub>Ms channels. Uptake was measured by incubating the liposomes in a solution containing <sup>22</sup>Na<sup>+</sup> ions before washing the liposomes, spinning them down and measuring the radioactivity of the sample. The structures of these ligands are shown in Figure 8. A 10 times molar excess of each drug was included in the liposomes mixed with Na<sub>v</sub>Ms prior to dialysis and film formation. Spectra collected for Na<sub>v</sub>Ms in the presence of each ligand (blue) are shown with an average of 6 spectra of Na<sub>v</sub>Ms oriented in the apo form (black) in Figure 8 b-g. The apo spectra averaged are shown in Figure 7a. To quantify the differences between the spectra 228:210 nm peak ratios are plotted for the different ligands. These are not simply the CD values at 228 and 210 nm, Gaussian curve fitting was used to find their locations. The three peaks are fit simultaneously by nonlinear fitting from the curve fit function of the scipy python package with the only restriction that one Gaussian be positive and the other two negative. The parameters for the Gaussians fitted to all of the spectra are given in appendix 5.

These show that with exception of mibefradil the ligands shift the distribution of spectra to have a more intense 210 nm peak. This does not necessarily mean mibefradil would not affect Na<sub>v</sub>Ms in this context as compared to the other ligands it is much more water soluble. As the detergent is removed by lengthy dialysis steps it is possible any bound mibefradil would dissociate and be dialysed away. Of the rest of the ligands while their relative 210 nm peaks are intensified compared to the average of the apo. This increase in relative 210 nm peak correlates with α-helices shifting to a greater angle to the beam and membrane normal. While Benzocaine, Lidocaine, Tamoxifen and Veratridine all show a difference from the apoprotein at a confidence level under p=0.05 the variability between individual samples and low sample size mean these data are not conclusive.

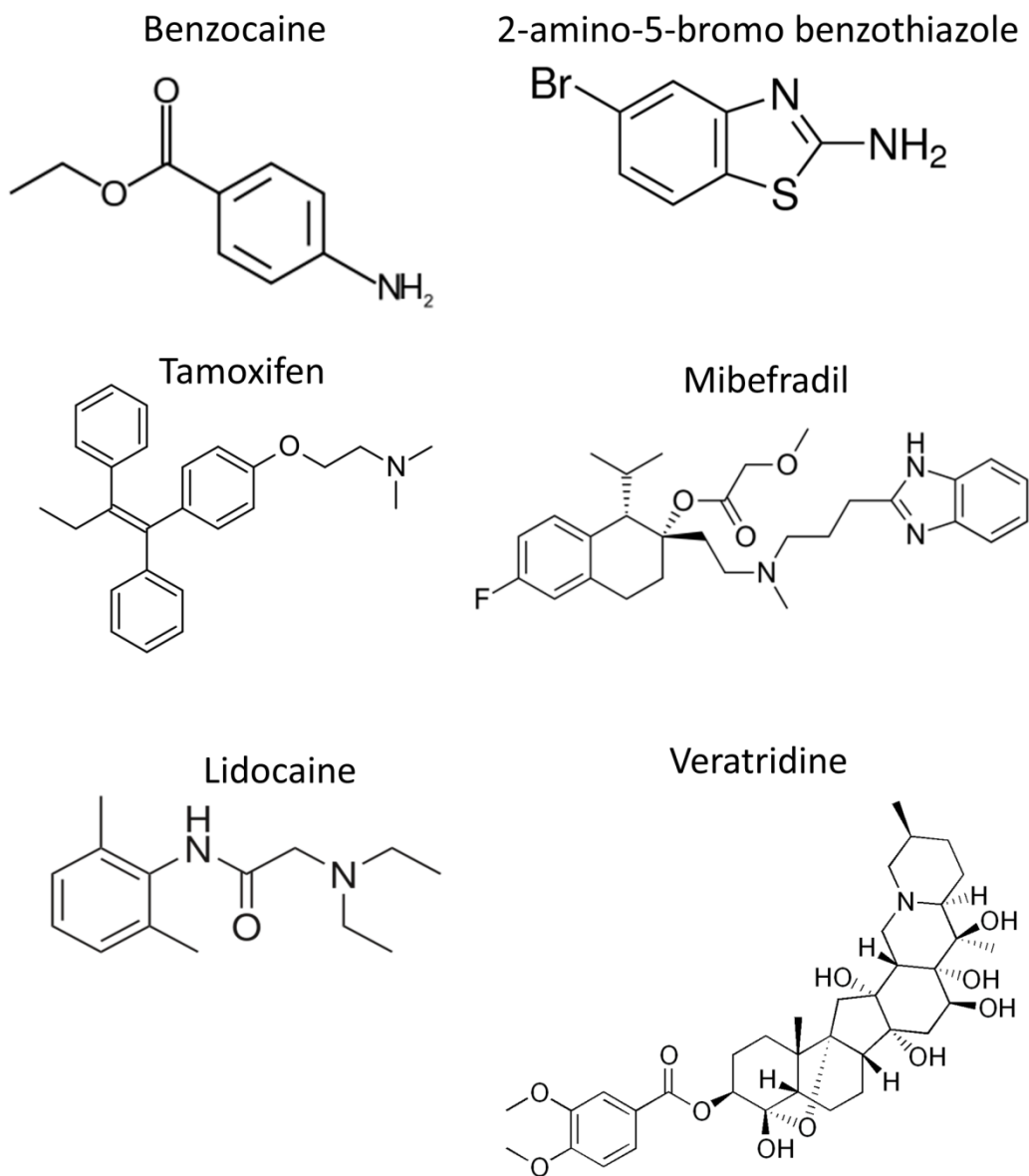


**Figure 8.** The structures of NaVMs ligands screened for binding in oCD

The magnitude of the 190 nm peak is inconsistent with the 228 nm peak between films. These data were collected over 3 data collection trips, in order to prevent degradation of the sample fresh Na<sub>v</sub>Ms was purified before each trip and liposomes prepared. It is possible that the differences in the films are due to variability in the purified protein despite their single band purity on an SDS-PAGE gel and the same buffer being used for size exclusion.

It is also possible that the change in spectra is caused by the drug acting on the lipid bilayer rather than binding specifically to the protein. This is because these spectra used spectra from films lacking the ligands as baselines, so it is possible the interaction of the ligands with the lipids has an optical effect.

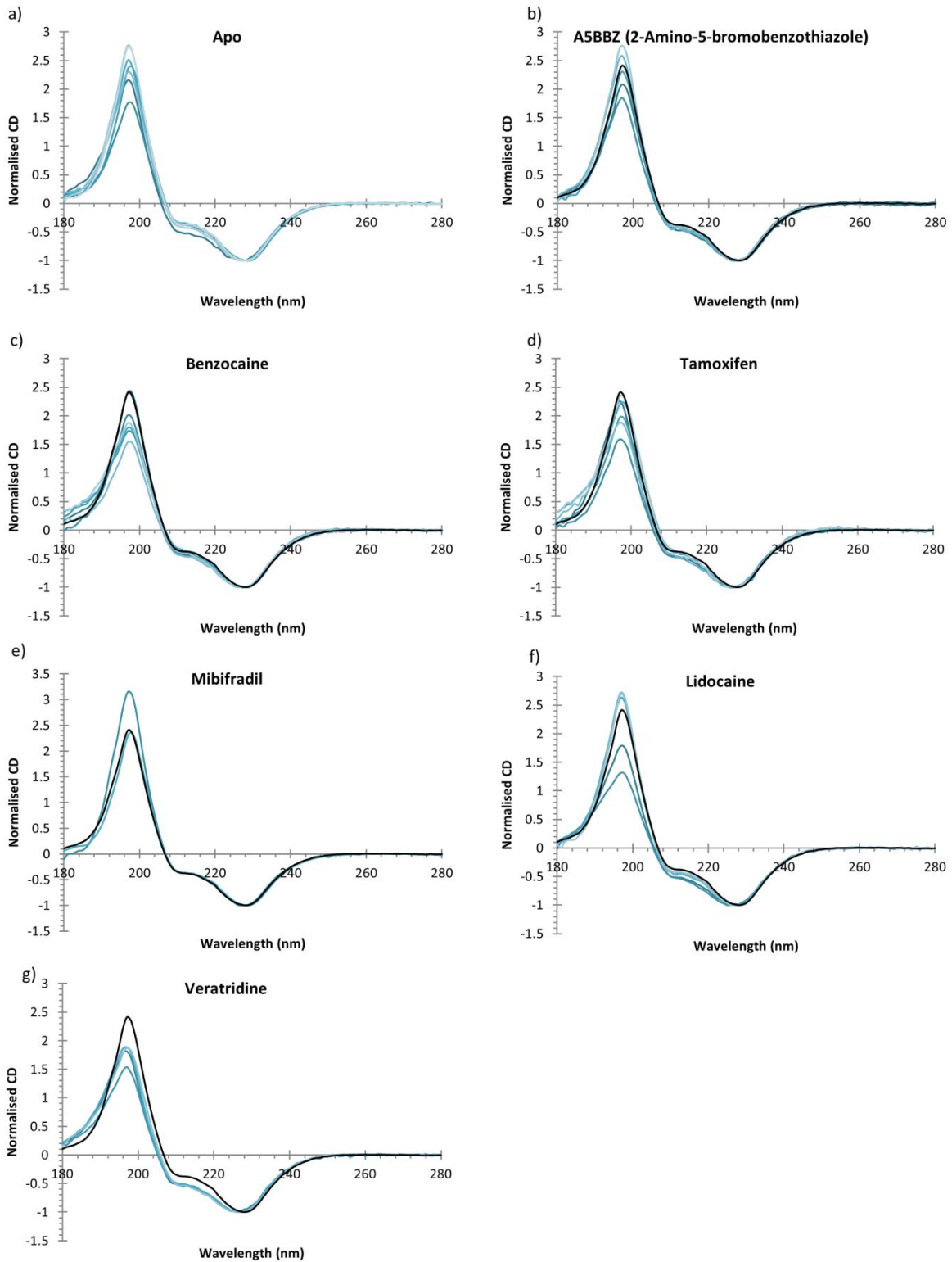


**Figure 9. oCD spectra of The Na<sub>v</sub>Ms pore bound to different ligands.** oCD spectra of the apo Na<sub>v</sub>Ms pore (a) with an outlying spectrum shown in red. oCD spectra of the Na<sub>v</sub>Ms pore in presence of the ligands indicated (b-g) blue lines overlaid with average oCD spectra of the apo Na<sub>v</sub>Ms pore (black lines).

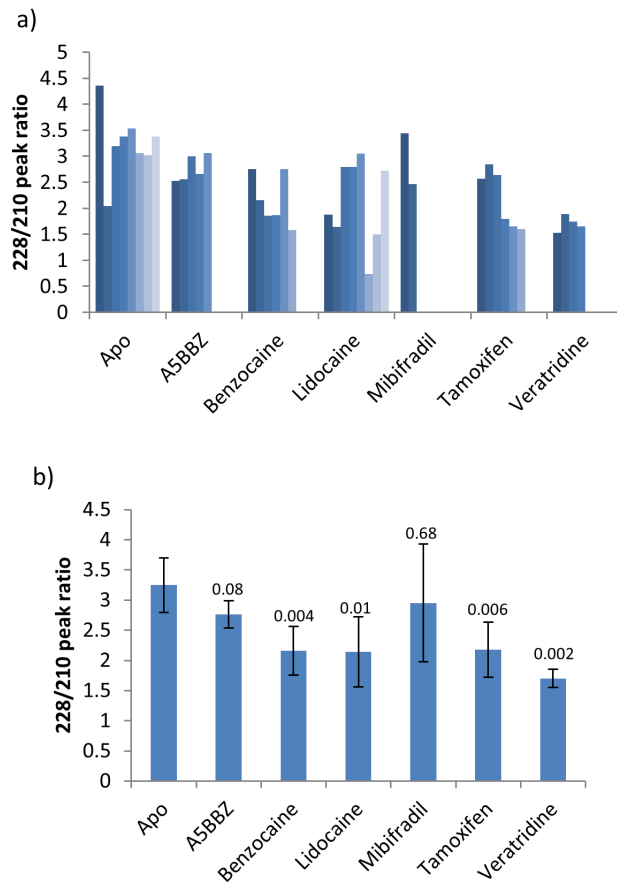


**Figure 10. 228/210 nm peak ratios for the oCD spectra of the Na<sub>v</sub>Ms pore in the presence of the ligands indicated. Values for each film recorded are shown in a) and averages with error bars of 2 standard errors in b), above each of the ligand ratio averages is the probability these values could be indistinct from the Apo as calculated by a 2 tailed independent t-test.**

## **Binding of veratridine to the NavMs pore**

As veratridine seemed to show the greatest change in 228/210 nm peak ratio, this interaction was selected for further repeats to be studied by oSRCD all in one data collection trip. In the ligand screening experiment it also showed the least difference in the shapes of the spectra collected so is most likely to give a significant difference from the apoprotein spectra. To confirm that veratridine does not interfere with the lipid bilayer baselines of films produced from liposomes mixed with veratridine by the same procedure as the protein samples were used. Figure 11 shows the spectra collected for NavMs films formed with and without veratridine. Unfortunately as was the case with the earlier apo spectra there was a variance in the 210 nm peak relative to the 228 nm, this time with two films showing an increased peak compared to the others. The spectra from the veratridine films shows there is also variation in these with the 3<sup>rd</sup> film showing a reduced relative 210 nm peak. The HT of the 3<sup>rd</sup> film shows an increase at 225 nm relative to the others, this increase in absorbance indicates a difference in the composition of the film such as contribution from denatured protein. There is no clear difference in the HT curves of the 2 apo spectra which show an increased 210 nm peak, so they may reflect a real distribution of oriented spectra from NavMs. 228/210 nm peak ratios are plotted as defined above in figure 12 with the average values and errors. The increase in 210 nm peak when bound to veratridine reflects an increase in average tilt angle of the  $\alpha$ -helices away from the membrane normal. Given there appear to be two different ratios observed for the apo protein one of which is similar to that observed for the veratridine bound, this could be interpreted as veratridine increasing the probability the channel is in one conformation. This seems unlikely given that oCD is an average technique so it would require all protein in the same film to be adopting the same of the two conformations.

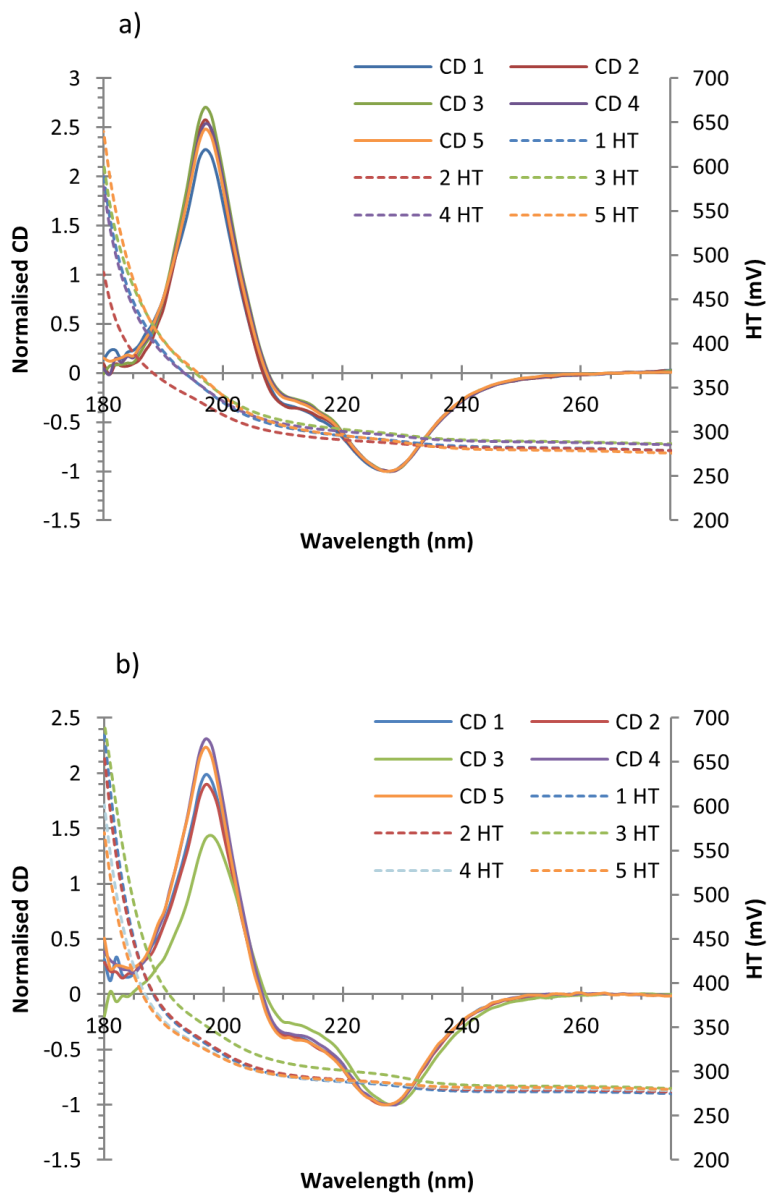


**Figure 11.** The effect of veratridine binding on the oCD spectra of Na<sub>v</sub>Ms. CD spectra (solid lines) and HT curves (dashed lines) shown for films of the Na<sub>v</sub>Ms pore alone (a) and in the presence of veratridine (b), all CD spectra are normalised to the 228 peak minima.

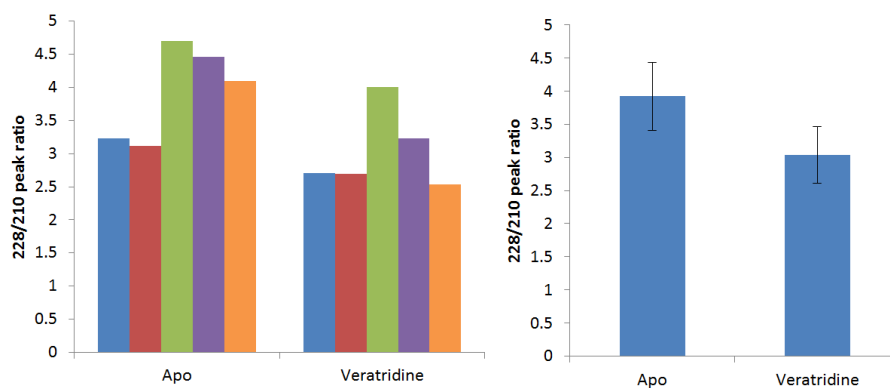


**Figure 12. 228/210 peak ratios shown for the oCD spectra of the  $\text{Na}_v\text{Ms}$  pore alone and in the presence of veratridine.** Values for each film recorded are shown in different colours (left). Average 228/210 ratios with error bars of 2 standard errors of the mean (right). The Veratridine data has a probability of 0.068 that its' 228/210 peak ratio is indistinct from the Apo

## **Binding of general anaesthetics to the Na<sub>v</sub>Ms pore**

The previous data shows that while oSRCD spectra are affected by the binding of ligands the differences between individual films complicates the analysis of this effect. oSRCD provides a unique opportunity to study the structural effects of general anaesthetic binding. As general anaesthetics bind from the gas phase it is possible to record data from a film before and after ligand binding in a non-disruptive manner. Figure 13 shows a pairwise comparison of oCD spectra from Na<sub>v</sub>Ms films before and after isoflurane incubation. Isoflurane was chosen as it is known to bind to the prokaryotic sodium channel NaChBac (*Ouyang et al., 2007*). The oriented Na<sub>v</sub>Ms films are the same as those shown in the veratridine comparison. As such they still show the same variation in initial spectra, however for the films with a lower 210 nm peak (films 3 to 5) showed an increase in this peak on the addition of isoflurane. Films 1 and 2 which already had higher 210 peaks than the others showed no significant increase on addition of isoflurane. This could indicate some difference during film formation had already caused the conformational change brought about by the binding of isoflurane. The increase in 210 peak from films incubated with isoflurane suggests isoflurane is increasing the tilt angle of the helices within Na<sub>v</sub>Ms to the membrane normal.

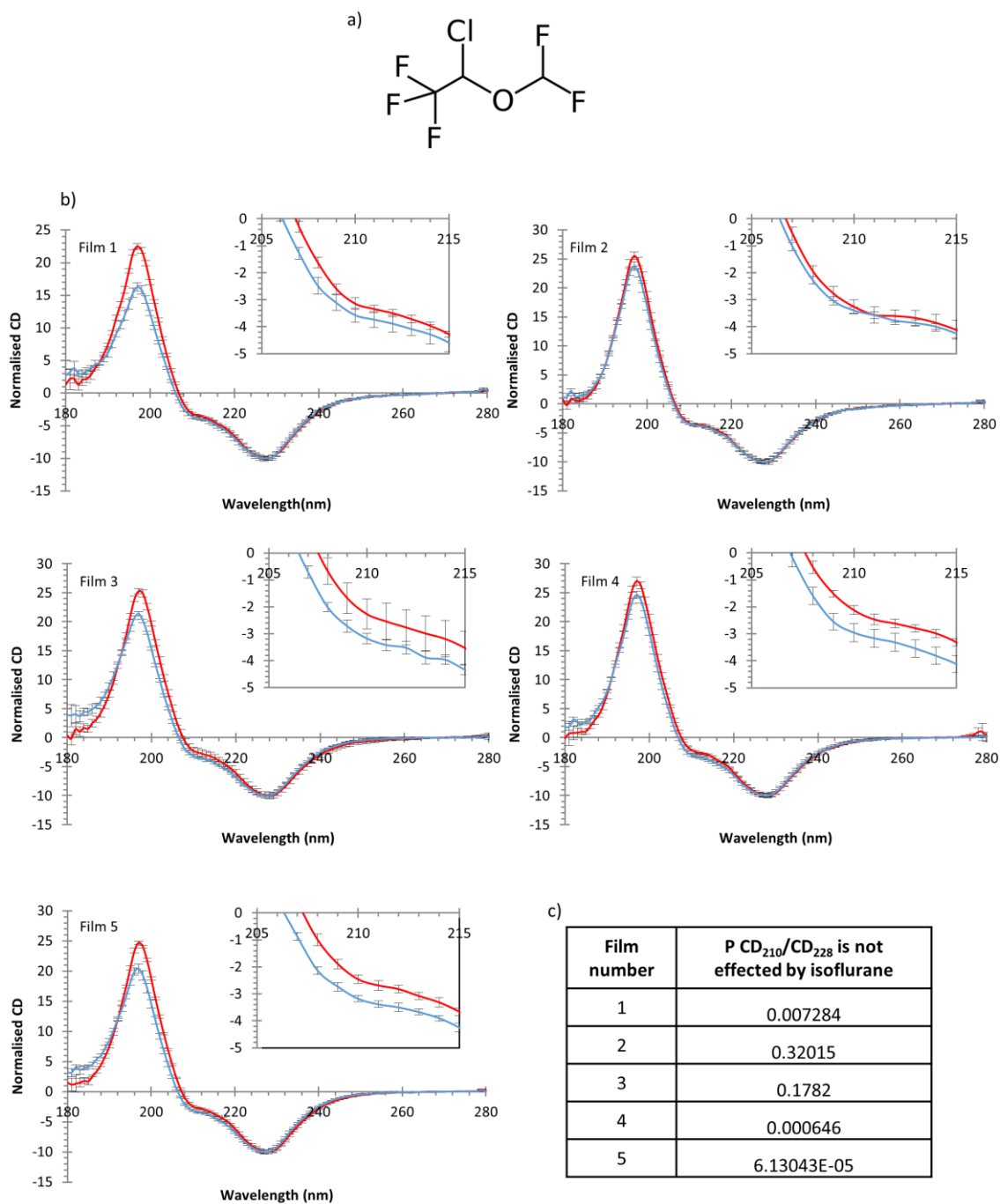


**Figure 13.** The effect of isoflurane incubation on oCD spectra of  $Na_VMs$ . The molecular structure of isoflurane is shown in a). oCD spectra of 5  $Na_VMs$  pore films before (red) and after (blue) equilibration in an atmosphere of isoflurane are shown in b), with error bars of 2 standard deviations of the individual rotational spectra are shown with the region between 205 and 215 nm expanded at the top right of each. c) shows the probability that the 210/228 peak ratio is unaffected by the addition of isoflurane as calculated by a 2-tailed T-test.

## Quantitative analysis of oSRCD data

Previous oSRCD experiments have been centred around classifying single  $\alpha$ -helical peptides as being transmembrane, surface associated or in a 'tilted state' (Bürck *et al.*, 2016). This is appropriate as for peptides consisting of a single  $\alpha$ -helix embedded in a membrane, as the lack of structural constraints mean they are likely to form a distributions of orientations. It should also be noted that a tilted state would be indistinguishable from a mixed population of transmembrane and surface associated peptides. Hence for single peptides 'angle' will refer to the average angle of the peptides, and is not meant to imply each are in the same orientation relative to the membrane normal.

Quantitative analysis of the angles of a  $\alpha$ -helical peptides would require reference spectra of the peptide parallel and perpendicular to the incident beam. Two attempts have been made so far at creating idealised spectra for oriented  $\alpha$ -helices; Wu *et al.*, 1990 used the solution spectra of poly( $\gamma$ -methyl L-glutamate) (PMLG) while deJongh *et al.*, 1994 used the alpha helical proteins from Chang *et al.*, 1978. Both methods are based around fitting four Gaussian curves and a Gaussian derivative to CD data to locate the positions of the absorption bands, and the helix band in the case of Gaussian derivative. The spectra for parallel and perpendicular are then created by summation of the curves assigned to the transitions of that orientation. The spectra with their contributing bands are shown in figure 14. The main difference apparent is that the Wu method predicts the spectra of a helix perpendicular to the beam will have 208 and 222 peaks of similar magnitude resembling an isotropic spectra. The expected CD from helices at angles other than 0 and 90° can be generated by using the equation from Moffit theory:

$$CD_{\theta} = CD_{\parallel} \cos^2 \theta + CD_{\perp} \sin^2 \theta$$

Where  $CD_{\theta}$  is the CD at a given angle  $\theta$  to the beam and,  $CD_{\parallel}$  and  $CD_{\perp}$  are the CD parallel and perpendicular to the beam respectively. Applying equation this to the two sets of oriented spectra gives the series of spectra shown in figure 14b.

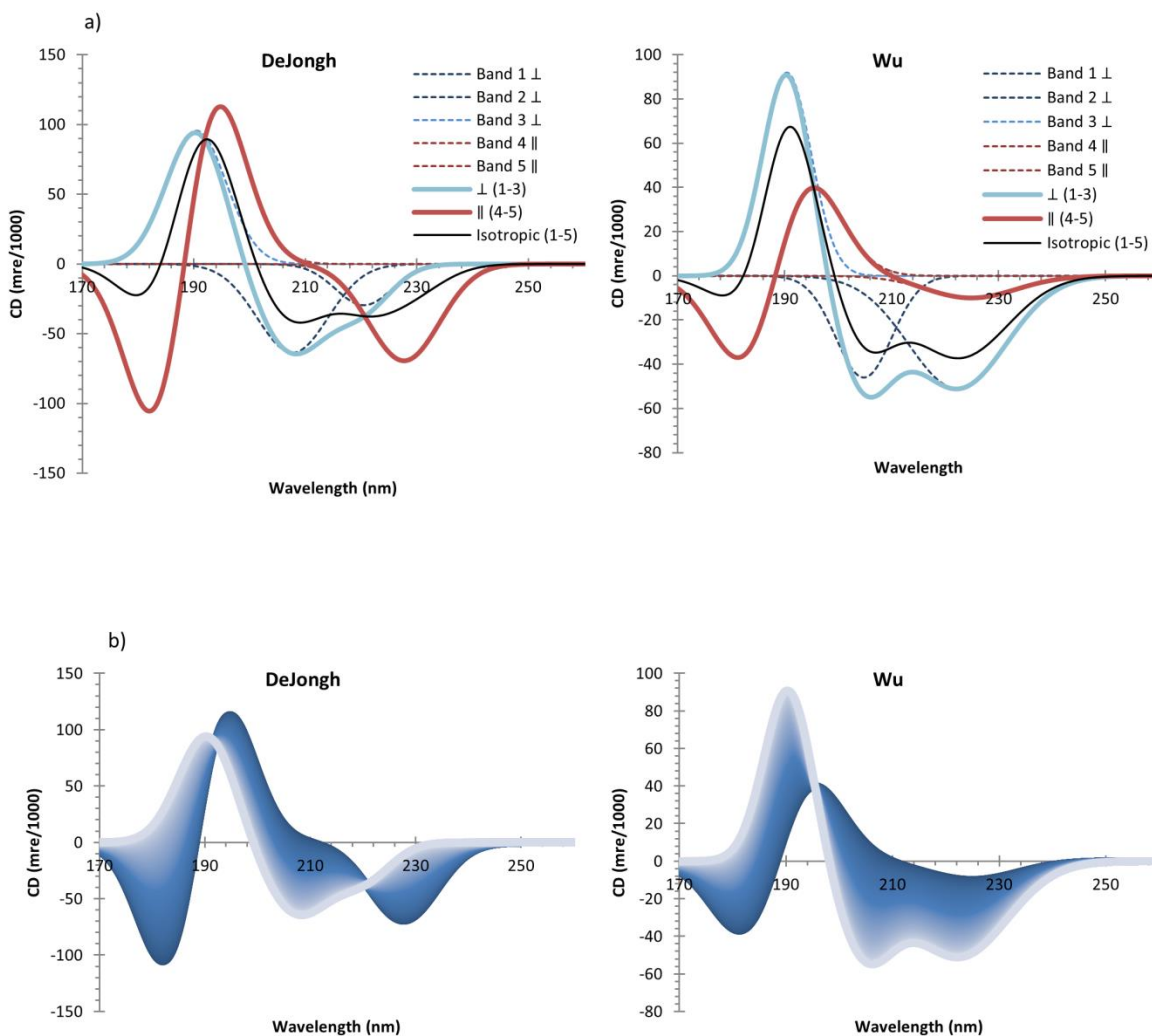


**Figure 14. Theoretical CD spectra for alpha helices parallel and perpendicular to the beam.** Spectra proposed in Wu et al., 1990 and DeJongh et al., 1994 are shown in a with the contributing peaks shown as dotted lines and an isotropic spectra as a black line. Spectra at different angles to the beam are shown in b going from parallel to the beam (dark blue) to perpendicular to the beam (light blue).

The two reference sets agree that the 208:222 nm ratio will decrease as the helix is closer in angle to the beam but differ in the magnitude of this effect and the shift in peak position of the 208 nm peak. The origin of this difference is in the relative contributions of the transition moments parallel and perpendicular to the helix within the 222 nm peak. This difference originates in the reference spectra used, each of which have their limitations. The PMLG spectra while verifiable as helical in solution is only based on a single spectrum so cannot reflect any of the variability in peak position and amplitude. This is especially true for differences due to helices in close proximity to each other as the helices in solution will be tumbling independently. DeJongh's reference spectra have the advantage they are based on multiple spectra of proteins with their secondary structure determined by crystallography, however as they are folded proteins the spectra will not be entirely helical. The data set used is also now rather outdated and limited only based on the  $\alpha$ -helical proteins from 15 known structures. Both methods are limited by the necessity that they be based entirely on soluble proteins. Since these papers were published it has come to light that there are significant spectral differences between the spectra of soluble and transmembrane  $\alpha$ -helices (*Chen and Wallace, 1997*).

While the contribution from LD and LB can be limited by the experimental set up and data collection there are further contributions of the oCD spectrum that need to be accounted for. The process of bilayer formation is unlikely to orient the entire sample as some tetramers may be left on the surface of the bilayer stacks out of the multilayer. This means the oCD spectra will have a contribution from an un-oriented protein population. This is the equivalent of the addition of the anisotropic spectrum proportional to the proportion of un-ordered protein, hence the equation for a partially oriented sample can be written as:

$$CD_{\theta} = (1 - u)(CD_{\parallel} \cos^2 \theta + CD_{\perp} \sin^2 \theta) + u CD_i$$

Where  $u$  is the proportion of unoriented protein and  $CD_i$  is the isotropic CD spectrum. Wu et al., 1990 proposed collecting spectra at different orientations of the membrane normal to the beam. This would change the angle between the membrane normal (and hence  $\theta$  in the above equation) while retaining the proportion of unoriented protein. However as the membranes and quartz supports have thickness this will also alter the effective path length and cause refraction of the beam. The above study fills a cylindrical sample chamber with water which will have a closer refractive index to the quartz to limit these effects. This would make measuring the angle of the membrane normal very difficult, a precise value of which is required for this approach to work. Further this would only ever work for oriented samples which can be produced sandwiched between

two plates and sealed to prevent disruption from the water. In recent years solid state NMR has been used as an independent method to assay the proportion of unoriented protein (*Bürck et al., 2016*). However this requires that protein be available isotopically labelled and in quantities required to give enough of a signal.

Ideally the protein could be switched between conformations of different tilt angles without changing the proportion of unoriented protein. This would require the uniform production of films with the same proportion of unoriented protein or the ability to switch the conformation of a film after data collection without disrupting it. General anaesthetic binding provides a good opportunity for this. However in the present data the variation of the 190 nm peak between films would dominate any comparison.

### **Oriented reference spectra for membrane proteins**

In order to try and find reference spectra more representative of alpha helical membrane proteins an approach using the SMP180 dataset was used (*Abdul-Gader et al., 2011*). This dataset consists of membrane proteins with structures solved by x-ray crystallography. Of these the 12 proteins with an alpha helical content above 51% were used. These proteins had 4 gaussian bands (one positive and 3 negative), and one Gaussian derivative fitted to them using nonlinear fitting from the curve fit function of the scipy python package. Initially the only restraint used was the Gaussian derivative be positive at long wavelengths as described in DeJongh et al., 1994. However this lead to Gaussian curves of very high amplitude acting degenerately to form the steep downwards slope of the 190 peak. The extra constraints that the positive peak has a maximum amplitude of the experimental spectrum maximum and the negative peaks have a maximum amplitude of the spectrum minimum were added. These constraints seemed reasonable as at both the isotropic spectrum maxima and minima there are transitions acting constructively so the peak from no individual transition should exceed these. To ensure two Gaussians were fitted to the 222 nm peak the constraint was also added that two of the negative Gaussians have maxima above a wavelength of 215 nm (the local maxima between the 208 and 222 nm peaks in SMP180). The parameters obtained from SMP180 were averaged and used to create the reference spectra shown in figure 15. This was done with the highest wavelength Gaussian and Gaussian derivative assigned to the parallel spectra, and the remaining two Gaussians assigned to the perpendicular spectra. As the parallel and perpendicular spectra combine to give the isotropic spectra according to the equation: (*Wu et al., 1990*)

$$CD_i = \frac{(CD_{\parallel} + 2CD_{\perp})}{3}$$

The parallel and perpendicular spectra derived from SMP180 were multiplied by 3 and  $3/2$  respectively to give their true proportions.

These reference spectra share features with both the previous methods. As with the DeJong method the 228 nm peak is predicted to not only decrease in amplitude with angle to the beam but shift down in wavelength. As with the Wu spectra the 190 nm peak is predicted to increase in amplitude with angle to the beam, although to a lesser extent. These differences show the difficulty in assigning the directional transitions which sum to the isotropic spectra. The variation of spectra with angle will be required to monitor how these transitions vary relative to each other.

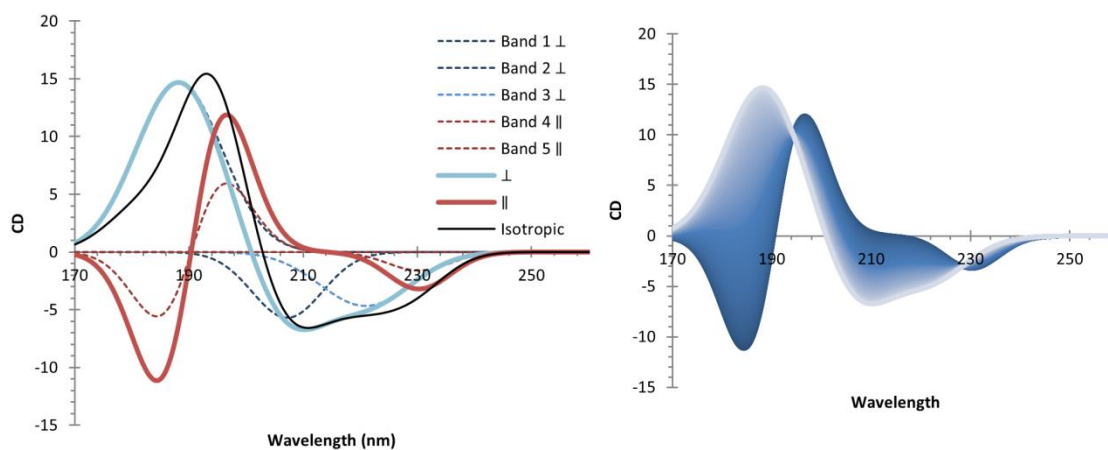


**Figure 15. Theoretical CD spectra for alpha helices parallel and perpendicular to the beam based on the SMP180 dataset (Abdul-Gader et al., 2011). Shown with the contributing peaks as dotted lines and an isotropic spectra as a black line (left). Spectra at different angles (right) to the beam are shown in  $b$  going from parallel to the beam (dark blue) to perpendicular to the beam (light blue).**

To assess the ability of the different reference spectra to describe the data collected they were fitted to the output of the Moffit theory equation with an additional scale factor S:

$$CD_{\theta} = S(CD_{\parallel} \cos^2 \theta + CD_{\perp} \sin^2 \theta)$$

This scale factor is to account for the fact the amount of protein the beam was passing through could not be measured and hence an effective concentration could not be determined. The fitting was performed by minimising the squared difference between the experimental and theoretical spectra using the differential evolution global optimisation function in the scipy package of python. As with all of the reference spectra the 190 nm peak maxima moves with angle and the experimental spectra the maxima is constant this was discounted. Fitting was only performed for negative CD values over 190 nm, this was because as the peak of greatest magnitude it would dominate the fit while the observed 190 nm peaks were very inconsistent.

The angles calculated from the 3 methods are plotted against the minimised square difference between the experimental and theoretical spectra in figure 16. The experimental spectra used were all of those from the ligand binding screen (those shown in figure 6). This shows that the SMP reference spectra give a similar angle range to the DeJongh spectra while the Wu spectra gave much larger angles. The Wu spectra also showed a poorer fits, the best and worst fits are shown in figure 14b. These show the Wu reference only fits well where there is little to no 210 nm peak. This is because in the Wu reference (figure 12b) at the angles where a 210 nm peak is present, the 228 nm peak is shifted to a lower wavelength than seen in the experimental spectra (around 222 nm). Conversely the SMP180 and DeJongh references fit spectra with little 210 nm peak the worst. The best fits and those of average performance are shown for DeJongh and SMP references in figure 17. These show that as well as fitting better on average the SMP180 reference more accurately represents the positions of the 210 and 228 nm peaks.

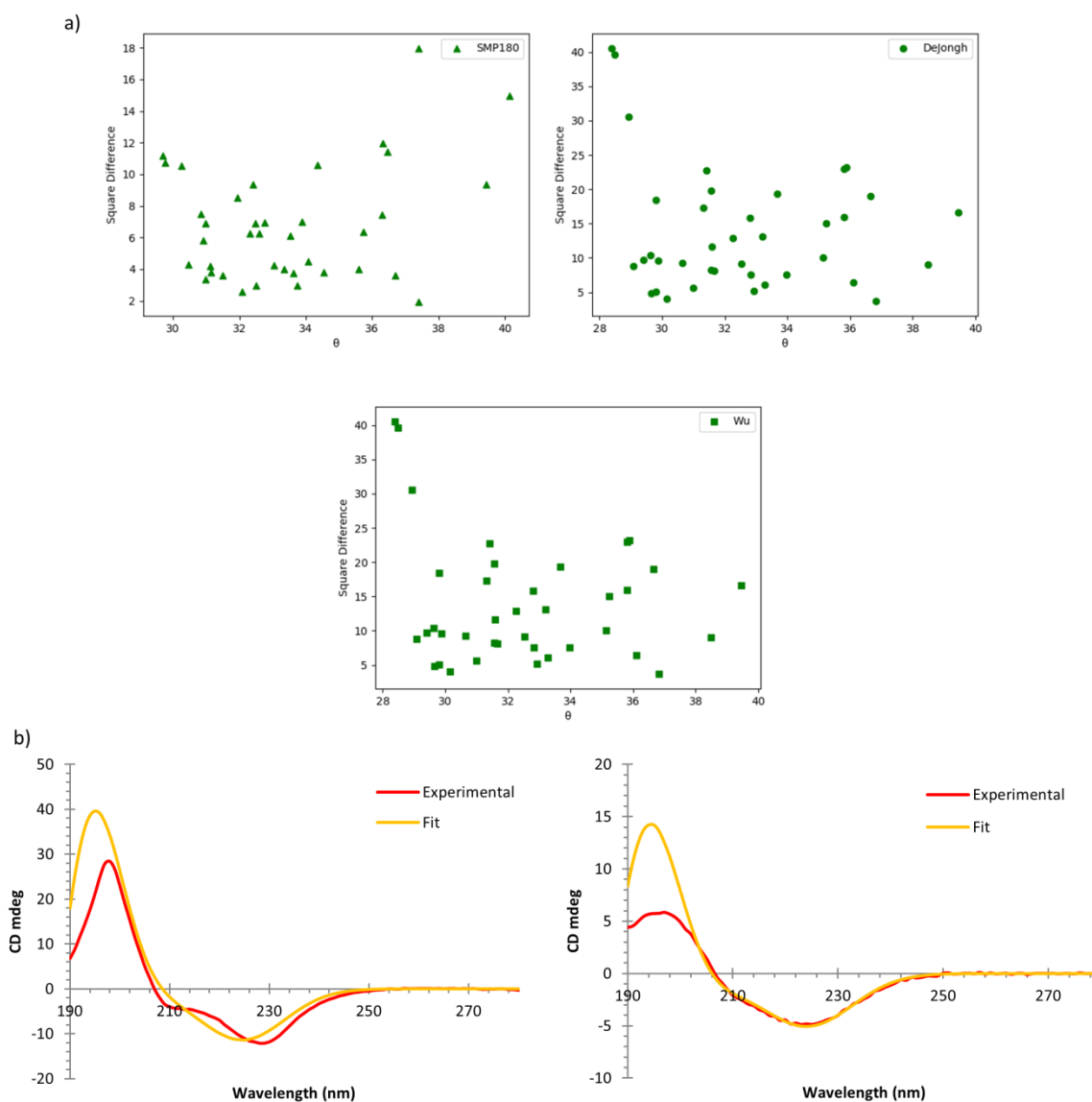


**Figure 16. The angle of theoretical spectra generated by different reference data which best fit experimental spectra. The angle of best fit is shown for the SMP180, Wu and DeJongh reference data is plotted against the square difference between the observed and fitted spectra (a). The best (left) and worst (right) fits achieved for the Wu data set.**

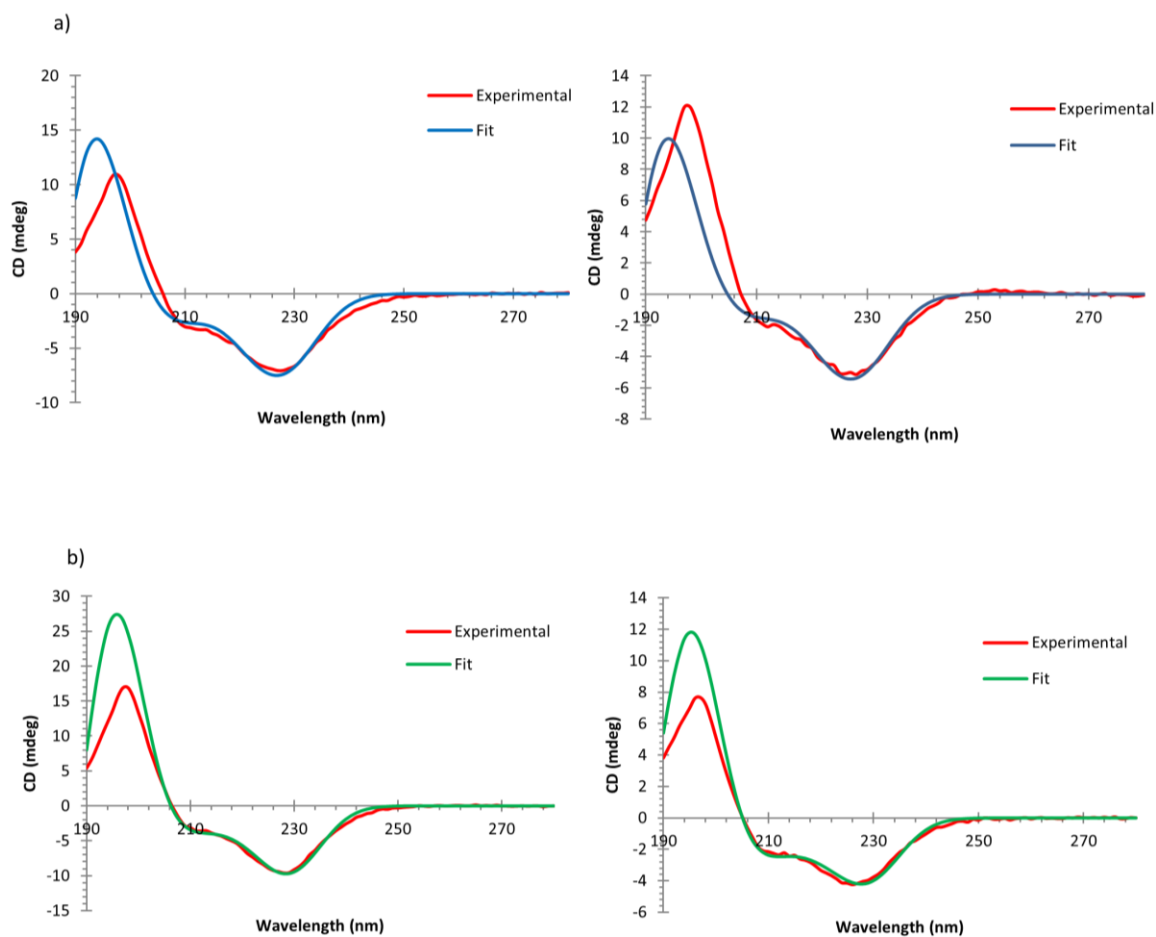


**Figure 17. Example fits of theoretical spectra generated from the DeJongh and SMP180 data sets to experimental. Average (left) and best (right) fits are shown for the DeJongh and SMP180 data sets (a and b respectively).**

Figure 18 shows the results of the fits from figure 16 for the SMP180 and DeJongh coloured by the different ligands present within the films. These showed some of the conditions causing spectra to cluster together with the apoprotein and mibifradil showing the greatest angle for each. As seen by looking at the peak ratios veratridine leads to a decrease in average angle, which here is quantified to  $\sim 6^\circ$ , and the smallest spread of angles between repeats.

To investigate if better fits could be achieved by including a proportion of isotropic spectra, the spectra of Na<sub>v</sub>Ms in cymal-5 solution (from figure 4) was included. Figure 19 shows the angle of best fit and the proportion of isotropic spectra that produced the best fit for the SMP and DeJong reference sets. Fitting was performed as above but with the extra parameter *u* for proportion of unordered protein according to the equation:

$$CD_\theta = S((1 - u)(CD_{\parallel} \cos^2\theta + CD_{\perp} \sin^2\theta) + u CD_i)$$

This shows that for the DeJong reference set the isotropic spectra dominate the fit while showing no difference in fit angle for most of the conditions except for veratridine. The SMP reference set shows a more modest proportion of isotropic spectra with the same trends for angles between conditions as without the isotropic spectra. The difference in angles is however narrowed with the apo and veratridine samples differing by  $4^\circ$ . The inclusion of the isotropic spectra has also significantly narrowed the spread of lidocaine angles indicating those spectra with poor fits to the SMP oriented spectra may have a higher proportion of unoriented protein.

For the isoflurane binding experiments pairwise analysis could be performed. Here the spectra were fitted to the SMP reference with an isotropic spectra as above but with the constraint that *u* be the same for each spectra in a pair. This approach is valid if the binding of isoflurane does not cause Na<sub>v</sub>Ms to become more or less ordered. As the pairs to spectra had different magnitudes they were normalised to their minima prior to analysis. Figure 20 shows the pairs spectra with their fitted curves. This shows a more modest change in angle of compared to the veratridine binding. Good fits could be achieved for the pairs of spectra indicating the assumption that the proportion of oriented protein stays constant during veratridine binding is valid.

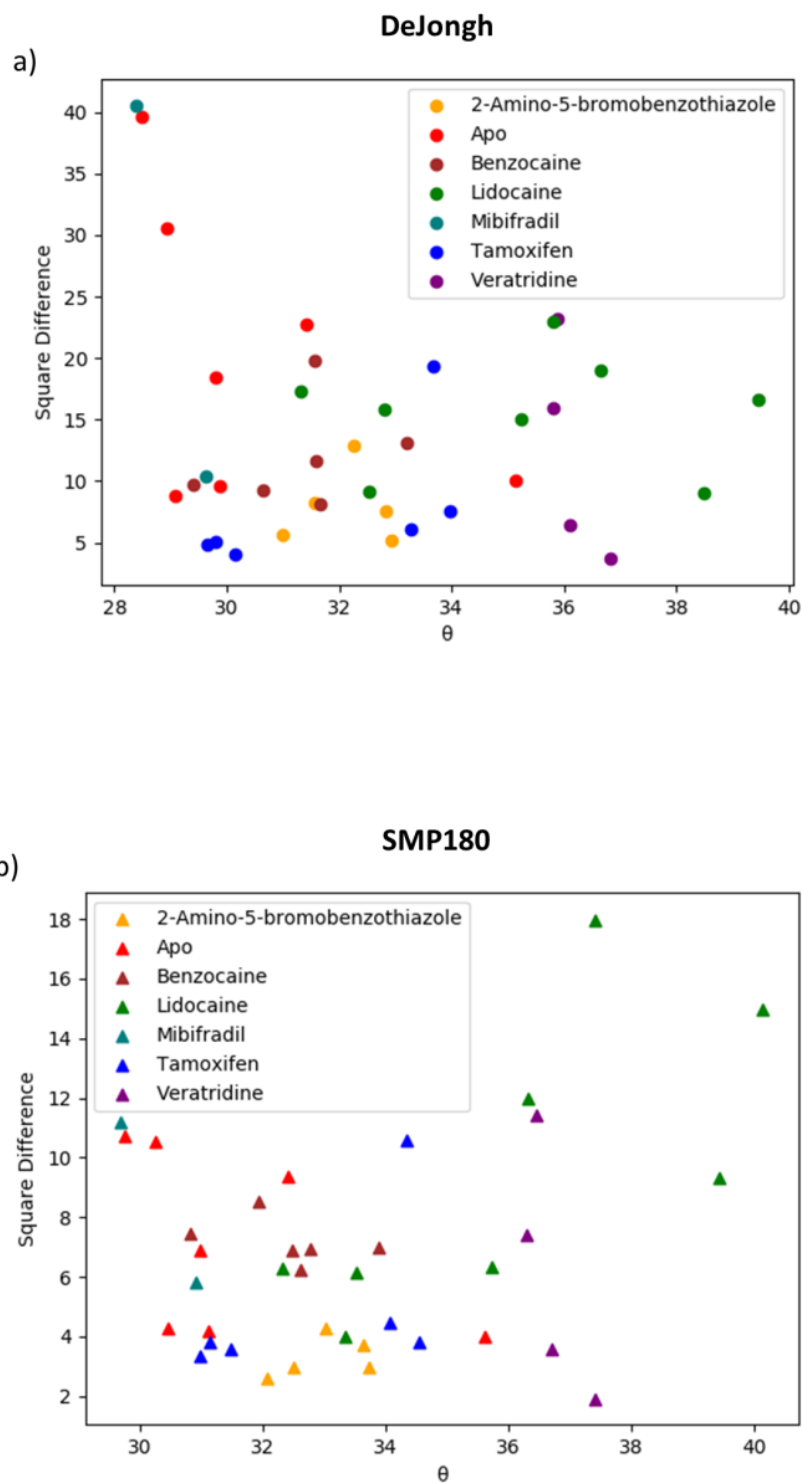


**Figure 18. The angle of theoretical spectra which best fit experimental spectra in the presence of different ligands. The angle of best fit is shown for the DeJongh (a) and SMP180 (b) reference data is plotted against the square difference between the observed and fitted spectra. Points are coloured by the ligand present in the film.**

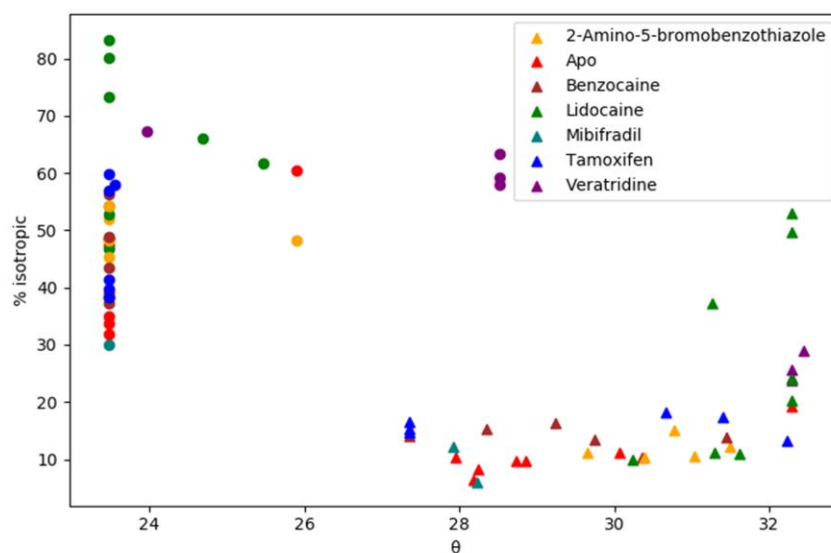


**Figure 19. The angle of theoretical spectra that best fits experimental data with an isotropic spectrum included.** The angle for SMP180 (triangles) and DeJongh (circles) are plotted against the percentage of an isotropic spectra that produced the best fit experimental oCD spectra of the  $Na_vMs$  pore. Points are coloured by the ligand present in the film.

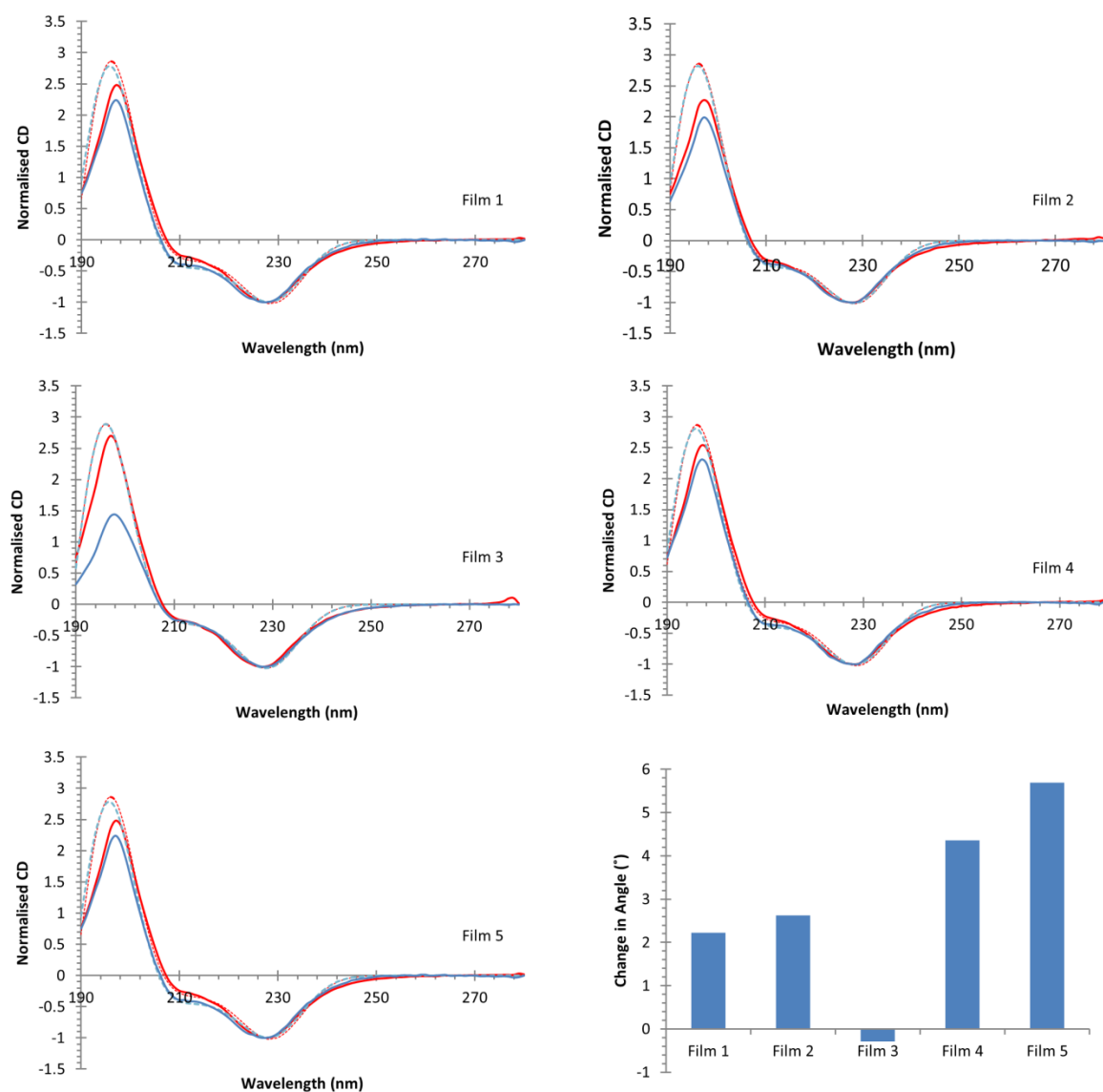


**Figure 20.** Fits of theoretical oCD spectra to oCD spectra of the Na<sub>v</sub>Ms pore before and after incubation with isoflurane. Spectra before (red) and after (blue) isoflurane incubation are overlaid with fits achieved (dashed lines) using the SMP 180 reference data and an isotropic spectrum. The fits were constrained so each pair of spectra had the same proportion of isotropic spectra. The difference in angle of the fitted spectra is shown for each film (bottom right).

These data combined give an estimate of a maximum change in tilt of  $6^\circ$ . It should be noted that this does not mean a change of  $6^\circ$  in an individual helix but a change in average angle. For comparison figure 21 shows the tilt angles of the helices within prokaryotic  $\text{Na}_v$  crystal structures. The average given is weighted by the length of the alpha helix as the longer the helix the greater the contribution to the oCD spectra. These show a difference of 5 to  $8^\circ$  degrees. This shows the changes in angles observed by oCD is in a reasonable range to represent the difference between open and closed states of a sodium channel pore. Further the absolute values for angles obtained by fitting to reference from fitting SMP180 and DeJongh reference spectra of 28 to  $34^\circ$  are reasonable values for the average angle of  $\alpha$ -helices within a prokaryotic  $\text{Na}_v$  pore.

Protein	Helix Tilt (°)				weighted average
	S5	P1	P2	S6	
NavMs pore (3zjz)	22.0	66.1	62.2	39.1	36.8
NavMs full length (5hvx)	24.7	65.0	63.0	41.9	34.3
NavAb (3rvy)	25.1	63.8	59.8	34.3	28.3
NavAb T206F V213Y (5vb2)	25.7	64.0	61.0	28.0	27.7
NavAb truncation (5vb8)	24.4	63.2	60.2	38.2	28.3
NavRh (4dxw)	34.6	62.6	64.3	35.1	31.4
NavAe (5hk7)	21.6	66.1	63.0	33.0	31.8

**Figure 21. Tilt values expected from prokaryotic NaV crystal structures.** The tilt values for the pore helices (S5 and S6) and turret loop helices (P1 and P2) were calculated for the crystal structures shown in parentheses using AnglerFish. An average weighted to the length of the helices is given and the structures that are in an open conformation are highlighted in green.

## Discussion

While spectra indicative of oriented Na<sub>v</sub>Ms could be obtained, oCD analysis of entire membrane proteins is still in its early stages. As spectra generated from the same conditions could vary considerably especially in the 190 peak reproducibility is still an issue. This highlights the importance of finding complementary techniques to assay film formation. While solid state NMR may require prohibitive amounts of protein, it is possible indirect methods could be used to assay the lipid bilayer in oriented samples. These include phosphorus NMR of the phospholipid phosphates or fourier transform infra-red spectroscopy of the lipid tails. <sup>31</sup>P MASNMR experiments can give information on the cross-sectional area available to the phosphate head groups of the lipids and hence can report on membrane curvature (*Guo et al., 2002*). While the FTIR bands arising from lipid CH<sub>2</sub> groups is dependent on the conformational disorder of the acyl chains and will hence reflect bilayer morphology (*Chia and Mendelson, 1996*). While these techniques may not be able to give precise data on the arrangement of bilayers they could be used to trial methods for producing liposomes and then bilayers that give reproducible spectra and hence reproducible films with or without the need for recombinant protein. They could also be used to check for any distortions or phase changes in bilayers caused by the addition of ligands in the absence of protein.

Despite these difficulties spectral differences could be seen on the binding of isoflourane to bilayers containing Na<sub>v</sub>Ms. Further experiments are required to confirm the specificity of this interaction as well as those suggested by the ligand screening. While oCD spectra can be collected (and used as baselines) for lipid films you would not expect these to vary on addition of ligands unless the ligands are optically active or induce an optically active arrangement of lipids. In order to assess whether the ligands are causing a conformational change within Na<sub>v</sub>Ms oCD experiments would need to be performed on proteins known to not bind the ligand in question. This could be a mutant of Na<sub>v</sub>Ms confirmed electrophysiology to abolish the ligands effect, to assess if the ligand changes how Na<sub>v</sub>Ms sits in the membrane without altering its conformation. More generally any transmembrane  $\alpha$ -helical peptide could be used to see if the ligand alters the ability of all proteins to sit in the membrane.

An exact quantitative analysis of any data collected is still unclear as the angles obtained from fitting are entirely dependent on the reference spectra used. So far there has been no independent verification of oriented reference spectra for  $\alpha$ -helices. The difference in proposed parallel and perpendicular alpha helical spectra show the ambiguity in deconvolution of  $\alpha$ -helical isotropic spectra into these two components. To quantitatively analysed oCD data the relative

contributions of the directions transitions making up the 222 nm band will need to be deduced. Ideally this can be achieved with a series of oCD spectra at different angles.

# Single molecule FRET studies of NavMs

---

## Introduction to smFRET

Förster resonance energy transfer (FRET) has been studied as a phenomenon and used as a tool for studying molecular proximities in biology for decades, but recent advances have dramatically increased the resolution and applicability of the field to structural biology. FRET is based on the transfer of energy from a donor to an acceptor fluorophore, exciting the acceptor without the emission and subsequent absorption of a photon. The efficiency of the energy transfer is proportional to  $1/r^6$  so can be used to assess the interatomic distance between fluorophores (*Stryer and Haugland, 1967*). The Förster radius ( $R_0$ ) of a dye pair where the FRET efficiency is 50%, is used to report the distances over which FRET will be detectable. This is dependent on the spectral overlap of the pairs' emission and absorption spectra in addition to their relative quantum yields (*Hohlbein et al., 2014*). In practice this makes FRET useful on the scale of  $\sim 10$  to  $100 \text{ \AA}$ . FRET will occur when the energy to excite the acceptor fluorophore is the same as the energy that would be emitted as a photon on relaxation of the donor. This means FRET can occur when the absorption spectra of the acceptor overlaps with the emission spectra of the donor, with the probability of FRET increasing with the greater the overlap. The occurrence of FRET is monitored by measuring the ratio of fluorescence at the donor and acceptor emission wavelengths, with the higher the proportion of the acceptor emission the higher the efficiency of FRET and the lower the inter-fluorophore distance (*Selvin, 1995*).

FRET can be performed using a standard fluorimeter or fluorescence microscope to measure the average efficiency of donor and acceptor fluorophores, to monitor the interatomic distance between them. FRET has been most frequently used to study the binding of subunits within a complex or the association of proteins. This is of great use as it is possible to perform FRET within living cells (*Sekar and Periasamy, 2003*). The ability to perform FRET at high spatial resolution is limited by the fact it will report an average efficiency for a sample. This means all molecules must be in the same state or synchronised in the case of a dynamic process, so there is only one apparent population. The ability to characterise different populations of biomolecules highlights the advantages of single molecule FRET (smFRET) where the fluorescence is measured from individual molecules/assemblies. smFRET is able to give distances for different conformations of a molecule or complex providing the conformations switch slower than the reporting frequency of the detector (*Kapanidis et al., 2004*).

For smFRET to be performed a method of resolving FRET events from individual species must be used. This can either be done specially by microscopy imaging where fluorescent species are non-overlapping or temporally where fluorescence is only detected from one species at a time. Total internal reflection microscopy (TIRF) microscopy can detect the emission from fluorophores close enough to a slide to be excited by an evanescent wave propagated by the total internal reflection of the excitation laser through the slide. TIRF is a popular method for obtaining FRET as it uses the same experimental set up as other forms of fluorescence microscopy and can give data from hundreds of fluorescent molecules at once (*Holden et al., 2010*). Analysis of this data is complex requiring the categorisation and tracking of individual fluorophores as they 'blink' by virtue of the excited state being able to relax directly to the ground state via fluorescence or via intermittent excited states without photon release (*Stefani et al., 2009; Holbein et al., 2013*). While TIRF can give extra valuable information such as the fluorescence lifetime of a dye during the experiment, practically it is usually limited to systems that can be immobilised onto a coverslip for tracking purposes (*Roy et al., 2009*).

With suitable experimental conditions confocal microscopy is able to achieve temporal resolution of FRET by obtaining data from a single molecule at a time. With a confocal volume of around 1 fl the passage of a single fluorescent species through the volume is detectable as a burst of photons. The burst is defined as a number of photons arriving at the detector within a given time frame, which can then be normalised to a fluorescence by subtracting the background counts during the experiment (*Holbein et al., 2013*). In order to detect individual bursts (i.e. a single molecule experiment), only one labelled species can be present in the confocal volume at a time, meaning the solution must be incredibly dilute, typically in the pM range. As with any single molecule technique, detecting and characterising contribution from individual molecules above the level of noise is a significant challenge, so limiting the background noise is crucial. The noise can be reduced by ensuring the fluorescence from the buffer is minimal. This makes removing the unreacted dye from the sample after labelling vital, as it will contribute heavily to the fluorescence of the buffer.

While smFRET is able to dissect different conformations, the resolution of the technique was considered too low for atomic modelling, this is because as well as a distance dependency on the FRET efficiency there is also a dependency on the relative orientation of the two fluorophores. This means accurate measurements would require constrained dyes of known orientation which is practically difficult in biology, as a single point of attachment is generally used for site specific labelling which leaves rotational freedom. Even if the dyes could be constrained an independent method of calculating or measuring the dyes' orientations would be required. This is overcome by using flexible dye linkers so the signal is contributed to by all possible orientations and an 'orientation factor' can

be used, but this leads to uncertainty in the positions of the donor and acceptor relative to their labelling, as well as errors in calculating an appropriate orientation factor (*Kalinin et al., 2012*). The accuracy of FRET can be increased to an atomic level by modelling the positions of the donor and acceptor using the distributions of efficiencies obtained from single particle measurements. This information can then be used in rigid body docking of labelled molecules or molecular dynamics restrained with FRET distances to inform biology (*Kalinin et al., 2012*).

While it is possible to monitor the efficiency of FRET from the ratio of donor and acceptor fluorescence alone, in practice this is prone to errors. This is because the excitation spectra of the acceptor fluorophore can overlap with the excitation laser causing direct excitation of the acceptor, the contribution of which is difficult to quantify. It is also possible for some fluorescence from the donor dye to be detected within the wavelength collected for acceptor emission. Comparing donor and acceptor fluorescence is also limited in FRET events of low efficiency, as the fluorescence from the donor will predominate so a low FRET fluorescent burst can be indistinguishable from donor only fluorescence; the inverse of this is also true for high FRET (*Kapanidis et al., 2004*). This is of particular importance in a heterogeneously labelled or partially photobleached sample as there is no way of ensuring that each burst is the result of a molecule with both donor and acceptor conjugated and active. Hence the ability to define the contribution from different fluorophores within a FRET event allows quantification and correction of these errors.

Sorting fluorescent bursts by the fluorophores contributing to them is achievable by the use of a second laser at the excitation wavelength of the acceptor. If the sample is exposed to both lasers alternately with a frequency high enough that each fluorophore is excited several times while traversing the confocal volume. The contribution from each fluorophore can then be calculated for a given burst without the lasers interfering with each other. This approach is known as alternate laser excitation (ALEX) (*Lee et al., 2005*). ALEX then gives data from four channels, two from each of the detectors for each of the excitation lasers. Photons from FRET events are detected in the donor excitation acceptor emission ( $D_{EX}A_{EM}$ ), while the acceptor excitation donor emission ( $A_{EX}D_{EM}$ ) channel is discarded as this only contains noise (*Hohlbein et al., 2014*). The donor excitation donor emission ( $D_{EX}D_{EM}$ ) and acceptor excitation acceptor emission ( $A_{EX}A_{EM}$ ) channels allow access to direct excitation of both the donor and acceptor. Using these channels the apparent FRET efficiency ( $E^*$ ) can be written as:

$$E^* = (D_{EX}A_{EM}) / (D_{EX}A_{EM} + A_{EX}A_{EM})$$

The contribution of each fluorophore can be assessed by calculating the stoichiometry (S) from the sum of the fluorescence from the Donor excitation channels divided by this and the acceptor excitation acceptor emission.

$$S = (D_{EX} D_{EM} + D_{EX} A_{EM}) / (D_{EX} D_{EM} + D_{EX} A_{EM} + A_{EX} A_{EM})$$

This calculation gives the raw stoichiometry, which in order for accurate FRET to be measured it is vital the stoichiometries of donor only and acceptor only species are distinct from dual labelled species undergoing FRET. Visually this is done using a plot of efficiency against stoichiometry and identifying laser intensities at which the donor only and acceptor only stoichiometries are as distinct as possible (*Hohlbein et al., 2014*).

In order to correct the raw FRET efficiency and stoichiometry the cross talk from leakage and direct excitation of the acceptor can be calculated using singly labelled species. The  $D_{EX} A_{EM}$  channel of donor only species will be entirely leaked photons, as the amount of  $L_k$  is proportional to the number of donor fluorophores this is defined as a leakage proportion  $l$  where  $D_{EX} A_{EM} = l \cdot D_{EX} D_{EM}$  for a donor only species. Substituting  $l$  into the equation for FRET efficiency gives  $l = E^*/(1-E^*)$  for a donor only species. Using similar logic the  $D_{EX} A_{EM}$  channel for an acceptor only species will be entirely photons resulting from direct excitation of the acceptor by the donor laser. This gives the direct excitation proportion  $d$  where  $D_{EX} A_{EM} = d \cdot A_{EX} A_{EM}$  which can be substituted into the stoichiometry equation to give  $d = S/(1-S)$  for an acceptor only labelled species. So for a species undergoing FRET as the  $D_{EX} A_{EM}$  channel is the sum of photons arising from FRET, leakage and direct excitation the photons arising due to FRET can be calculated from:

$$FRET = D_{EX} A_{EM} - l \cdot D_{EX} D_{EM} - d \cdot A_{EX} A_{EM}$$

Leakage from the acceptor fluorophore into the donor channel is directly accounted for as the  $D_{EX} D_{EX}$  channel will only contain photons arising from excitation of the donor. Were this not the case that would mean the donor is being excited by the acceptor excitation wavelength and a significant number of photons would be seen in the  $A_{EX} D_{EM}$  channel which in practice is not the case (*Hohlbein et al., 2014*).

For accurate FRET one further correction defined as  $\gamma$  is required. When the quantum yields of donor and acceptor fluorophore are not equal (and  $\gamma \neq 1$ ) the apparent stoichiometry of low and high efficiency FRET samples will be different.  $\gamma$  can be calculated from a linear fit of  $E^*$  against  $1/S$  and then used to correct the FRET efficiency to give an accurate efficiency of:

$$E = FRET / (\gamma \cdot D_{EX} D_{EM} + FRET)$$

Single molecule FRET studies have already made valuable contributions to the studies of ion channels. Gramicidin is an ideal channel to study via FRET as gating of the channel is dimerization dependant. This is because gramicidin monomers can diffuse independently in the plane of a membrane and only form functional channels on dimerization (*Wallace, 1986*). Hence it is possible to mix donor and acceptor labelled gramicidin and observe FRET during dimerization and hence open channels. As such Gramicidin was the first ion channel to be studied by smFRET (*Borisenko et al., 2003*), here gramicidin was labelled with Cy3 and a low conductance gramicidin mutant was labelled with Cy5. This meant homodimers containing Cy3 would form high conductance channels, Cy5 homodimers low conductance channels, and heterodimers channels of intermediate conductance. This allowed the three possible channels to be distinguished by both fluorescence and conductance. In this study bilayers were suspended between two electrodes such that simultaneous fluorescence imaging at the emission wavelengths of Cy3 and Cy5, and electrical current reading were possible. This showed good correlation of fluorescent bursts with changes in current. FRET events correlated with the intermediate conductance events, hence the formation of heterodimers. This study emphasises how the non-invasive nature and fast response time of smFRET allow for correlated simulations measurement with techniques such as electrophysiology which is especially useful for the study of ion channels.

Prior to the use of smFRET ensemble FRET measurements had been performed on the mechanosensitive channel MscL (*Correy et al., 2005; 2010*). These experiments used lysophosphatidylcholine to force closure of the channel and assessed donor and acceptor contribution by recording fluorescence before and after photo bleaching of the donor. This lead to estimates of the change in diameter on closure of  $\sim 16$  Å and an open diameter value of 25 Å. As the channels are pentameric, determining the diameter from efficiency measurements arising from distances between five randomly labelled sites required Monte Carlo simulation. smFRET studies were performed by TIRF microscopy on labelled MscL pentamers reconstituted into liposomes. This allowed the separate distances present in the pentamer to be distinguished as separate efficiency peaks and a diameter for 28 Å could be determined for the open channel. By labelling the protein at separate points within the protein distance restrictions for molecular dynamics simulations could be generated; the resulting simulations strongly supported a helix tilt model for opening of the channel (*Wang et al., 2014*).

The bacterial potassium channel KirBac has been studied by smFRET using both confocal microscopy of solubilised channels in solution and TIRF microscopy of membranes. In both cases phosphatidylinositol 4,5-bisphosphate was used to cause channel closure. The confocal experiments were able to distinguish the two separate distances in the Kirbac homotetramer as separate

efficiencies (*Sadler et al., 2016*). In a similar manner to the MsCL example labelling at the top and bottom of the channel showed different changes in diameter on gating which led to an iris-like dilation model of opening for the channel. In the TIRF experiments tandem constructs could be created containing 4 repeats of the KirBac monomer which formed functional ion channels in an architecture similar to a eukaryotic sodium channel (*Wang et al., 2016*). This allowed the channels to be labelled with a single pair of fluorophores and hence one distance to be studied at a time. Further this allowed distances between different points in the channel to be studied rather than simply studying across the channel. This showed the movement of the cytoplasmic domain towards the membrane on gating of the channel.

smFRET studies of the NMDA receptor show how structural dynamics of an ion channel can be studied *in situ* (*Sasmal and Lu, 2014*). HEK-293 cells were used where the GluN2b subunit of the NMDA receptor had been labelled with an antibody covalently linked to the Atto-594 dye, which was utilised as the acceptor fluorophore. The donor fluorophore (Alexa-532) was covalently linked to the gating ligand of the channel, glycine. It might be expected that such huge modifications to the channel and ligand would interfere with either ligand binding or movement of the channel, but this was shown not to be the case. The smFRET was performed such that patch clamp electrophysiology recordings could be made simultaneously showing the system had electrical properties consistent with the wild type. This study could then give kinetic data on the binding of the ligand to the receptor (by proximity from smFRET) correlated with current recordings across the channel.

## Methods

### Labelling

The Na<sub>v</sub>Ms pore A221C and full length A221C mutants were purified as described in Chapter 2 for dye labelling at the mutated cysteine. The cysteines were reduced by incubation for 1 hour at room temperature with 20 mM DDT (Sigma Aldrich). The excess DDT removed by a 1 ml NAP5 gravity flow desalting column (GE lifesciences) according to the manufacturer's instructions, using a 0.2% DDM 200 mM NaCl 20 mM Tris pH 7.5 buffer to both equilibrate and elute. The column was washed with 10 ml of deionised water before being equilibrated with 5ml of the above buffer. 100 µl of sample was loaded followed by 500 µl of buffer, this was left until all liquid had been absorbed into the column then the sample was eluted in a further 500 µl of buffer. This was labelled with a 10 times molar excess of Cy3B maleimide (GE lifesciences) and Atto647N maleimide (Sigma Aldrich) for 1 hour at room temperature, in a reaction volume of 200 µl and protein concentration of 2mg/ml.

The reaction occurred in Eppendorf tubes wrapped in tin foil to prevent photobleaching of the dyes. Prior to labelling both dyes were dissolved in DMSO (Sigma) to a concentration of 20 mM. The excess dye was removed with a second NAP5 desalting step using the same protocol as the first. For samples where the His tag was left un-cleaved the second NAP5 desalting step was replaced by binding to 250  $\mu$ l Ni-NTA beads in a gravity column. Beads were washed with 20 ml of deionised water then equilibrated with 5 ml 0.52% HEGA-10, 200 mM NaCl, 20 mM Tris, pH 7.5 buffer in the gravity column. 500  $\mu$ l of labelled protein was then loaded onto the column which was washed with buffer the same as the equilibration until no absorption could be detected from the dyes in the flow through (5 ml) via a nanodrop spectrophotometer. The protein was eluted with 3 ml of the same buffer with the addition of 200 mM imidazole. Samples were filtered using a 0.22  $\mu$ m syringe filter (Millipore) prior to data collection. Labelling was checked on SDS-PAGE gels. 10  $\mu$ l samples were loaded onto 4-12% Bis-Tris gels (Novex). These were run at 200 V for 45 min in MES buffer (Thermo Scientific). Prior to staining gels were imaged on a Typhoon FLA9000 fluorescence scanner (GE life sciences) at 532 and 633 nm excitation wavelengths. These were then stained as described in chapter 3 to align the molecular weight ladder.

## Data collection

smFRET experiments were performed at the Central Laser Facility in the Rutherford Appleton Laboratories, Oxfordshire with the assistance of Benjamin Coles. The donor and acceptor excitation lasers were 561 nm 25  $\mu$ W (Jive from Cobolt) and 635 nm 30  $\mu$ W (CUBE from Coherent), respectively both continuous wave. The beams from these lasers were combined with a dichroic mirror and focussed to a confocal observation volume of  $\sim 1 \mu\text{m}^3$  above the objective lens. The donor and acceptor laser powers were set to 9 and 4.5% respectively and alternated at the frequency of 10 kHz. This was such that single FRET bursts could be detected from donor and acceptor labelled DNA standards and acceptor- or donor-only species gave bursts of a separate stoichiometry. This is the standard set up for ALEX FRET at the central laser facility and was set up by Benjamin Coles and Timothy Craggs (Physics department, University of Oxford) based on the apparatus in (Santoso *et al.*, 2010). Labelled protein was then pipetted onto a coverslip over the objective lens, the objective manually focused onto the coverslip (where confocal rings could be seen), and then mechanically elevated by 25  $\mu$ m to ensure the confocal volume is within the sample. The protein was then diluted to a point where single bursts could be detected above noise and data collected for five minute intervals. Dilution was performed by pipetting buffer into the sample to find a good working dilution in the first instance then a fresh dilution was made with this ratio for further data collection. Dilutions were typically 1 in  $10^6$  for the sample after free dye was removed achieved using serial dilution of 1 in 100. Data was collected as arrival times of photons at the

photon detectors for the donor and acceptor emission wavelengths. The lasers and photon detectors were controlled by a virtual environment created in LABView by Benjamin Coles to ensure accurate correlation of excitation laser with the arrival times. This gives data in 3 channels; donor excitation donor emission ( $D_{EX} D_{EM}$ ), acceptor excitation acceptor emission ( $A_{EX} A_{EM}$ ), and donor excitation acceptor emission ( $D_{EX} A_{EM}$ ). As described earlier the acceptor excitation donor emission channel is discarded. Data was saved in 5 minute chunks so problems with the set up would not invalidate all the data up to that point in longer data collection runs.

Data Processing Photon bursts were defined and characterised from the photon streams by custom MATLAB software written by Johannes Hohlbein (Physics department, University of Oxford) based on the algorithms in Kapanidis et al., 2004. Photon bursts caused by fluorophore labelled protein traversing the confocal volume were defined as containing photons that had over a threshold number of neighbours within a time interval. Final parameters used for analysis were a minimum of 7 neighbouring photons and a time interval of 100  $\mu$ s. Data sets were used where between 70 and 300 FRET bursts were observed in the 5 minute intervals data was collected for. This is enough that it is unlikely the observed bursts are genuine and not due to alignments of noise within the channels and few enough that each burst can be observed as a separate event (less than 1 per second).

## Results

The Na<sub>v</sub>Ms pore was successfully labelled separately with both Cy3B (donor) and Atto647N (acceptor) and with a combination of both. In the first instance this was done with a 1:1 mix of donor to acceptor, this however lead to an overabundance of fluorescence in the A<sub>EX</sub> A<sub>EM</sub> channel. UV spectroscopy of this sample (figure 1) showed an overabundance of Atto647N over Cy3B given extinction coefficients of 130,000 and 150,000 M<sup>-1</sup>cm<sup>-1</sup> respectively. It is vital that a labelling ratio as close to 1:1 as possible is achieved as given there are 4 independent labelling sites there will be a distribution of labelling ratios within molecules. Even with a 1:1 labelling ratio 12.5% of molecules will be labelled with only donor or acceptor so give rise to no FRET; the further the labelling deviates from 1:1 the greater the proportion of donor only or acceptor only labelled species. As both donor and acceptor use maleimide chemistry to react with the free cysteine you might expect a similar labelling efficiency. However as seen in the structures shown in figure 2 Atto647N is a much more hydrophobic molecule so it could have an increased reaction rate due to its' higher affinity for protein-detergent micelles. As the malimide moiety of Atto647N is connected to the fluorophore by a more flexible linker it is possible this group is more sterically available to the cysteine side chain for reaction.

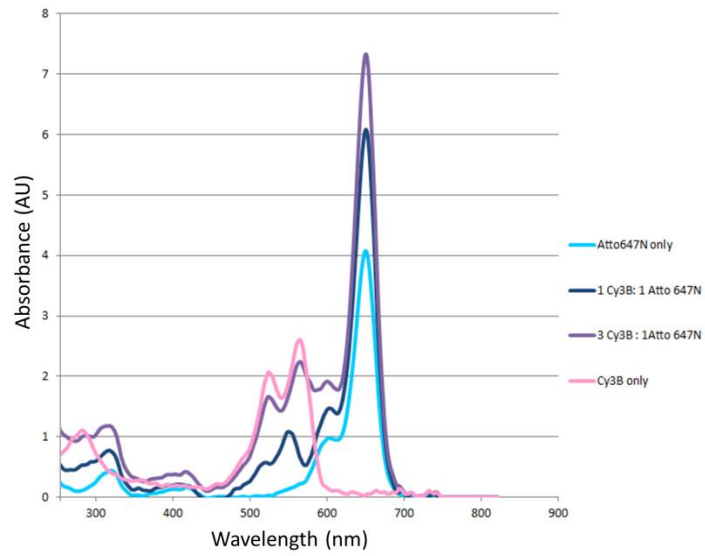


**Figure 1. UV-Visible absorbance spectra of the dye bound  $Na_vMs$  pore 221C.** Protein was labelled with Cy3B and Atto647N in the ratios indicated, spectra were collected on a nanodrop spectrophotometer.

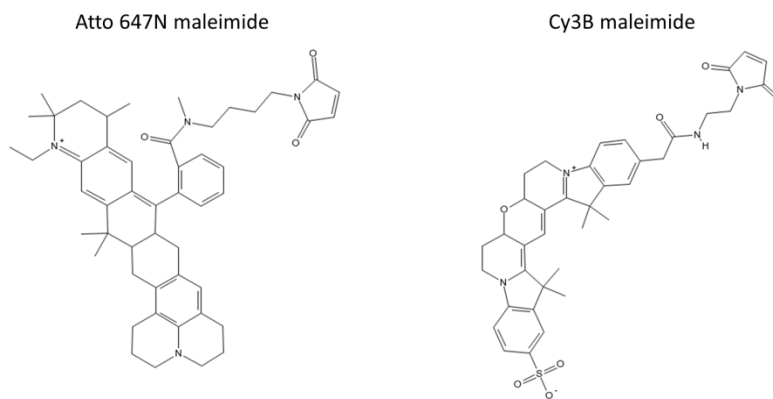


**Figure 2. Atomic structures of FRET dyes.** Structures are shown for Atto 647N (the acceptor) Cy3B (the donor) dyes, with the maleimide moiety and point of attachment aligned top right.

A 3:1 mixture of donor to acceptor gave an improved labelling ratio, with fluorescence gels showing labelling of the protein by both dyes (figure 3 left). However at a concentration where FRET bursts could be observed a high background fluorescence was present. This made detecting bursts over noise difficult leading to a low rate of data acquisition. The high background fluorescence was thought to be due to unreacted dye still within the sample. While the desalting column saw the free dye elute separately to the labelled protein it is possible unreacted dye could still be associated to protein containing micelles. In order to combat this Na<sub>v</sub>Ms A221C was purified with the His-tag uncleaved (as shown in Chapter 2). Allowing the second desalting step could be replaced with Ni<sup>2+</sup> affinity. This immobilised the protein during dye removal, so buffer could be washed over the protein allowing non-covalently associated dye to unbind and elute. The detergent in the elution buffer was changed to HEGA-10 from DDM as it has a much lower aggregation number, too low to be measured accurately compared to 78-140 for DDM (*Anatrace data sheet*). The lower aggregation number should provide less of a hydrophobic volume associated to the protein for dyes to bind to non-specifically. The gels in figure 3 show a much reduced free dye band when dye was removed by Ni<sup>2+</sup> affinity, as opposed to the size exclusion based desalting column. The gels also show oligomeric banding of the pore as is seen with the full length Na<sub>v</sub>Ms, this can be explained by the lack of a heating step in the SDS sample preparation leaving higher oligomeric states of the pore intact.

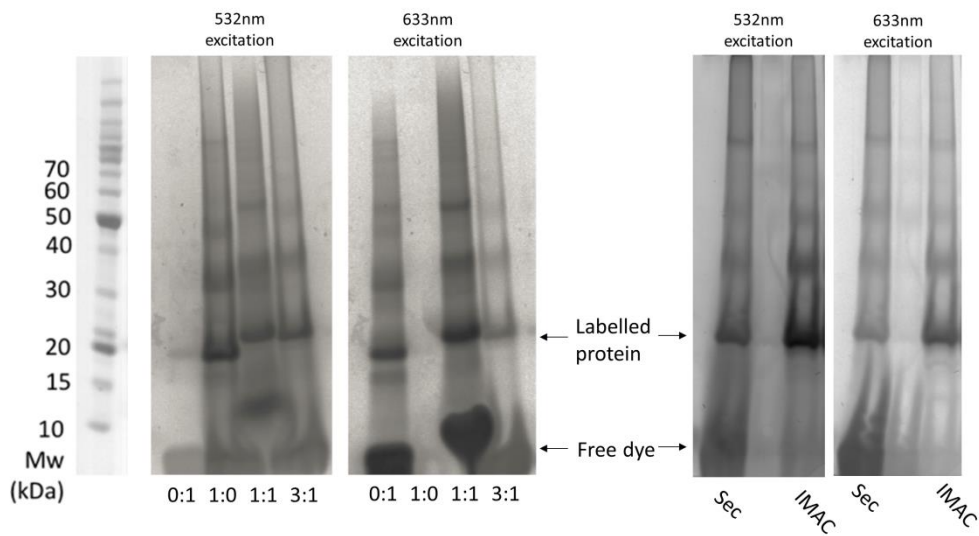


**Figure 3. Fluorescence gels of the dye bound Na<sub>v</sub>Ms pore A221C.** Protein was labelled with Cy3B and Atto647N imaged under excitation wavelengths 532 nm and 633 nm to show Cy3B and Atto647N respectively. Different ratios of dye used in labelling are shown (left) with ratio of Cy3B to Atto647N (donor to acceptor) indicated for each lane. The difference in labelled protein purification by a size exclusion desalting column (Sec) and Ni<sup>2+</sup> affinity (IMAC) are shown (right) for protein labelled with a 3:1 ratio of donor to acceptor.

Single major populations of FRET could be seen on the efficiency stoichiometry plots for the Na<sub>v</sub>Ms pore alone, and in the presence of lidocaine and veratridine as shown in figure 4. It might seem counter intuitive for there to be a single distribution of stoichiometry values given the 4 independent labelling positions. The 3 labelling ratios (1:3, 1:1 and 3:1) that give rise to FRET would have stoichiometries of 0.25, 0.5 and 0.75 respectively and be in a distribution of 4 to 6 to 4. With sufficiently broad peaks these 3 species would appear as a single Gaussian curve.

Distinct peaks within ES plots were seen for Na<sub>v</sub>Ms pore samples labelled with only donor or acceptor fluorophores as shown in figure 5. These were separate to those for the FRET events indicating they would not disrupt calculation of FRET efficiency and could be used to calculate leakage and direct excitation proportions.

As Na<sub>v</sub>Ms did not show a great enough variation in FRET efficiency between conditions for the  $\gamma$  correction factor to be calculated a series of DNA standards labelled with the same fluorophores in the same buffer was used. Each of these showed a distinct ES peak which is shown in figure 6. The E to 1/S plot showed a linear fit and could be used to calculate a  $\gamma$  value of: 1.24

These parameters were used to calculate the corrected ES plots for the full length and pore Na<sub>v</sub>Ms constructs shown in figure 7. These corrections drastically shift the efficiency peaks to give values of 0.5 and 0.7 for the full length and pore respectively. Using the published value of  $R_0$  for the Cy3B Atto647N dye pair of 62 Å (*Holden et al., 2010*) these efficiency values give distances of 60.0 and 53.8 Å.

For reference raw traces of the counts of the photons in the three recorded channels are shown in figure 8. In both cases there are far more counts in the D<sub>EX</sub>D<sub>EM</sub> channel than either of the others. This being said significant bursts in this channel co-localise with bursts in the other two channels for the pore construct indicating FRET events. While the same is true for the full length construct the greater the degree of noise in the D<sub>EX</sub>D<sub>EM</sub> channel could mean this co-localisation is incidental. This with the fact the apparent efficiency for the full length was 0.5 (exactly mid-way within the possible range) sheds doubt on if the bursts classified by the software were true events or noise.

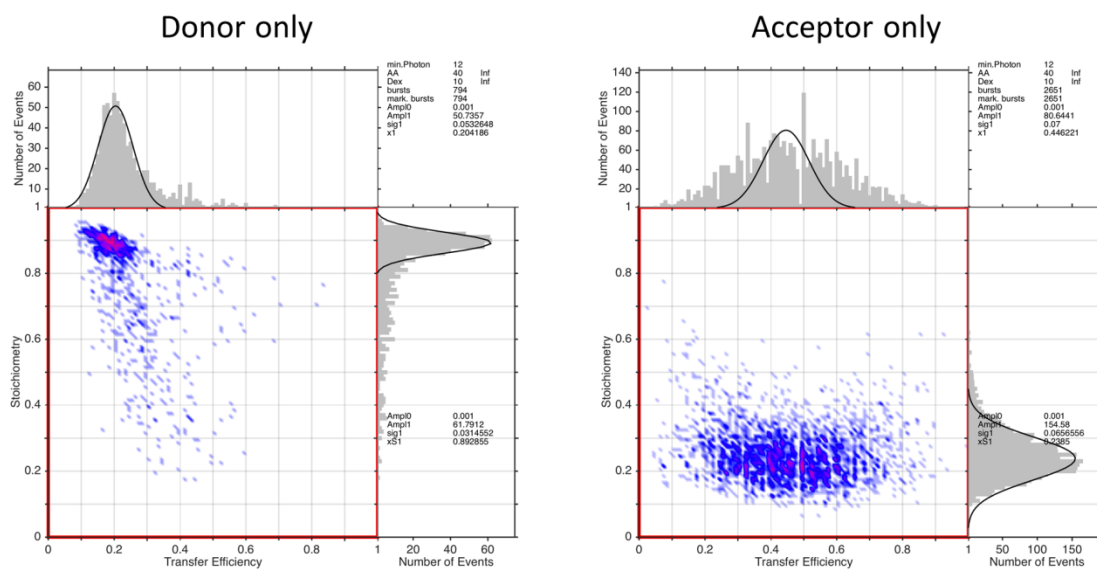


**Figure 5. FRET efficiency stoichiometry plots for the NaVMs pore A221C labelled separately with Cy3B and Atto647N. Peaks for efficiency and stoichiometry were defined by Gaussian curved fitted to histograms of the bursts' values.**

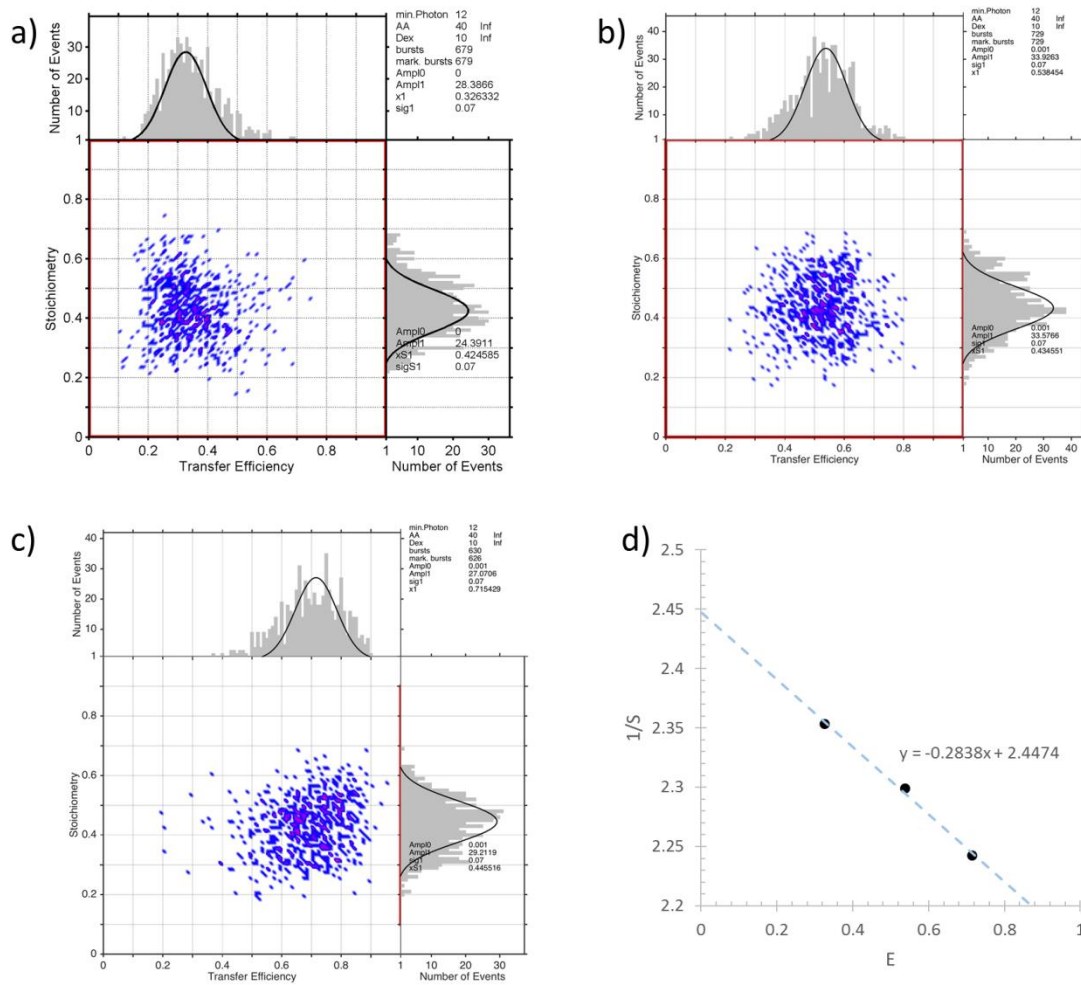


**Figure 6. FRET data from DNA standards.** (a-c) FRET efficiency stoichiometry plots for reference DNA duplexes of different lengths labelled with Cy3B and Atto647N showing low (a), medium (b), and high (c) FRET. Peaks for efficiency ( $E$ ) and stoichiometry ( $S$ ) were defined by Gaussian curves fitted to histograms of the bursts' values. A plot of  $1/S$  against  $E$  is shown (d) with the equation for a linear fit in order to determine the correction factor  $\gamma$ .

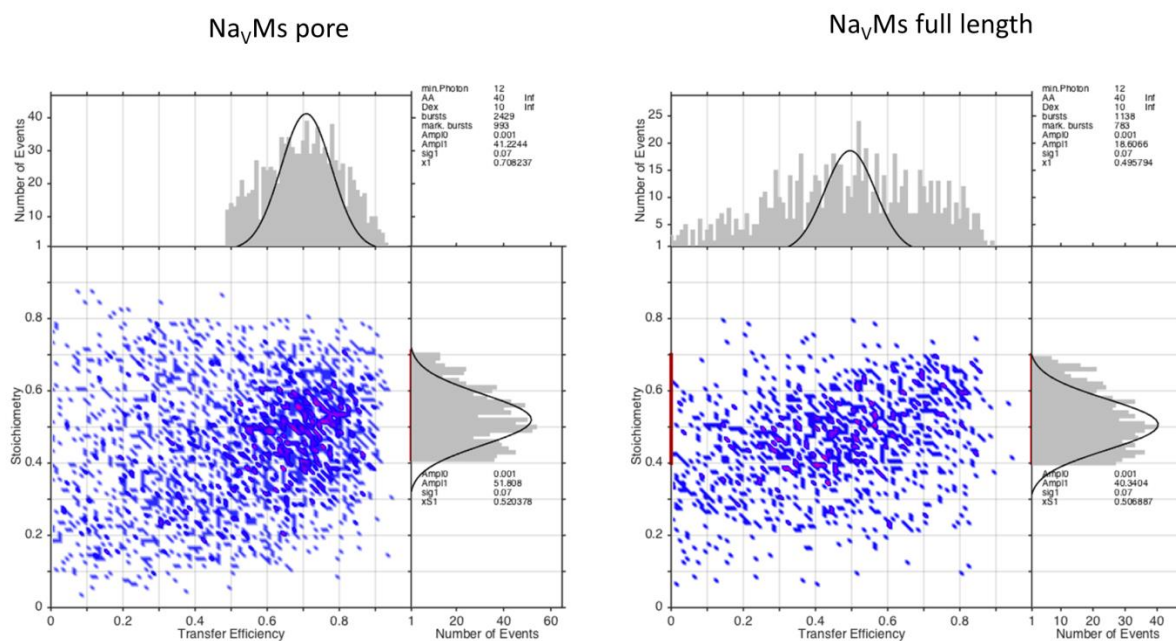


**Figure 7. Corrected FRET efficiency stoichiometry plots for  $Na_VMs$ .** Plots for both the pore and full length  $Na_VMs$  alone are each shown, both with the A221C mutation. Both samples are labelled with Cy3B and Atto647N. Peaks for efficiency and stoichiometry were defined by Gaussian curved fitted to histograms of the bursts' values. The range of stoichiometry values used for efficiency fitting are shown as red lines.

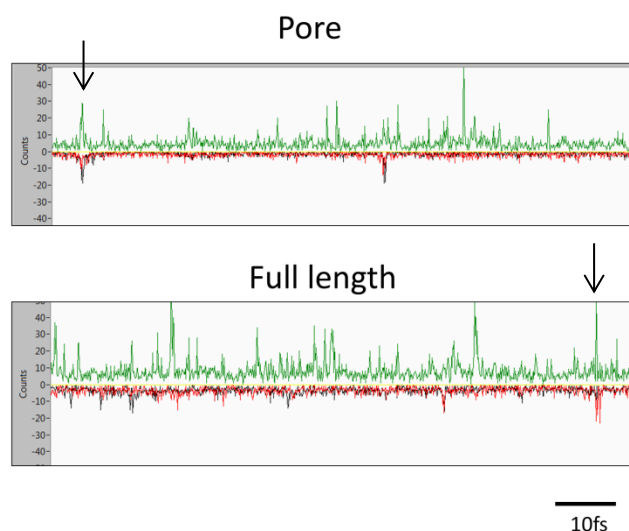


**Figure 8. examples of raw photon bursts from fluorescently labelled  $Na_VMs$ .** The green line represents counts in the  $D^{EX} D^{EM}$  channel, the red the  $A^{EX} A^{EM}$ , and the  $D^{EX} A^{EM}$  (ie. the FRET) channel. All counts were positive but the  $A^{EX} A^{EM}$ , and the  $D^{EX} A^{EM}$  are shown as negative for clarity. A scale bar of 10 femtoseconds is shown below. Example bursts corresponding to FRET events are highlighted by black arrows.

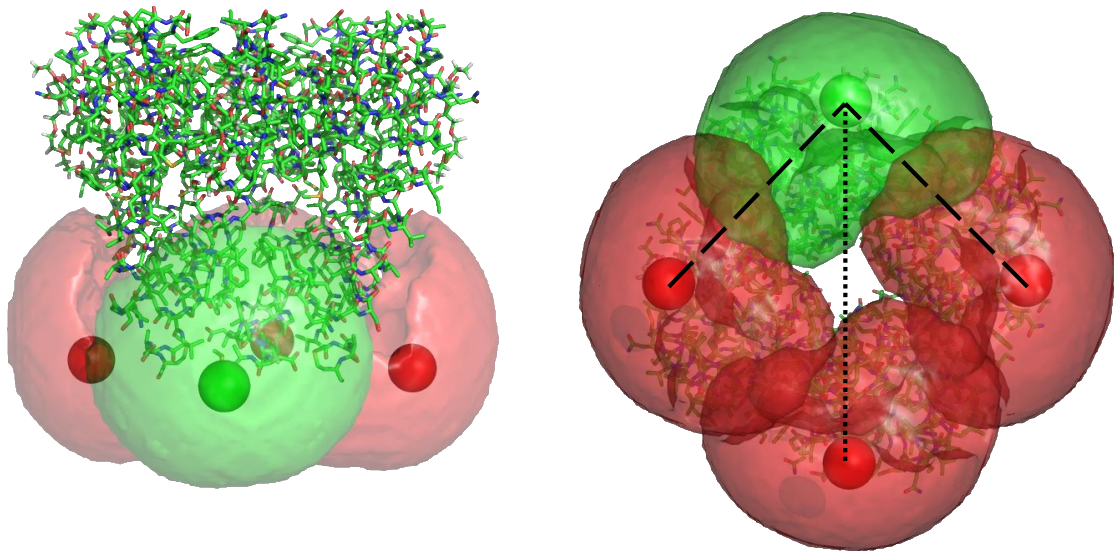
## Discussion

The distances calculated by FRET are the distances between the average position of the donor and acceptor fluorophores. Due to the requirement of a long flexible linker this is significantly greater than the distance between the attachment points. Modelled distances for Atto647N and Cy3B maleimides conjugated to cysteine 221 the Na<sub>v</sub>Ms pore are shown in figure 9. These predicted distances are much shorter than those calculated from the ALEX measurements indicating accurate FRET has not been achieved. While it is possible the protein denatured after dye labelling altering the inter-dye distance. This seems unlikely as the denatured protein tends to aggregate and the fluorescent bursts were consistent with protein tumbling freely in solution. It is more likely that the calculation of  $\gamma$  from DNA standards is inappropriate to this study. While the DNA standards were performed in the same buffer as the protein, detergent micelles would not associate around the DNA as it does with the protein. Hence it is possible the different local environment of a micelle bound membrane protein may alter the spectral properties of the fluorophores. These same effects could also alter the value of  $R^0$  from previous calculated values.

It should be noted that due to the wide efficiency distributions it was not possible to observe the two distances as separate peaks, and the multiple distances may indeed contribute to the width of the E peak. The expected efficiency would not be an average of the two distances as the two distances are not present in equal quantities. Figure 10 shows the distances measurable in different labelling schemes of an individual channel. This shows for species with a 1:1 ratio of donor to acceptor the short distance will be represented three times as much as the long. However a 3:1 labelled species would have a 2:1 ratio of short to long distances observable. The exact ratio of short to long distances present in the efficiency peak is then dependant on the range of stoichiometry values of the bursts used as the 3:1 labelled species will have stoichiometries further from 0.5. These limitations show the value in being able to precisely define the positions dyes will conjugate to a molecule. This scheme is the ideal scenario where the protein is 100% labelled, where each cysteine residue is conjugated to a dye. As labelling efficiency decreases so does the proportion of species where FRET is possible, as the more unreacted cysteine residues the higher the probability a molecule will be labelled with only one of the dyes. Were Na<sub>v</sub>Ms to be labelled with only one donor and acceptor fluorophore per channel the efficiency peak would represent a single distance and there would be no ambiguity in which interatomic distances are contributing. In practice this could be achieved by creating a species with only 2 labelling sites as any molecule labelled with any combination other than one donor and one acceptor will not give rise to FRET. This could be achieved by creating a tandem construct as was done for KirBac (*Wang et al., 2016*), however previous attempts to create such a construct for Na<sub>v</sub>Ms in order to create an asymmetric selectivity

filter proved unsuccessful. The CTD coiled coil could prove useful in producing a species with only 2 labelling sites as methods for generating sequences of coiled coils which only associate in specific orders have been developed (*Woolfson, 2017*). Were two Na<sub>v</sub>Ms monomer constructs with the CTD sequenced designed to ensure they associated into a tetramer with like monomers opposite it could be engineered such that only 2 monomers contained cysteines for labelling. While this approach would give the distance across the diameter of the channel, the prospect of designing asymmetric tetramers gives further opportunities for distance measurement. A tetramer could be generated with three copies of a monomer without cysteine residues and one copy of a monomer with 2 cysteines. This would allow measurement of distances between different domains within the protein, for example the hypothesis that the CTD rises and falls during gating (see chapter 1 figure 12).

Another approach to mitigating the problem of variable labelling ratios is to use a method that can report on the distance between two copies. homo-FRET is possible for fluorophores which have emission spectra that overlap significantly with their own absorption spectra. While it is not possible to monitor homoFRET by a change in wavelength it is possible to use the polarisation of light (*Bastiens et al., 1992*). Due to the orientation dependence of fluorescence a stationary fluorophore excited by polarised light will fluoresce polarised light. However in practice fluorophores move so polarisation is lost proportion to the speed of reorientation between excitation and emission, this is fluorescence anisotropy and often used to report on the mobility of a fluorophore (*Weber, 1954*). As FRET is a non-radiative energy transfer polarisation is also lost so for a transition where the overall tumbling of a molecule is minimal the loss of polarisation will be proportional to the transfer efficiency of homoFRET and hence distance (*Bastiens et al., 1992*). This is especially powerful in the case of membrane proteins as their tumbling can be restricted by their inclusion in bilayers, and even in the case of a solution experiment the movement of the gating helices is unlikely to effect the overall size and shape of the molecule. Another method to measure the distance would be DEER EPR which can give the distance between labels containing unpaired electrons, as was first used to define the structure of the Na<sub>v</sub>Ms CTD (*Bagneris et al., 2013*). However this required cooling to around 50 K so would not be able to give data from a native like environments but provide information in snapshots more akin to X-ray diffraction or cryo-electron microscopy.



	Distance (Å)	FRET
.....	40.9	0.85
— —	28.8	0.96

**Figure 9. Simulated accessible volumes simulated for dyes conjugated to the  $Na_vMs$  pore.** Simulations were performed using the software from Kalinin et al., 2012. The accessible volumes are shown as translucent surfaces and their centres as solid spheres with Cy3B in green and Atto647N in red. The two distances present in  $Na_vMs$  are shown as dashed and dotted lines and their expected FRET efficiencies are shown below.

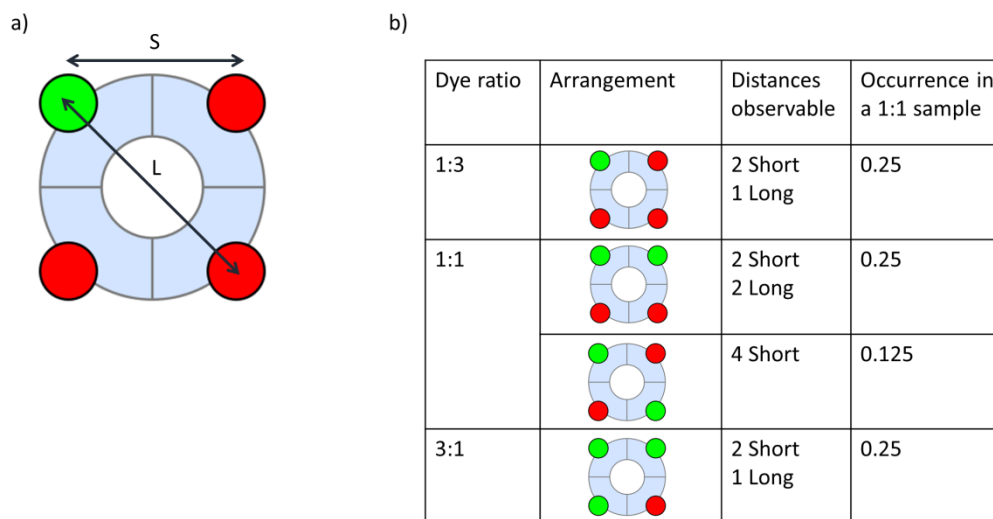


**Figure 9. Possible FRET labelling schemes of a symmetric labelled tetramer.**  
 The short and long distances observable are shown in a) with the numbers of these distances observable for different arrangements of fluorophore in b)

The FRET efficiency peaks seen also show the limitation of working at such high efficiencies. With the distributions seen were the interatomic distances to decrease this may be unobservable; this is because for the maxima of the peak to increase in efficiency some of the bursts within would have to have an efficiency of above 1 which is impossible. In order to assess interatomic distances this low it would be advisable to switch to a dye pairing with a lower Förster radius.

While the efficiency value for the full length Na<sub>v</sub>Ms is not reliable to give an accurate distance it is interesting the distance would be shorter than the pore, given the recent crystal structure of the full length Na<sub>v</sub>Ms (*Sula et al., 2017*). This structure is shown in figure 10 highlighting the position A221C, where the fluorescent dyes are conjugated. In the crystal structure there is no difference in the interatomic distances between the labelled residues in the pore and the full length. There are however interactions between the end of S6 and the voltage sensor in the full length structure, not possible in the pore. It is possible in solution the pore is taking a more closed conformation than is seen in the crystal structure, while the extra interactions in the full length stabilise a more open conformation. This would explain the shorter interatomic distance seen in the pore construct by FRET.

It should however be noted that in the full length the labelled residue is oriented towards the S4-S5 linker. This means it is unlikely the protein could have exactly this conformation in solution with conjugated dyes. This inaccessibility could explain the unreliability of the full length results, with the reaction of the dye causing denaturation of the protein preventing intramolecular FRET. To test this size exclusion chromatography of the labelled protein should be performed to ensure that it is still monodisperse.

As FRET reports on the centres of the distributions of fluorophores, any difference between the pore and full length may also be due to the difference of the range of conformations sterically possible for the dyes. In particular the presence of the voltage sensors would limit the ability for the dyes to bend up (towards the extracellular end); this could artificially increase the donor-acceptor distance slightly. It is also worth considering that the accessibility of the dyes only considers the protein and not the detergent micelle. As we have already observed one dye seems to have a higher affinity for detergent than the other it would be informative to determine dye accessibility from an ensemble of structures generated by all atom molecular dynamics with detergent molecules present.

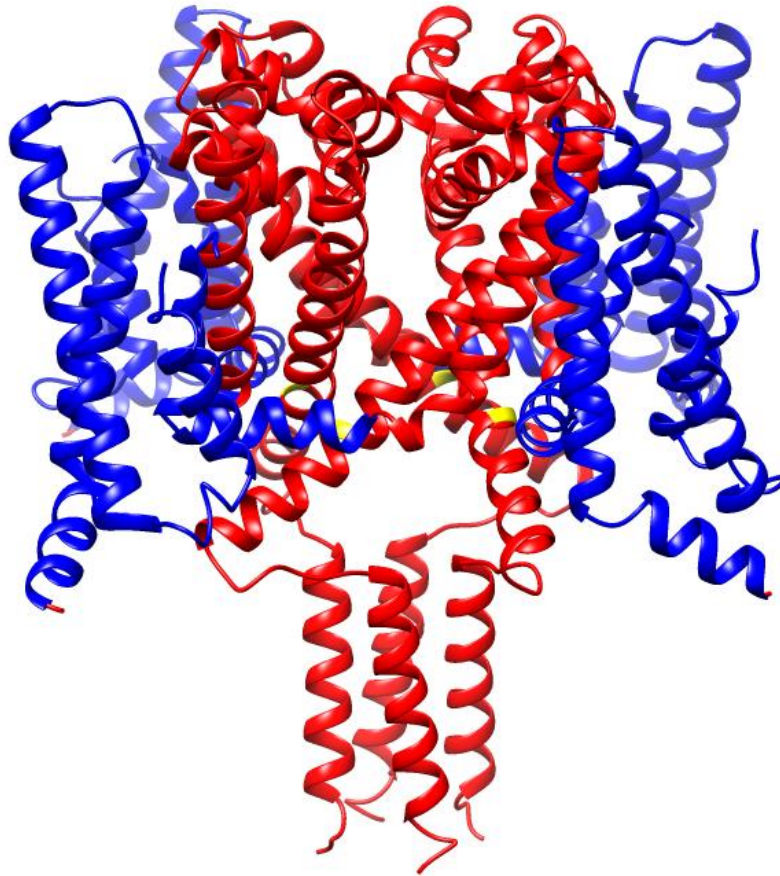


**Figure 10. The conjugation position of the full length NaVMs.** *The structure shown is PDBID 5hvx with the pore and C-terminal domain shown in red and the voltage sensor in blue. The point of attachment for dyes, the A221C mutation, is shown in yellow.*

# Conclusions and Future Work

---

The discovery and study of prokaryotic Na<sub>v</sub>s has led to a great deal of insight into the structure-function relationship of voltage-gated sodium channels including their eukaryotic counterparts. This includes the determination of the gating charges of the S4 voltage sensing helix, the molecular basis for sodium selectivity, and the elucidation of the local anaesthetic binding site. Despite these advancements, the structural changes that underpin gating of the channel are still unclear. This is in part because the crystal structures solved are of channels from different organisms in different conformations, but not of the same channel in multiple conformations. This leads to an ambiguity in whether the different conformations shown in the different crystal structures are due to the protein sequences, or crystallisation conditions used. As the conformations of structures that can be obtained by crystallography are limited to those present in conditions amenable to crystallisation, independent techniques for assaying Na<sub>v</sub> conformations are desirable as complementary methods. This study has presented alternative methods for assaying the conformation Na<sub>v</sub> structures.

In order to define the conformations of existing channels, the AnglerFish webserver was established. This parameterises the orientation of pore-forming  $\alpha$ -helices given atomic co-ordinates. In addition to showing the ranges of conformations seen in prokaryotic Na<sub>v</sub> pores so far, it provides a framework for describing dilation in  $\alpha$ -helical bundles in other kinds of proteins. How useful this will be in describing pore depends on how widely the webserver is used and more importantly whether the definitions of tilt and swing angles are adopted. Further developments in AnglerFish would be best placed making the calculations more convenient to structural biologists, by incorporating anglerfish into existing practice. This could be done by adapting the code to be a plug-in for existing molecular graphics software. This would negate the need for files to be uploaded to a webserver and have the added benefit that the output could be displayed graphically on the structure in question.

Constructs of the prokaryotic Na<sub>v</sub> from *Magnetococcus marinus* were successfully purified for biophysical characterisation. This homologue was chosen due to the wealth of structural data available. These channels could be labelled such that single molecule FRET bursts were detected in solution. The introduction of the ligands veratridine and lidocaine did not give rise to a structural change large enough to elicit a quantifiable change in the FRET efficiency of this channel. This could either be down to a lack of binding under the experimental conditions or a change too small to detect. Further work with a different dye pairing could bring the FRET efficiency into a region more sensitive to subtle changes, as the data presented here was close to the maximum possible

efficiency. This work also suggests that using DNA standards to calculate the correction factor was inappropriate. Further experiments would benefit from multiple labelling sites expected to be at very different distances. This would allow measurement of low and high FRET on the channel being studied, to calculate the correction factor. The decision was made to pursue confocal smFRET in solution as the isotropic tumbling was seen to yield more accurate results (*Sisamakris et al., 2010*). As only qualitative assessments could be made, FRET in a more native environment may be more relevant to studies of Na<sub>v</sub>s. It is possible to measure FRET from proteoliposomes, while these tumble too slowly to effectively characterise single bursts within a confocal volume. Proteoliposomes amenable to total internal reflection (TIRF) measurements, with the liposomes associated to the coverslip, tracking the fluorescence from individual molecules. A full length Na<sub>v</sub>Ms construct was also purified with a cysteine in the same position as the pore construct. This led to FRET bursts of a lower efficiency suggesting a greater distance. However due to the large range of efficiencies of recorded FRET bursts and centring on an efficiency of 0.5 it is possible these measurements were due to noise. Despite the limitations this study suggested smFRET can act as complementary method to crystallography for the study of Na<sub>v</sub>Ms.

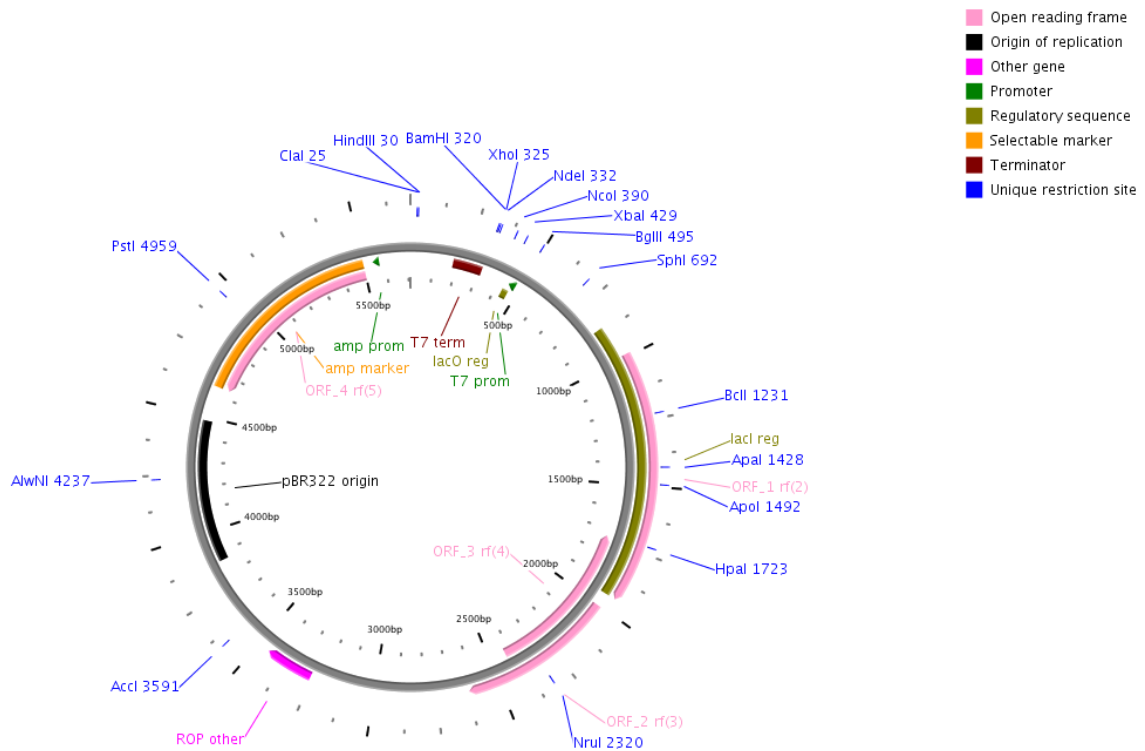
Oriented circular dichroism spectra were collected for Na<sub>v</sub>Ms pore films. This represents the first time that oCD has been used to characterise a functional protein rather than a peptide. The spectra were indicative of tilted  $\alpha$ -helices within a bilayer, as would be expected from the Na<sub>v</sub>Ms crystal structure. Oriented films could also be formed in the presence of Na<sub>v</sub> ligands. The inclusion of the ligands veratridine and isoflurane altered the spectra in a fashion indicative of an increase in tilt angle. An increase in tilt angle is consistent with the structural changes that upon closure of the channel. As oCD reports on the angles of helices with respect to the beam further control experiments would be needed to determine if the presence of these ligands is changing the conformation of the protein instead of either the angle of the whole protein within the membrane or the ordering of the membranes themselves. These observations are based on the ratio of the negative CD peaks, as thus far the magnitude of the positive peak at around 190 nm has been very inconsistent between replicate samples. This is likely to be due to artefacts in the formation of some protein-lipid films. In order for accurate oCD measurements to be made complementary methods will need to be used to assay film quality and quantify any artefacts that could interfere with the spectra. Atomic force microscopy (AFM) would allow the distribution of channels at the top layer to be characterised as well as the surface structure of the film. While it will only give data on the top layer, the distribution of protein would be a useful parameter as an inhomogeneous distribution is what gives rise to absorbance flattening (*Whitehead and Park*). In terms of assaying the effect of ligands

on the films AFM imaging would also show if the ligands are disrupting the membrane surface or altering the angle of the channel top with respect to the membrane surface.

While one of the main advantages of oCD is the reduced sample requirements and lack of isotropic labelling compared to solid state NMR, however NMR could still help characterise films of unlabelled samples. The line width of one dimensional  $^{31}\text{P}$  NMR is indicative of the ordering of phospholipid head groups, so it can be used to estimate the ordering of the lipid bilayer within the protein-lipid films (*Muhle-Goll et al., 2012*). In addition to screening conditions this would work as a control to see the effects of possible ligands on the ordering of lipids within the bilayers.

In order to produce a quantitative analysis of these spectra, new reference spectra for  $\alpha$ -helices based on the CD spectra of  $\alpha$ -helical membrane proteins of known structure was required. Fitting of these spectra to the negative peaks of the experimental data produced ranges of angles in agreement with the parameters calculated using AnglerFish. While this reference data fits well to the negative peaks of the experimental spectra presented here, it is far from conclusive. Like previous attempts to produce oriented reference spectra, it was based on spectra of proteins in solution. This leaves the fundamental problem of assigning directionality to isotropic spectra, this is most evident in the solution 222 nm peak which is formed from components both parallel and perpendicular to the beam. The directional components are assigned to this by the constraint that the parallel component is of the higher wavelength but there are many combinations of peak parameters that could sum to the isotropic spectra. In order allow a quantitative analysis of the tilt angles of oCD spectra reference data based on oriented spectra will be required. This will require independent methods to assay the tilt within bilayers. The gold standard for this would be to create a reference set of oCD spectra from films which have had their orientation solved by solid state NMR. This would allow the analysis of oCD spectra in a similar manner to estimating secondary structure from solution CD spectra by selecting a reference set and algorithm for angle determination.

# Appendices



```

AGATCTCGATCCCGCGAAATTAATACGACTCACTATAGGGGAATTGTGAGCGGATAACAATTCCCTCTAG
AAATAATTTTGTTTAACTTTAAGAAGGAGATATACCATGGGCAGCAGCCATCATCATCATCACAGCAG
CGGCCTGGTGCCGCGCGGCAGCCATATGCTCGAGGATCCGGCTGCTAACAAGCCCCGAAAGGAAGCTGA
GTTGGCTGCTGCCACCGCTGAGCAATAACTAGCATAACCCCTTGGGGCCTCTAAACGGGTCTTGAGGGGT
    
```

**Appendix 1. Plasmid map of pET-15b.** The multiple cloning site DNA sequence is shown below with the T7 promoter shown in dark green, the Lac operator in brown, the T7 terminator in dark red, the NdeI restriction site in green, the BamHI, and the thrombin cleavage site bold underlined. The above image was generated using the plamapper webserver

Na<sub>v</sub>Ms Full length:

Atgggcagcagccatcatcatcatcatcacagcagcggcctggtgccgcgcggcagc **catatg**tcacgcaaa  
atccgcgatttaatcgaatccaaacgctttcaaaacgcatcacccgcattattgtgctcaatggcgctgtg  
ctgggtctgctgaccgatacaaccctgtcggcctccagccaaaacctgctggagcgtgtggatcaactttgt  
ctgactatctttattgttgaaatctccctgaaaatctacgcctatggcgtgcgcggctttttccgcagcggc  
tggaatctgtttgattttgtgattgtggccatcgcgcttatgccggcccagggtagcctgtcgggtgctgctg  
acctccgtatcttccgcgtcatgcgcctcgtatcggatcatccaacctgcccgtgtggtgcaaggcatg  
ctcttggcactgccggcgctgggctcggtagcggcactggtgacgggtggtcttctatattgcggctgtcatg  
gccaccaatctctacggggcaaccttccctgaatggtttggtgatcttagcaagagcctgtacacactgttt  
caggtgatgaccttagagtcattggtctatgggcattgtgctccagtgatgaacggttcatccgaacgcattg  
gtttttttcatcccgttcatcatgctcaccacctttaccgtgctcaacctgtttattggcattattgtagat  
gcaatggcaatcaccaaggaacaggaggaagaggccaaaaccggtcaccatcaagaacctattttctcaaact  
cttcttcatcttgggtgatcgtcttgatcgtattgaaaaacaacttgctcaaaaataatgaacttcttcaacgt  
caacaacctcaaaaaaaaa **taa**taaggatcc

Na<sub>v</sub>Ms Pore:

Atgggcagcagccatcatcatcatcatcacagcagcggcctggtgccgcgcggcagc **catatg**gtgggctcg  
gtagcggcactggtgacgggtggtcttctatattgcggctgtcatggccaccaatctctacggggcaaccttc  
cctgaatggtttggtgatcttagcaagagcctgtacacactgtttcaggtgatgaccttagagtcattggtct  
atggggattgtgctccagtgatgaacggttcatccgaacgcattgggtttttttcatcccggttcatcatgctc  
accacctttaccgtgctcaacctgtttattggcattattgtagatgcaatggcaatcaccaaggaacaggag  
gaagaggccaaaaccggacaccatcaagaacctattttctcaaactcttcttcatcttgggtgatcgtcttgat  
cgtattgaaaaacaacttgctcaaaaataatgaacttcttcaacgtcaacaacctcaaaaaaaaa **taa**taagga  
tcc

Na<sub>v</sub>Ms Pore only:

Atgggcagcagccatcatcatcatcatcacagcagcggcctggtgccgcgcggcagc **catatg**gtgggctcg  
gtagcggcactggtgacgggtggtcttctatattgcggctgtcatggccaccaatctctacggggcaaccttc  
cctgaatggtttggtgatcttagcaagagcctgtacacactgtttcaggtgatgaccttagagtcattggtct  
atggggattgtgctccagtgatgaacggttcatccgaacgcattgggtttttttcatcccggttcatcatgctc  
accacctttaccgtgctcaacctgtttattggcattattgtagatgcaatggcaatcaccaaggaacaggag  
gaagaggccaaaaccggacaccat **taaggatcc**

**Appendix 2. NaVMs gene sequences.** The start codon is highlighted in yellow, the stop codon in red, Nde I restriction site in green and the Bam HI restriction site in grey.

Na<sub>v</sub>Ms full length:

MGSSHHHHHSSGLVPRGSH**M**SRKIRD LIESKR FQNVITAIIVLNGAVLGLL  
TDTTLSASSQNLLERVDQLCLTIFIVEISLKIYAYGVRGFFRSGWNLFDFVI  
VAIALMPAQGSLSVLRTFRIFRVMRLVSVIPTMRRVVQGMLLALPG**V**GSVAA  
LLTVVFYIAAVMATNLYGATFPEWFGDLSKSLYTLFQVMTLESWSMGIVRPV  
MNVHPNAWVFFIPFIMLTFTVNLNFIGIIVD**A**MAITKEQEEEEAKTGHHQEP  
ISQTLHLGDRLDRIEKQLAQNNELLQRQQPQKK

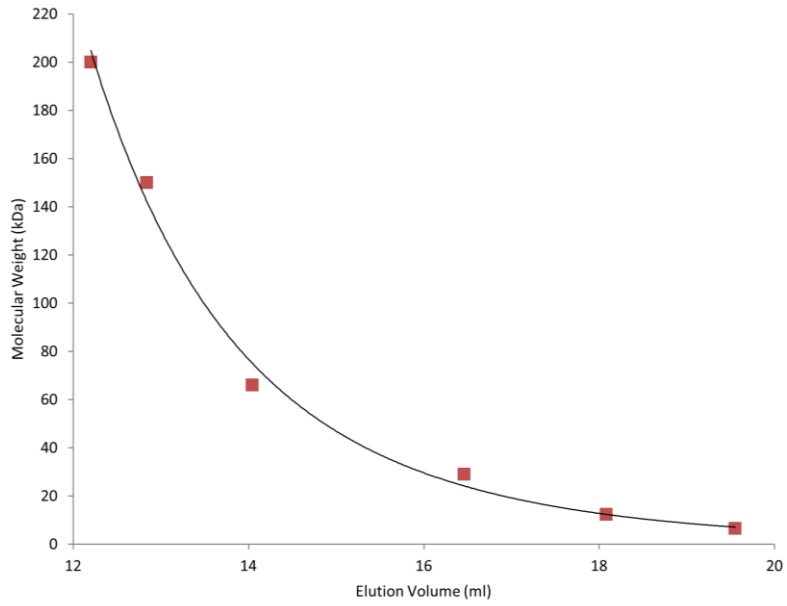
Na<sub>v</sub>Ms pore:

MGSSHHHHHSSGLVPRGSH**V**GSVAALLTVVFYIAAVMATNLYGATFPEWF  
GDLSKSLYTLFQVMTLESWSMGIVRPVMNVHPNAWVFFIPFIMLTFTVNLN  
FIGIIVD**A**MAITKEQEEEEAKTGHHQEPISQTLHLGDRLDRIEKQLAQNNEL  
LQRQQPQKK

Na<sub>v</sub>Ms pore only:

MGSSHHHHHSSGLVPRGSH**V**GSVAALLTVVFYIAAVMATNLYGATFPEWF  
GDLSKSLYTLFQVMTLESWSMGIVRPVMNVHPNAWVFFIPFIMLTFTVNLN  
FIGIIVDAMAITKEQEEEEAKTGHH

**Appendix 3. Na<sub>v</sub>Ms constructs protein sequences.** *The underlined sequence is removed by thrombin cleavage, the first amino acid of the Magnetococcus Mariunus gene highlighted in blue, the first Na<sub>v</sub>Ms amino acid of the pore construct in green and the alanine mutated to cysteine for labelling in yellow*



**Appendix 3. Size exclusion chromatography standards.** *The molecular weights of the proteins:  $\beta$ -amylase, Cytochrome C, Alcohol Dehydrogenase, Bovine Serum Albumin, Carbonic Anhydrase and Aprotinin are plotted against their elution volumes for the size exclusion column used to purify Na<sub>v</sub>Ms. A logarithmic trend line of:*

$$y = -390.17 * \ln(x) + 1141.17$$

*is included.*

		Peak 1			Peak 2			Peak 3			Peak 3 / Peak 2
file	Condition	Magnitude (mdeg)	$\lambda$ (nm)	Bandwidth (nm)	Magnitude (mdeg)	$\lambda$ (nm)	Bandwidth (nm)	Magnitude (mdeg)	$\lambda$ (nm)	Bandwidth (nm)	Magnitude
a49358	A5BBZ	15.31	197.49	6.71	-2.81	208.53	9.32	-7.09	227.42	10.80	2.52
a49367	A5BBZ	10.79	197.03	6.84	-2.36	208.21	8.17	-6.03	226.96	10.64	2.56
a50074	A5BBZ	13.60	197.17	6.25	-2.05	210.40	6.37	-6.14	227.20	10.81	3.00
a50092	A5BBZ	16.62	196.92	6.50	-2.50	209.20	7.86	-6.64	226.98	10.55	2.66
a50101	A5BBZ	14.68	196.96	6.16	-1.78	210.60	5.97	-5.44	227.16	10.58	3.06
a47908	Apo	10.29	199.21	5.33	-4.48	210.50	4.80	-19.52	228.40	13.33	4.36
a49285	Apo	14.15	197.00	7.00	-3.07	207.36	9.35	-6.29	226.80	11.06	2.05
a49294	Apo	16.56	197.44	6.60	-2.95	209.10	7.63	-9.42	227.53	10.77	3.20
a49303	Apo	26.76	197.68	6.07	-3.42	210.57	5.94	-11.55	227.84	10.81	3.38
a49312	Apo	18.26	196.98	6.17	-2.11	210.24	5.80	-7.47	227.39	10.56	3.54
a50002	Apo	17.24	197.13	6.56	-2.51	209.14	7.41	-7.69	227.42	10.45	3.06
a50020	Apo	28.56	197.09	6.28	-3.58	209.83	6.69	-10.80	227.13	10.82	3.02
a50029	Apo	33.53	197.18	6.01	-3.76	210.48	5.11	-12.72	227.46	10.67	3.38
a49473	Benzocaine	21.58	197.47	6.49	-3.31	209.06	8.06	-9.12	227.34	10.83	2.75
a49482	Benzocaine	15.24	197.02	6.12	-3.39	213.26	0.17	-7.30	225.64	13.48	2.15
a53249	Benzocaine	16.77	197.69	8.07	-4.92	206.30	8.48	-9.12	226.91	10.39	1.85
a53258	Benzocaine	16.72	197.73	8.00	-4.64	205.80	8.51	-8.65	227.10	10.53	1.86
a53267	Benzocaine	10.74	197.48	6.86	-2.53	208.17	7.45	-6.97	226.72	11.61	2.75
a53276	Benzocaine	15.43	197.70	8.16	-4.86	205.68	8.22	-7.67	226.66	10.75	1.58
a49437	Lidocaine	15.37	197.40	7.24	-4.24	206.49	9.47	-7.95	226.67	11.16	1.88
a49446	Lidocaine	13.01	197.76	8.48	-5.54	206.43	8.04	-9.11	226.11	11.91	1.64
a50038	Lidocaine	17.67	196.89	6.33	-2.49	209.89	6.58	-6.96	226.97	10.75	2.80
a50047	Lidocaine	22.39	196.94	6.22	-3.08	210.12	6.26	-8.59	226.94	10.92	2.79
a50056	Lidocaine	24.51	197.10	6.04	-3.13	210.40	5.50	-9.54	227.09	10.89	3.05
a53186	Lidocaine	6.72	197.86	12.81	-3.77	207.06	9.49	-2.78	224.05	10.57	0.74
a53195	Lidocaine	7.05	196.12	11.96	-2.89	207.39	7.58	-4.31	223.22	12.55	1.49
a53204	Lidocaine	5.97	196.53	11.23	-1.79	208.39	6.26	-4.88	223.62	13.40	2.72
a49455	Mibifradil	21.87	197.08	6.08	-2.04	210.15	5.79	-7.03	227.24	10.84	3.44
a49464	Mibifradil	28.49	198.03	6.60	-4.81	206.84	8.92	-11.85	227.96	10.63	2.47
a49383	Tamoxifen	22.66	196.74	6.71	-4.01	208.85	7.80	-10.28	226.77	10.75	2.56
a49392	Tamoxifen	8.26	197.28	6.70	-1.85	208.88	7.30	-5.25	226.63	11.66	2.84
a53294	Tamoxifen	10.57	197.74	7.07	-1.93	206.99	9.89	-5.10	227.10	10.44	2.64
a53303	Tamoxifen	12.18	198.06	7.72	-2.79	205.70	9.72	-5.00	227.21	10.49	1.79
a53312	Tamoxifen	10.78	197.62	7.89	-3.15	205.30	8.72	-5.19	226.35	11.26	1.65
a53321	Tamoxifen	13.04	198.12	7.70	-3.22	205.28	8.68	-5.15	226.94	10.72	1.60
a49322	Veratridine	8.67	196.98	7.56	-2.73	204.89	9.35	-4.16	226.16	11.48	1.52
a49331	Veratridine	18.46	197.12	7.55	-6.01	206.71	9.02	-11.32	226.48	11.09	1.88
a49340	Veratridine	12.59	196.81	7.47	-3.49	205.84	9.33	-6.07	226.37	11.10	1.74
a49349	Veratridine	15.11	197.49	7.65	-4.57	206.25	8.78	-7.54	226.27	11.46	1.65

**Appendix 5. Peak parameters for oCD ligand binding experiments.** Peaks were fit simultaneously by nonlinear fitting from the curve fit function of the scipy python package.

# Bibliography

---

- [1] A. M. Whited and P. S.-H. Park, "Atomic force microscopy: A multifaceted tool to study membrane proteins and their interactions with ligands," *Biochim. Biophys. Acta - Biomembr.*, vol. 1838, no. 1, pp. 56–68, Jan. 2014.
- [2] A. Niitsu, J. W. Heal, K. Fauland, A. R. Thomson, and D. N. Woolfson, "Membrane-spanning  $\alpha$ -helical barrels as tractable protein-design targets.," *Philos. Trans. R. Soc. Lond. B. Biol. Sci.*, vol. 372, no. 1726, p. 20160213, Aug. 2017.
- [3] S. Wang, R. Vafabakhsh, W. F. Borschel, T. Ha, and C. G. Nichols, "Structural dynamics of potassium-channel gating revealed by single-molecule FRET.," *Nat. Struct. Mol. Biol.*, vol. 23, no. 1, pp. 31–36, Jan. 2016.
- [4] B. A. Wallace, "Structure of gramicidin A.," *Biophys. J.*, vol. 49, no. 1, pp. 295–306, Jan. 1986.
- [5] D. N. Woolfson, "Coiled-Coil Design: Updated and Upgraded," in *Sub-cellular biochemistry*, vol. 82, 2017, pp. 35–61.
- [6] G. Weber, "Dependence of the polarization of the fluorescence on the concentration," *Trans. Faraday Soc.*, vol. 50, no. 0, p. 552, Jan. 1954.
- [7] P. I. Bastiaens, A. van Hoek, J. A. Benen, J. C. Brochon, and A. J. Visser, "Conformational dynamics and intersubunit energy transfer in wild-type and mutant lipoamide dehydrogenase from *Azotobacter vinelandii*. A multidimensional time-resolved polarized fluorescence study," *Biophys. J.*, vol. 63, no. 3, pp. 839–853, Sep. 1992.
- [8] F. D. Stefani, J. P. Hoogenboom, and E. Barkai, "Beyond quantum jumps: Blinking nanoscale light emitters," *Phys. Today*, vol. 62, no. 2, pp. 34–39, Feb. 2009.
- [9] L. Zubcevic, M. A. Herzik, B. C. Chung, Z. Liu, G. C. Lander, and S.-Y. Lee, "Cryo-electron microscopy structure of the TRPV2 ion channel," *Nat. Struct. Mol. Biol.*, vol. 23, no. 2, pp. 180–186, Feb. 2016.
- [10] W. Huang, M. Liu, S. F. Yan, and N. Yan, "Structure-based assessment of disease-related mutations in human voltage-gated sodium channels.," *Protein Cell*, vol. 8, no. 6, pp. 401–438, Jun. 2017.
- [11] J.-B. Kim, "Channelopathies," *Korean J. Pediatr.*, vol. 57, no. 1, p. 1, Jan. 2014.
- [12] O. V. Nolandt, T. H. Walther, S. Roth, J. Bürck, and A. S. Ulrich, "Structure analysis of the membrane protein TatCd from the Tat system of *B. subtilis* by circular dichroism," *Biochim. Biophys. Acta - Biomembr.*, vol. 1788, no. 10, pp. 2238–2244, Oct. 2009.
- [13] A. J. Miles, B. A. Wallace, and M. Esmann, "Correlation of structural and functional thermal stability of the integral membrane protein Na,K-ATPase," *Biochim. Biophys. Acta - Biomembr.*, vol. 1808, no. 10, pp. 2573–2580, Oct. 2011.
- [14] L. Zheng and J. D. Brennan, "Measurement of intrinsic fluorescence to probe the conformational flexibility and thermodynamic stability of a single tryptophan protein entrapped in a sol-gel derived glass matrix," *Analyst*, vol. 123, no. 8, pp. 1735–1744, Jan. 1998.

- [15] L. Reinhard, H. Mayerhofer, A. Geerlof, J. Mueller-Dieckmann, and M. S. Weiss, "Optimization of protein buffer cocktails using Thermofluor.," *Acta Crystallogr. Sect. F. Struct. Biol. Cryst. Commun.*, vol. 69, no. Pt 2, pp. 209–14, Feb. 2013.
- [16] A. I. Alexandrov, M. Mileni, E. Y. T. Chien, M. A. Hanson, and R. C. Stevens, "Microscale Fluorescent Thermal Stability Assay for Membrane Proteins," *Structure*, vol. 16, no. 3, pp. 351–359, Mar. 2008.
- [17] L. Boscá and F. Morán, "Circular dichroism analysis of ligand-induced conformational changes in protein kinase C. Mechanism of translocation of the enzyme from the cytosol to the membranes and its implications," *Biochem. J.*, vol. 290, no. 3, pp. 827–832, Mar. 1993.
- [18] S. M. Ireland, A. Sula, and B. A. Wallace, "Thermal melt circular dichroism spectroscopic studies for identifying stabilising amphipathic molecules for the voltage-gated sodium channel NavMs," *Biopolymers*, p. e23067, Sep. 2017.
- [19] N.-C. Chia and R. Mendelsohn, "Conformational disorder in unsaturated phospholipids by FTIR spectroscopy," *Biochim. Biophys. Acta - Biomembr.*, vol. 1283, no. 2, pp. 141–150, Sep. 1996.
- [20] W. Guo, V. Kurze, T. Huber, N. H. Afdhal, K. Beyer, and J. A. Hamilton, "A solid-state NMR study of phospholipid-cholesterol interactions: sphingomyelin-cholesterol binary systems.," *Biophys. J.*, vol. 83, no. 3, pp. 1465–78, Sep. 2002.
- [21] J. Karolin, M. Fa, M. Wilczynska, T. Ny, and L. B. Johansson, "Donor-donor energy migration for determining intramolecular distances in proteins: I. Application of a model to the latent plasminogen activator inhibitor-1 (PAI-1).," *Biophys. J.*, vol. 74, no. 1, pp. 11–21, Jan. 1998.
- [22] Y. Santoso, C. M. Joyce, O. Potapova, L. Le Reste, J. Hohlbein, J. P. Torella, N. D. F. Grindley, and A. N. Kapanidis, "Conformational transitions in DNA polymerase I revealed by single-molecule FRET.," *Proc. Natl. Acad. Sci. U. S. A.*, vol. 107, no. 2, pp. 715–20, Jan. 2010.
- [23] E. E. Sadler, A. N. Kapanidis, and S. J. Tucker, "Solution-Based Single-Molecule FRET Studies of K(+) Channel Gating in a Lipid Bilayer.," *Biophys. J.*, vol. 110, no. 12, pp. 2663–2670, Jun. 2016.
- [24] B. Corry, A. C. Hurst, P. Pal, T. Nomura, P. Rigby, and B. Martinac, "An improved open-channel structure of MscL determined from FRET confocal microscopy and simulation," *J. Gen. Physiol.*, vol. 136, no. 4, pp. 483–494, Oct. 2010.
- [25] B. Corry, P. Rigby, Z.-W. Liu, and B. Martinac, "Conformational changes involved in MscL channel gating measured using FRET spectroscopy," *Biophys. J.*, vol. 89, no. 6, pp. L49-51, Dec. 2005.
- [26] J. Spillane, D. M. Kullmann, and M. G. Hanna, "Genetic neurological channelopathies: molecular genetics and clinical phenotypes.," *J. Neurol. Neurosurg. Psychiatry*, vol. 87, no. 1, pp. 37–48, Jan. 2016.
- [27] J.-B. Kim, "Channelopathies.," *Korean J. Pediatr.*, vol. 57, no. 1, pp. 1–18, Jan. 2014.
- [28] Y. Wang, Y. Liu, H. A. DeBerg, T. Nomura, M. T. Hoffman, P. R. Rohde, K. Schulten, B. Martinac, and P. R. Selvin, "Single molecule FRET reveals pore size and opening mechanism of a mechano-sensitive ion channel," *Elife*, vol. 3, p. e01834, Feb. 2014.
- [29] D. K. Sasmal and H. P. Lu, "Single-Molecule Patch-Clamp FRET Microscopy Studies of NMDA Receptor Ion Channel Dynamics in Living Cells: Revealing the Multiple Conformational States Associated with a Channel at Its Electrical Off State," *J. Am. Chem. Soc.*, vol. 136, no. 37, pp. 12998–13005, Sep. 2014.

- [30] A. Rath, M. Glibowicka, V. G. Nadeau, G. Chen, and C. M. Deber, “Detergent binding explains anomalous SDS-PAGE migration of membrane proteins,” *Proc. Natl. Acad. Sci. U. S. A.*, vol. 106, no. 6, pp. 1760–5, Feb. 2009.
- [31] H. Rogl, K. Kosemund, W. Kühlbrandt, and I. Collinson, “Refolding of Escherichia coli produced membrane protein inclusion bodies immobilised by nickel chelating chromatography,” *FEBS Lett.*, vol. 432, no. 1–2, pp. 21–6, Jul. 1998.
- [32] M. N. Kinde, V. Bondarenko, D. Granata, W. Bu, K. C. Grasty, P. J. Loll, V. Carnevale, M. L. Klein, R. G. Eckenhoff, P. Tang, and Y. Xu, “Fluorine-19 NMR and computational quantification of isoflurane binding to the voltage-gated sodium channel NaChBac,” *Proc. Natl. Acad. Sci. U. S. A.*, vol. 113, no. 48, pp. 13762–13767, Nov. 2016.
- [33] A. F. Barber, V. Carnevale, M. L. Klein, R. G. Eckenhoff, and M. Covarrubias, “Modulation of a voltage-gated Na<sup>+</sup> channel by sevoflurane involves multiple sites and distinct mechanisms,” *Proc. Natl. Acad. Sci. U. S. A.*, vol. 111, no. 18, pp. 6726–31, May 2014.
- [34] S. G. Raju, A. F. Barber, D. N. LeBard, M. L. Klein, and V. Carnevale, “Exploring Volatile General Anesthetic Binding to a Closed Membrane-Bound Bacterial Voltage-Gated Sodium Channel via Computation,” *PLoS Comput. Biol.*, vol. 9, no. 6, p. e1003090, Jun. 2013.
- [35] K. F. Herold and H. C. Hemmings, “Sodium channels as targets for volatile anesthetics,” *Front. Pharmacol.*, vol. 3, p. 50, 2012.
- [36] C. Penny, “The Molecular Physiology of Two-pore Channels,” UCL (University College London), 2016.
- [37] W. Moffitt, D. D. Fitts, and J. G. Kirkwood, “CRITIQUE OF THE THEORY OF OPTICAL ACTIVITY OF HELICAL POLYMERS,” *Proc. Natl. Acad. Sci. U. S. A.*, vol. 43, no. 8, pp. 723–30, Aug. 1957.
- [38] M. A. Andrade, P. Chacón, J. J. Merelo, and F. Morán, “Evaluation of secondary structure of proteins from UV circular dichroism spectra using an unsupervised learning neural network,” *Protein Eng.*, vol. 6, no. 4, pp. 383–90, Jun. 1993.
- [39] B. A. Wallace and R. W. Janes, “An Introduction to Circular Dichroism and Synchrotron Radiation Circular Dichroism Spectroscopy,” in *Modern Techniques for Circular Dichroism and Synchrotron Radiation Circular Dichroism Spectroscopy*, IOS Press, 2009, pp. 1–18.
- [40] S. W. Provencher and J. Glöckner, “Estimation of globular protein secondary structure from circular dichroism,” *Biochemistry*, vol. 20, no. 1, pp. 33–7, Jan. 1981.
- [41] B. T. Arachea, Z. Sun, N. Potente, R. Malik, D. Isailovic, and R. E. Viola, “Detergent selection for enhanced extraction of membrane proteins,” *Protein Expr. Purif.*, vol. 86, no. 1, pp. 12–20, 2012.
- [42] M. J. Lenaeus, T. M. Gamal El-Din, C. Ing, K. Ramanadane, R. Pomès, N. Zheng, and W. A. Catterall, “Structures of closed and open states of a voltage-gated sodium channel,” *Proc. Natl. Acad. Sci. U. S. A.*, vol. 114, no. 15, pp. E3051–E3060, Apr. 2017.
- [43] Y. Xiao, K. Blumenthal, J. O. Jackson, S. Liang, and T. R. Cummins, “The tarantula toxins ProTx-II and huwentoxin-IV differentially interact with human Nav1.7 voltage sensors to inhibit channel activation and inactivation,” *Mol. Pharmacol.*, vol. 78, no. 6, pp. 1124–1134, 2010.
- [44] G. M. Lipkind and H. A. Fozzard, “A structural model of the tetrodotoxin and saxitoxin binding site of the sodium channel,” *Biophys. J.*, vol. 66, pp. 1–12, 1994.

- [45] D. A. Hanck, E. Nikitina, M. M. McNulty, H. A. Fozzard, G. M. Lipkind, and M. F. Sheets, "Using lidocaine and benzocaine to link sodium channel molecular conformations to state-dependent antiarrhythmic drug affinity," *Circ. Res.*, vol. 105, no. 5, pp. 492–499, 2009.
- [46] R. Blunck, J. F. Cordero-Morales, L. G. Cuello, E. Perozo, and F. Bezanilla, "Detection of the opening of the bundle crossing in KcsA with fluorescence lifetime spectroscopy reveals the existence of two gates for ion conduction," *J. Gen. Physiol.*, vol. 128, no. 5, pp. 569–581, 2006.
- [47] C. E. Naylor, C. Bagn ris, P. G. DeCaen, A. Sula, A. Scaglione, D. E. Clapham, and B. A. Wallace, "Molecular basis of ion permeability in a voltage-gated sodium channel.," *EMBO J.*, vol. 35, no. 8, pp. 820–830, 2016.
- [48] F. Tombola, M. M. Pathak, P. Gorostiza, and E. Y. Isacoff, "The twisted ion-permeation pathway of a resting voltage-sensing domain," *Nature*, 2007.
- [49] S. B. Long, X. Tao, E. B. Campbell, and R. MacKinnon, "Atomic structure of a voltage-dependent K<sup>+</sup> channel in a lipid membrane-like environment," *Nature*, 2007.
- [50] S. England and M. J. de Groot, "Subtype-selective targeting of voltage-gated sodium channels," *Br. J. Pharmacol.*, vol. 158, no. 6, pp. 1413–1425, Nov. 2009.
- [51] F. H. Yu, V. Yarov-Yarovoy, G. A. Gutman, and W. A. Catterall, "Overview of Molecular Relationships in the Voltage-Gated Ion Channel Superfamily," *Pharmacol. Rev.*, vol. 57, no. 4, pp. 387–395, Dec. 2005.
- [52] B. Hille, *Ion channels of excitable membranes*. 2001.
- [53] E. Sisamakias, A. Valeri, S. Kalinin, P. J. Rothwell, and C. A. M. Seidel, "Accurate Single-Molecule FRET Studies Using Multiparameter Fluorescence Detection," *Methods Enzymol.*, vol. 475, no. C, pp. 455–514, 2010.
- [54] C. Muhle-Goll, S. Hoffmann, S. Afonin, S. L. Grage, A. A. Polyansky, D. Windisch, M. Zeitler, J. B rck, and A. S. Ulrich, "Hydrophobic matching controls the tilt and stability of the dimeric platelet-derived growth factor receptor (PDGFR)  $\beta$  transmembrane segment.," *J. Biol. Chem.*, vol. 287, no. 31, pp. 26178–86, Jul. 2012.
- [55] W. Ouyang, T.-Y. Jih, T.-T. Zhang, A. M. Correa, and H. C. Hemmings, "Isoflurane Inhibits NaChBac, a Prokaryotic Voltage-Gated Sodium Channel," *J. Pharmacol. Exp. Ther.*, vol. 322, no. 3, pp. 1076–1083, Jun. 2007.
- [56] C. T. Chang, C.-S. C. Wu, and J. T. Yang, "Circular dichroic analysis of protein conformation: Inclusion of the  $\beta$ -turns," *Anal. Biochem.*, vol. 91, no. 1, pp. 13–31, Nov. 1978.
- [57] P. R. Selvin, "Fluorescence resonance energy transfer," *Methods Enzymol.*, vol. 246, no. C, pp. 300–334, 1995.
- [58] L. Stryer and R. P. Haugland, "Energy Transfer: A Spectroscopic Ruler," *Proc. Natl. Acad. Sci. U. S. A.*, vol. 58, pp. 719–726.
- [59] S. J. Holden, S. Uphoff, J. Hohlbein, D. Yadin, L. Le Reste, O. J. Britton, and A. N. Kapanidis, "Defining the Limits of Single-Molecule FRET Resolution in TIRF Microscopy," *Biophys. J.*, vol. 99, no. 9, pp. 3102–3111, Nov. 2010.
- [60] A. S. R. Periasamy, "Fluorescence resonance energy transfer (FRET) microscopy imaging of live cell protein localizations," *J. Cell Biol.*, vol. 160, no. 5, pp. 629–633, 2003.

- [61] A. M. Seddon, P. Curnow, and P. J. Booth, "Membrane proteins, lipids and detergents: not just a soap opera," *Biochim. Biophys. Acta - Biomembr.*, vol. 1666, no. 1, pp. 105–117, 2004.
- [62] B. Miroux and J. E. Walker, "Over-production of Proteins in *Escherichia coli*: Mutant Hosts that Allow Synthesis of some Membrane Proteins and Globular Proteins at High Levels," *J. Mol. Biol.*, vol. 260, no. 3, pp. 289–298, Jul. 1996.
- [63] S. Wagner, M. M. Klepsch, S. Schlegel, A. Appel, R. Draheim, M. Tarry, M. Högbom, K. J. van Wijk, D. J. Slotboom, J. O. Persson, and J.-W. de Gier, "Tuning *Escherichia coli* for membrane protein overexpression," *Proc. Natl. Acad. Sci. U. S. A.*, vol. 105, no. 38, pp. 14371–6, Sep. 2008.
- [64] S. Kalipatnapu and A. Chattopadhyay, "Membrane Protein Solubilization: Recent Advances and Challenges in Solubilization of Serotonin1A Receptors," *IUBMB Life (International Union Biochem. Mol. Biol. Life)*, vol. 57, no. 7, pp. 505–512, 2005.
- [65] P. N. Hengen, "Purification of His-Tag fusion proteins from *Escherichia coli*," *Trends Biochem Sci*, vol. 20, no. 7, pp. 285–286, 1995.
- [66] F. Gubellini, N. K. Karpowich, J. D. Luff, N. Gauthier, S. K. Handelman, S. E. Ades, and J. F. Hunt, "Physiological Response to Membrane Protein Overexpression in *E. coli*," *Mol. Cell.*, pp. 1–17, 2011.
- [67] N. D'Avanzo, E. C. McCusker, A. M. Powl, A. J. Miles, C. G. Nichols, and B. A. Wallace, "Differential Lipid Dependence of the Function of Bacterial Sodium Channels," *PLoS One*, vol. 8, no. 4, 2013.
- [68] H. G. Barth, C. Jackson, and B. E. Boyes, "Size exclusion chromatography," *Anal. Chem.*, vol. 66, no. 12, pp. 595–620, 1994.
- [69] R. Roy, S. Hohng, and T. Ha, "A practical guide to single-molecule FRET," *Nat. Methods*, vol. 5, no. 6, pp. 507–516, Jun. 2008.
- [70] S. Kalinin, T. Peulen, S. Sindbert, P. J. Rothwell, S. Berger, T. Restle, R. S. Goody, H. Gohlke, and C. A. M. Seidel, "A toolkit and benchmark study for FRET-restrained high-precision structural modeling," *Nat. Methods*, vol. 9, no. 12, pp. 1218–1225, Nov. 2012.
- [71] N. K. Lee, A. N. Kapanidis, Y. Wang, X. Michalet, J. Mukhopadhyay, R. H. Ebright, and S. Weiss, "Accurate FRET Measurements within Single Diffusing Biomolecules Using Alternating-Laser Excitation," *Biophys. J.*, vol. 88, no. 4, pp. 2939–2953, Apr. 2005.
- [72] A. N. Kapanidis, N. K. Lee, T. A. Laurence, S. Doose, E. Margeat, and S. Weiss, "Fluorescence-aided molecule sorting: Analysis of structure and interactions by alternating-laser excitation of single molecules," *Proc. Natl. Acad. Sci.*, vol. 101, no. 24, pp. 8936–8941, Jun. 2004.
- [73] B. A. Wallace, J. G. Lees, A. J. W. Orry, A. Lobley, and R. W. Janes, "Analyses of circular dichroism spectra of membrane proteins," *Protein Sci.*, vol. 12, no. 4, pp. 875–84, Apr. 2003.
- [74] N. Sreerama and R. W. Woody, "Estimation of Protein Secondary Structure from Circular Dichroism Spectra: Comparison of CONTIN, SELCON, and CDSSTR Methods with an Expanded Reference Set," *Anal. Biochem.*, vol. 287, no. 2, pp. 252–260, Dec. 2000.
- [75] P. Manavalan and W. C. Johnson, "Variable selection method improves the prediction of protein secondary structure from circular dichroism spectra," *Anal. Biochem.*, vol. 167, no. 1, pp. 76–85, Nov. 1987.
- [76] N. Sreerama and R. W. Woody, "A Self-Consistent Method for the Analysis of Protein Secondary Structure from Circular Dichroism," *Analytical biochemistry*, vol. 209, no. 1, pp. 32–44, 15-Feb-1993.

- [77] I. H. van Stokkum, H. J. Spoelder, M. Bloemendal, R. van Grondelle, and F. C. Groen, "Estimation of protein secondary structure and error analysis from circular dichroism spectra," *Anal. Biochem.*, vol. 191, no. 1, pp. 110–8, Nov. 1990.
- [78] W. Kabsch and C. Sander, "Dictionary of protein secondary structure: Pattern recognition of hydrogen-bonded and geometrical features," *Biopolymers*, vol. 22, no. 12, pp. 2577–2637, 1983.
- [79] D. H. Boxer, H. Zhang, D. G. Gourley, W. N. Hunter, S. M. Kelly, N. C. Price, Y. W. Ebricht, H. M. Berman, and R. H. Ebricht, "Sensing of remote oxyanion binding at the DNA binding domain of the molybdate-dependent transcriptional regulator, ModE," *Org. Biomol. Chem.*, vol. 2, no. 19, p. 2829, 2004.
- [80] A.-Y. M. Woody and R. W. Woody, "Individual tyrosine side-chain contributions to circular dichroism of ribonuclease," *Biopolymers*, vol. 72, no. 6, pp. 500–513, 2003.
- [81] S. M. Kelly, T. J. Jess, and N. C. Price, "How to study proteins by circular dichroism," *Biochimica et Biophysica Acta - Proteins and Proteomics*, vol. 1751, no. 2, pp. 119–139, 2005.
- [82] S. Craig, R. H. Pain, U. Schmeissner, R. Virden, and P. T. Wingfield, "Determination of the contributions of individual aromatic residues to the CD spectrum of IL-1 beta using site directed mutagenesis," *Int. J. Pept. Protein Res.*, vol. 33, no. 4, pp. 256–62, Apr. 1989.
- [83] A. Abdul-Gader, A. J. Miles, and B. A. Wallace, "A reference dataset for the analyses of membrane protein secondary structures and transmembrane residues using circular dichroism spectroscopy," *Bioinformatics*, vol. 27, no. 12, pp. 1630–1636, Jun. 2011.
- [84] J. Hohlbein, T. D. Craggs, and T. Cordes, "Alternating-laser excitation: single-molecule FRET and beyond," *Chem. Soc. Rev.*, vol. 43, no. 4, pp. 1156–1171, 2014.
- [85] J.-F. Desaphy, A. Dipalma, T. Costanza, C. Bruno, G. Lentini, C. Franchini, A. L. George, and D. Conte Camerino, "Molecular determinants of state-dependent block of voltage-gated sodium channels by pilsicainide," *Br. J. Pharmacol.*, vol. 160, no. 6, pp. 1521–1533, Jul. 2010.
- [86] C. Arrigoni, A. Rohaim, D. Shaya, F. Findeisen, R. A. Stein, S. R. Nurva, S. Mishra, H. S. Mchaourab, and D. L. Minor, "Unfolding of a Temperature-Sensitive Domain Controls Voltage-Gated Channel Activation," *Cell*, vol. 164, no. 5, pp. 922–36, Feb. 2016.
- [87] F. D. Rinkevich, Y. Du, and K. Dong, "Diversity and convergence of sodium channel mutations involved in resistance to pyrethroids," *Pestic. Biochem. Physiol.*, vol. 106, no. 3, pp. 93–100, Jul. 2013.
- [88] A. O. O'Reilly, B. P. S. Khambay, M. S. Williamson, L. M. Field, B. A. Wallace, and T. G. E. Davies, "Modelling insecticide-binding sites in the voltage-gated sodium channel," *Biochem. J.*, vol. 396, no. 2, pp. 255–263, Jun. 2006.
- [89] L. M. Field, T. G. Emyr Davies, A. O. O'Reilly, M. S. Williamson, and B. A. Wallace, "Voltage-gated sodium channels as targets for pyrethroid insecticides," *European Biophysics Journal*, Springer Berlin Heidelberg, pp. 1–5, 09-Jan-2017.
- [90] C. Bagn eris, C. E. Naylor, E. C. McCusker, and B. A. Wallace, "Structural model of the open–closed–inactivated cycle of prokaryotic voltage-gated sodium channels," *J. Gen. Physiol.*, vol. 145, pp. 5–16, 2014.
- [91] M. B. Ulmschneider, C. Bagn eris, E. C. McCusker, P. G. Decaen, M. Delling, D. E. Clapham, J. P. Ulmschneider, and B. A. Wallace, "Molecular dynamics of ion transport through the open conformation of a bacterial voltage-gated sodium channel," *Proc. Natl. Acad. Sci. U. S. A.*, vol. 110, no. 16, pp. 6364–9, Apr. 2013.

- [92] C. E. Naylor, C. Bagn ris, P. G. DeCaen, D. E. Clapham, and B. A. Wallace, “Sodium Ion Coordination in the Selectivity Filter of a Voltage-Gated Sodium Channel,” *Biophys. J.*, vol. 108, no. 2, p. 490a, Jan. 2015.
- [93] A. Sula, J. Booker, L. C. T. Ng, C. E. Naylor, P. G. DeCaen, and B. A. Wallace, “The complete structure of an activated open sodium channel,” *Nat. Commun.*, vol. 8, p. 14205, Feb. 2017.
- [94] S. Ahuja, S. Mukund, L. Deng, K. Khakh, E. Chang, H. Ho, S. Shriver, C. Young, S. Lin, J. P. Johnson, P. Wu, J. Li, M. Coons, C. Tam, B. Brillantes, H. Sampang, K. Mortara, K. K. Bowman, K. R. Clark, A. Estevez, Z. Xie, H. Verschoof, M. Grimwood, C. Dehnhardt, J.-C. Andrez, T. Focken, D. P. Sutherlin, B. S. Safina, M. A. Starovasnik, D. F. Ortwine, Y. Franke, C. J. Cohen, D. H. Hackos, C. M. Koth, and J. Payandeh, “Structural basis of Nav1.7 inhibition by an isoform-selective small-molecule antagonist,” *Science (80-. )*, vol. 350, no. 6267, p. aac5464, Dec. 2015.
- [95] S. K. Bagal, B. E. Marron, R. M. Owen, R. I. Storer, and N. A. Swain, “Voltage gated sodium channels as drug discovery targets,” *Channels*, vol. 9, no. 6, pp. 360–366, Nov. 2015.
- [96] A. J. Miles and B. A. Wallace, “Circular dichroism spectroscopy of membrane proteins,” *Chem. Soc. Rev.*, vol. 45, no. 18, pp. 4859–4872, 2016.
- [97] T. Zimmer and R. Surber, “SCN5A channelopathies - An update on mutations and mechanisms,” *Progress in Biophysics and Molecular Biology*, vol. 98, no. 2–3, pp. 120–136, 2008.
- [98] Y. Zhao, V. Yarov-Yarovoy, T. Scheuer, and W. A. Catterall, “A Gating Hinge in Na<sup>+</sup> Channels,” *Neuron*, vol. 41, no. 6, pp. 859–865, 2004.
- [99] Y. Zhao, T. Scheuer, and W. A. Catterall, “Reversed voltage-dependent gating of a bacterial sodium channel with proline substitutions in the S6 transmembrane segment,” *Proc. Natl. Acad. Sci. U. S. A.*, vol. 101, no. 51, pp. 17873–8, 2004.
- [100] L. Yue, B. Navarro, D. Ren, A. Ramos, and D. E. Clapham, “The cation selectivity filter of the bacterial sodium channel, NaChBac,” *J. Gen. Physiol.*, vol. 120, no. 6, pp. 845–53, 2002.
- [101] F. H. Yu, M. Mantegazza, R. E. Westenbroek, C. A. Robbins, F. Kalume, K. A. Burton, W. J. Spain, G. S. McKnight, T. Scheuer, and W. A. Catterall, “Reduced sodium current in GABAergic interneurons in a mouse model of severe myoclonic epilepsy in infancy,” *Nat. Neurosci.*, vol. 9, no. 9, pp. 1142–1149, 2006.
- [102] N. Yang and R. Horn, “Evidence for Voltage-Dependent in Sodium Channels S4 Movement,” *Neuron*, vol. 15, pp. 213–218, 1995.
- [103] N. Yang, A. L. George, R. Horn, E. Y. Isacoff, J. B. Findlay, O. Pongs, J. O. Dolly, R. MacKinnon, and A. Ferrus, “Molecular Basis of Charge Movement in Voltage-Gated Sodium Channels,” *Neuron*, vol. 16, no. 1, pp. 113–122, 1996.
- [104] W. Xiong, Y. Z. Farukhi, Y. Tian, D. DiSilvestre, R. A. Li, and G. F. Tomaselli, “A conserved ring of charge in mammalian Na<sup>+</sup> channels: a molecular regulator of the outer pore conformation during slow inactivation,” *J. Physiol.*, vol. 576, no. 3, pp. 739–754, 2006.
- [105] X. S. Wu, H. D. Edwards, and W. A. Sather, “Side chain orientation in the selectivity filter of a voltage-gated Ca<sup>2+</sup> channel,” *J. Biol. Chem.*, vol. 275, no. 0021–9258 SB–M SB–X, pp. 31778–31785, 2000.
- [106] P. T., “Voltage-gated sodium channels and pain,” *Current Drug Targets: CNS and Neurological Disorders*, vol. 3, no. 6, pp. 441–456, 2004.

- [107] J. W. West, D. E. Patton, T. Scheuer, Y. Wang, A. L. Goldin, and W. A. Catterall, "A cluster of hydrophobic amino acid residues required for fast Na(+)-channel inactivation.," *Proc. Natl. Acad. Sci. U. S. A.*, vol. 89, no. 22, pp. 10910–4, 1992.
- [108] E. Vargas, V. Yarov-Yarovoy, F. Khalili-Araghi, W. A. Catterall, M. L. Klein, M. Tarek, E. Lindahl, K. Schulten, E. Perozo, F. Bezanilla, and B. Roux, "An emerging consensus on voltage-dependent gating from computational modeling and molecular dynamics simulations," *J. Gen. Physiol.*, vol. 140, no. 6, pp. 587–594, 2012.
- [109] S. Uysal, V. Tereshko, K. Esaki, F. A. Fellouse, S. S. Sidhu, S. Koide, E. Perozo, and A. Kossiakoff, "Crystal structure of full-length KcsA in its closed conformation," *Proc. Natl. Acad. Sci.*, vol. 106, pp. 6644–6649, 2009.
- [110] C. Townsend and R. Horn, "Effect of alkali metal cations on slow inactivation of cardiac Na<sup>+</sup> channels," *J. Gen. Physiol.*, vol. 110, no. July, pp. 23–33, 1997.
- [111] F. Tombola and E. Y. Isacoff, "How far will you go to collect biomass?," *Neuron*, vol. 48, pp. 719–725, 2005.
- [112] A. Toib, V. Lyakhov, and S. Marom, "Interaction between duration of activity and time course of recovery from slow inactivation in mammalian brain Na<sup>+</sup> channels.," *J. Neurosci.*, vol. 18, no. 5, pp. 1893–903, 1998.
- [113] S. K. Tiwari-Woodruff, "Voltage-dependent Structural Interactions in the Shaker K<sup>+</sup> Channel," *J. Gen. Physiol.*, vol. 115, no. 2, pp. 123–138, 2000.
- [114] X. Tao, W. Limapichat, D. A. Dougherty, and R. MacKinnon, "A gating charge transfer center in voltage sensors," *Science (80-. )*, vol. 328, pp. 67–73, 2010.
- [115] Y. Shafirir, S. R. Durell, and H. R. Guy, "Models of Voltage-Dependent Conformational Changes in NaChBac Channels," *Biophys. J.*, vol. 95, no. 8, pp. 3663–3676, 2008.
- [116] C. Sato, K. Asai, K. Takahashi, M. Sato, A. Engel, and Y. Fujiyoshi, "The voltage-sensitive sodium channel is a bell-shaped molecule with several cavities," *Nature*, vol. 409, pp. 1047–1051, 2001.
- [117] C. A. Rohl, F. A. Boeckman, C. Baker, T. Scheuer, W. A. Catterall, and R. E. Klevit, "Solution structure of the sodium channel inactivation gate.," *Biochemistry*, vol. 38, no. 3, pp. 855–861, 1999.
- [118] D. S. Ragsdale, J. C. McPhee, T. Scheuer, and W. A. Catterall, "Molecular determinants of state-dependent block of Na<sup>+</sup> channels by local anesthetics.," *Science (80-. )*, vol. 265, no. 5179, pp. 1724–8, 1994.
- [119] D. S. Ragsdale, "How do mutant Nav1.1 sodium channels cause epilepsy?," *Brain Research Reviews*, vol. 58, no. 1, pp. 149–159, 2008.
- [120] A. M. Powl, A. J. Miles, and B. A. Wallace, "Synchrotron radiation circular dichroism spectroscopy-defined structure of the C-terminal domain of NaChBac and its role in channel assembly," *Proc. Natl. Acad. Sci.*, vol. 107, pp. 14064–14069, 2010.
- [121] J. Payandeh, T. Scheuer, N. Zheng, and W. A. Catterall, "The crystal structure of a voltage-gated sodium channel," *Nature*, vol. 475, no. 7356, pp. 353–358, 2011.
- [122] E. Pavlov, R. Winkfein, C. Diao, P. Dhaliwal, and R. J. French, "The pore, not cytoplasmic domains, underlies inactivation in a prokaryotic sodium channel," *Biophys. J.*, vol. 89, pp. 232–242, 2005.
- [123] D. M. Papazian, S. A. Seoh, A. F. Mock, Y. Huang, and D. H. Wainstock, "Electrostatic interactions of S4 voltage sensor in Shaker K<sup>+</sup> channel," *Neuron*, vol. 14, pp. 1293–1301, 1995.

- [124] D. Oliver, M. Soom, T. Baukrowitz, P. Jonas, and B. Fakler, "Functional conversion between A-type and delayed rectifier K<sup>+</sup> channels by membrane lipids," *Science (80-. )*, vol. 304, pp. 265–270, 2004.
- [125] G. Nurani, K. Charalambous, A. O. O'Reilly, N. B. Cronin, S. Haque, and B. A. Wallace, "Tetrameric bacterial sodium channels: characterization of structure, stability, and drug binding," *Biochemistry*, vol. 47, pp. 8114–8121, 2008.
- [126] M. Noda, H. Suzuki, H. Takeshima, T. Takahashi, M. Kuno, and S. Numa, "Expression of functional sodium channels from cloned cDNA," *Nature*, vol. 322, pp. 826–828, 1986.
- [127] M. Noda, Y. Furutani, H. Takahashi, M. Toyosato, T. Tanabe, S. Shimizu, S. Kikuyotani, T. Kayano, T. Hirose, S. Inayama, and S. Numa, "Cloning and sequence analysis of calf cDNA and human genomic DNA encoding  $\alpha$ -subunit precursor of muscle acetylcholine receptor," *Nature*, vol. 305, pp. 818–823, 1983.
- [128] J. C. Mulley, I. E. Scheffer, S. Petrou, L. M. Dibbens, S. F. Berkovic, and L. A. Harkin, "SCN1A mutations and epilepsy," *Human Mutation*, vol. 25, no. 6, pp. 535–542, 2005.
- [129] S. N. Misra, A. L. George, and Jr., "Impaired NaV1.2 function and reduced cell surface expression in benign familial neonatal-infantile seizures," *Epilepsia*, vol. 49, pp. 1535–1545, 2008.
- [130] K. Mio, F. Arisaka, M. Sato, and C. Sato, "The C-terminal coiled-coil of the bacterial voltage-gated sodium channel NaChBac is not essential for tetramer formation, but stabilizes subunit-to-subunit interactions," *Prog. Biophys. Mol. Biol.*, vol. 103, pp. 111–121, 2010.
- [131] S. B. Long, "Voltage Sensor of Kv1.2: Structural Basis of Electromechanical Coupling," *Science (80-. )*, vol. 309, no. 5736, pp. 903–908, 2005.
- [132] A. Kuzmenkin and A. M. Correa, "Gating of the Bacterial Sodium Channel, NaChBac Voltage-dependent Charge Movement and Gating Currents," *J. Gen. Physiol.*, vol. 124, pp. 349–356, 2004.
- [133] C. C. Kuo and L. Lu, "Characterization of lamotrigine inhibition of Na<sup>+</sup> channels in rat hippocampal neurones," *Br. J. Pharmacol.*, vol. 121, no. 6, pp. 1231–8, 1997.
- [134] K. J. Kontis and A. L. Goldin, "Sodium channel inactivation is altered by substitution of voltage sensor positive charges," *J. Gen. Physiol.*, vol. 110, no. 4, pp. 403–13, 1997.
- [135] R. Koishi, H. Xu, D. Ren, B. Navarro, B. W. Spiller, Q. Shi, and D. E. Clapham, "A Superfamily of Voltage-gated Sodium Channels in Bacteria," *J. Biol. Chem.*, vol. 279, no. 10, pp. 9532–9538, 2004.
- [136] Y. Jiang, J. Chen, M. Cadene, B. T. Chait, and R. MacKinnon, "The open pore conformation of potassium channels," *Nature*, vol. 417, pp. 523–526, 2002.
- [137] M. O. Jensen, D. W. Borhani, A. E. Leffler, R. O. Dror, and D. E. Shaw, "Mechanism of voltage gating in potassium channels," *Science (80-. )*, vol. 336, pp. 229–233, 2012.
- [138] M. Ito, H. Xu, A. A. Guffanti, Y. Wei, L. Zvi, D. E. Clapham, and T. A. Krulwich, "The voltage-gated Na<sup>+</sup> channel NaVBP has a role in motility, chemotaxis, and pH homeostasis of an alkaliphilic *Bacillus*," *Proc. Natl. Acad. Sci.*, vol. 101, no. 29, pp. 10566–10571, Jul. 2004.
- [139] L. L. Isom, K. S. De Jongh, D. E. Patton, B. F. Reber, J. Offord, H. Charbonneau, K. Walsh, A. L. Goldin, and W. A. Catterall, "Primary structure and functional expression of the beta 1 subunit of the rat brain sodium channel," *Science (80-. )*, vol. 256, no. 5058, pp. 839–842, 1992.
- [140] K. Irie, K. Kitagawa, H. Nagura, T. Imai, T. Shimomura, and Y. Fujiyoshi, "Comparative study of the gating motif and C-type inactivation in prokaryotic voltage-gated sodium channels," *J. Biol. Chem.*, vol. 285, no. 6, pp. 3685–3694, 2010.

- [141] A. L. Hodgkin and A. F. Huxley, "A Quantitative Description of Membrane Current and its Application to Conduction and Excitation in Nerves," *J. Physiol.*, vol. 117, pp. 500–544, 1952.
- [142] G. H. Hockerman, B. Z. Peterson, B. D. Johnson, and W. A. Catterall, "MOLECULAR DETERMINANTS OF DRUG BINDING AND ACTION ON L-TYPE CALCIUM CHANNELS," *Annu. Rev. Pharmacol. Toxicol.*, vol. 37, no. 1, pp. 361–396, 1997.
- [143] S. H. Heinemann, W. Stuhmer, K. Imoto, and S. Numa, "Calcium channel characteristics conferred on the sodium channel by single mutations," *Nature*, vol. 356, pp. 441–443, 1992.
- [144] Y. P. Goldberg, M. L. MacDonald, J. Thompson, M. P. Dube, M. Mattice, R. Fraser, C. Young, S. Hossain, T. Pape, B. Payne, C. Radomski, G. Donaldson, E. Ives, J. Cox, H. B. Younghusband, R. Green, A. Duff, E. Boltshauser, G. A. Grinspan, J. H. Dimon, B. G. Sibley, G. Andria, E. Toscano, J. Kerdraon, D. Bowsher, S. N. Pimstone, M. E. Samuels, R. Sherrington, and M. R. Hayden, "Loss-of-function mutations in the Nav1.7 gene underlie congenital indifference to pain in multiple human populations," *Clin Genet*, vol. 71, pp. 311–319, 2007.
- [145] S. Fujinami, T. Sato, J. S. Trimmer, B. W. Spiller, D. E. Clapham, T. A. Krulwich, I. Kawagishi, and M. Ito, "The voltage-gated Na<sup>+</sup> channel Na<sup>v</sup>BP co-localizes with methyl-accepting chemotaxis protein at cell poles of alkaliphilic *Bacillus pseudofirmus*," *Microbiology*, vol. 125, pp. 4027–4038, 2007.
- [146] G. Eisenman and R. Horn, "Ionic selectivity revisited: the role of kinetic and equilibrium processes in ion permeation through channels," *J. Membr. Biol.*, vol. 76, pp. 197–225, 1983.
- [147] T. Dudev and C. Lim, "Determinants of K<sup>+</sup> vs Na<sup>+</sup> Selectivity in Potassium Channels," *J. Am. Chem. Soc.*, vol. 131, no. 23, pp. 8092–8101, 2009.
- [148] D. A. Doyle, R. A. Pfuetzner, A. Kuo, J. M. Gulbis, S. L. Cohen, B. T. Chait, and R. MacKinnon, "The structure of the potassium channel: molecular basis of K<sup>+</sup> conduction and selectivity," *Science (80-. )*, vol. 280, pp. 69–77, 1998.
- [149] I. E. Dick, Y. Purohit, G. J. Kaczorowski, W. J. Martin, and B. T. Priest, "Sodium channel blockade may contribute to the analgesic efficacy of antidepressants," *J. Pain*, vol. 8, pp. 315–324, 2007.
- [150] S. D. Dib-hajj, J. A. Black, and S. G. Waxman, "Voltage-gated sodium channels: therapeutic targets for pain," *Pain Med.*, vol. 10, no. 7, pp. 1260–1269, 2009.
- [151] P. Delmas, B. Coste, N. Gamper, and M. S. Shapiro, "Phosphoinositide lipid second messengers: New paradigms for calcium channel modulation," *Neuron*, vol. 47, no. 2, pp. 179–182, 2005.
- [152] P. G. DeCaen, Y. Zhao, T. Scheuer, and W. A. Catterall, "Disulfide locking a sodium channel voltage sensor reveals ion pair formation during activation," *Proc. Natl. Acad. Sci.*, vol. 105, pp. 15142–15147, 2008.
- [153] P. G. DeCaen, V. Yarov-Yarovoy, E. M. Sharp, T. Scheuer, and W. A. Catterall, "Sequential formation of ion pairs during activation of a sodium channel voltage sensor," *Proc. Natl. Acad. Sci.*, vol. 106, no. 52, pp. 22498–22503, 2009.
- [154] P. G. DeCaen, V. Yarov-Yarovoy, T. Scheuer, and W. A. Catterall, "Gating charge interactions with the S1 segment during activation of a Na<sup>+</sup> channel voltage sensor," *Proc. Natl. Acad. Sci.*, vol. 108, no. 46, pp. 18825–18830, 2011.
- [155] M. De Curtis and G. Avanzini, "Interictal spikes in focal epileptogenesis," *Prog. Neurobiol.*, vol. 63, no. 5, pp. 541–567, 2001.

- [156] G. M. Clayton, L. Heginbotham, V. M. Unger, and J. H. Morais-Cabral, "Structure of the transmembrane regions of a bacterial cyclic nucleotide-regulated channel," *Proc. Natl. Acad. Sci.*, vol. 105, pp. 1511–1515, 2008.
- [157] D. M. Chernoff, "Kinetic analysis of phasic inhibition of neuronal sodium currents by lidocaine and bupivacaine," *Biophys. J.*, vol. 58, no. 1, pp. 53–68, 1990.
- [158] Z. Chen, C. Alcayaga, B. A. Suárez-Isla, B. O'Rourke, G. Tomaselli, and E. Marbán, "A 'minimal' sodium channel construct consisting of ligated S5-P-S6 segments forms a toxin-activatable ionophore," *J. Biol. Chem.*, vol. 277, no. 27, pp. 24653–24658, 2002.
- [159] X. Chen, F. Ni, and J. Ma, "Structure of the full-length Shaker potassium channel Kv1.2 by normal-mode-based X-ray crystallographic refinement," *Proc. Natl. Acad. Sci.*, vol. 107, pp. 11352–11357, 2010.
- [160] K. Charalambous and B. A. Wallace, "NaChBac: The long lost sodium channel ancestor," *Biochemistry*, vol. 50, no. 32, pp. 6742–6752, 2011.
- [161] W. A. Catterall, "Ion channel voltage sensors - structure function and pathophysiology," *Neuron*, vol. 67, pp. 915–928, 2010.
- [162] D. A. Beneski and W. A. Catterall, "Covalent labeling of protein components of the sodium channel with a photoactivable derivative of scorpion toxin," *Proc. Natl. Acad. Sci.*, vol. 77, no. 1, pp. 639–643, 1980.
- [163] C. Bagnéris, P. G. DeCaen, B. A. Hall, C. E. Naylor, D. E. Clapham, C. W. M. Kay, and B. A. Wallace, "Role of the C-terminal domain in the structure and function of tetrameric sodium channels," *Nat. Commun.*, vol. 4, p. 2465, 2013.
- [164] C. M. Armstrong and B. Hille, "Voltage-Gated Ion Channels Review and Electrical Excitability," *Neuron*, vol. 20, pp. 371–380, 1998.
- [165] C. M. Armstrong and F. Bezanilla, "Charge movement associated with the opening and closing of the activation-gates of the Na channels," *J. Gen. Physiol.*, vol. 63, pp. 533–552, 1974.
- [166] M. Akhtar and N. F. Goldschlager, "Brugada electrocardiographic pattern due to tricyclic antidepressant overdose," *J. Electrocardiol.*, vol. 39, no. 3, pp. 336–339, 2006.
- [167] G. Yellen, D. Sodickson, T. Y. Chen, and M. E. Jurman, "An engineered cysteine in the external mouth of a K<sup>+</sup> channel allows inactivation to be modulated by metal binding," *Biophys. J.*, vol. 66, no. 4, pp. 1068–1075, Jan. 1994.
- [168] L. Tang, T. M. Gamal El-Din, J. Payandeh, G. Q. Martinez, T. M. Heard, T. Scheuer, N. Zheng, and W. A. Catterall, "Structural basis for Ca<sup>2+</sup> selectivity of a voltage-gated calcium channel," *Nature*, vol. 505, no. 7481, pp. 56–61, Nov. 2013.
- [169] D. Shaya, F. Findeisen, F. Abderemane-Ali, C. Arrigoni, S. Wong, S. R. Nurva, G. Loussouarn, and D. L. Minor, "Structure of a Prokaryotic Sodium Channel Pore Reveals Essential Gating Elements and an Outer Ion Binding Site Common to Eukaryotic Channels," *J. Mol. Biol.*, vol. 426, no. 2, pp. 467–483, 2014.
- [170] K. Hemming, M. J. Maguire, J. L. Hutton, and A. G. Marson, "Vigabatrin for refractory partial epilepsy," in *Cochrane Database of Systematic Reviews*, K. Hemming, Ed. Chichester, UK: John Wiley & Sons, Ltd, 2013.

- [171] M. Colledge and B. A. Wallace, "AnglerFish: a webserver for defining the geometry of  $\alpha$ -helices in membrane proteins," *Bioinformatics*, vol. 16, p. btw781, Dec. 2016.
- [172] H. L. Zhu, R. D. Wassall, M. Takai, H. Morinaga, M. Nomura, T. C. Cunnane, and N. Teramoto, "Actions of veratridine on tetrodotoxin-sensitive voltage-gated Na<sup>+</sup> currents, NaV1.6, in murine vas deferens myocytes," *Br. J. Pharmacol.*, vol. 157, no. 8, pp. 1483–1493, 2009.
- [173] B. M. Bulheller, A. Rodger, and J. D. Hirst, "Circular and linear dichroism of proteins.," 2007.
- [174] J. C. Sutherland, "Measurement of circular dichroism and related spectroscopies with conventional and synchrotron light sources: Theory and instrumentation," *Adv. Biomed. Spectrosc.*, vol. 1, pp. 19–72, 2009.
- [175] J. Bürck, P. Wadhvani, S. Fanghänel, and A. S. Ulrich, "Oriented Circular Dichroism: A Method to Characterize Membrane-Active Peptides in Oriented Lipid Bilayers," *Acc. Chem. Res.*, vol. 49, no. 2, pp. 184–192, Feb. 2016.
- [176] H. H. J. De Jongh, E. Goormaghtigh, and J. A. Killian, "Analysis of Circular Dichroism Spectra of Oriented Protein–Lipid Complexes: Toward a General Application," *Biochemistry*, vol. 33, no. 48, pp. 14521–14528, Dec. 1994.
- [177] C. Bagneris, P. G. DeCaen, C. E. Naylor, D. C. Pryde, I. Nobeli, D. E. Clapham, and B. A. Wallace, "Prokaryotic NavMs channel as a structural and functional model for eukaryotic sodium channel antagonism," *Proc. Natl. Acad. Sci.*, vol. 111, no. 23, pp. 8428–8433, 2014.
- [178] H. Nury, C. Van Renterghem, Y. Weng, and A. Tran, "X-ray structures of general anaesthetics bound to a pentameric ligand-gated ion channel," *Nature*, vol. 469, pp. 428–431, 2011.
- [179] L. Czerski and C. R. Sanders, "Functionality of a Membrane Protein in Bicelles," *Anal. Biochem.*, vol. 284, no. 2, pp. 327–333, Sep. 2000.
- [180] J. Bürck, S. Roth, P. Wadhvani, S. Afonin, N. Kanithasen, E. Strandberg, and A. S. Ulrich, "Conformation and Membrane Orientation of Amphiphilic Helical Peptides by Oriented Circular Dichroism," *Biophys. J.*, vol. 95, no. 8, pp. 3872–3881, 2008.
- [181] H. M. Berman, J. Westbrook, Z. Feng, G. Gilliland, T. N. Bhat, H. Weissig, I. N. Shindyalov, and P. E. Bourne, "The Protein Data Bank.," *Nucleic Acids Res.*, vol. 28, no. 1, pp. 235–42, Jan. 2000.
- [182] B. Kozlikova, E. Sebestova, V. Sustr, J. Brezovsky, O. Strnad, L. Daniel, D. Bednar, A. Pavelka, M. Manak, M. Bezdeka, P. Benes, M. Kotry, A. Gora, J. Damborsky, and J. Sochor, "CAVER Analyst 1.0: graphic tool for interactive visualization and analysis of tunnels and channels in protein structures," *Bioinformatics*, vol. 30, no. 18, pp. 2684–2685, Sep. 2014.
- [183] O. S. Smart, J. G. Neduelil, X. Wang, B. A. Wallace, and M. S. P. Sansom, "HOLE: A Program for the Analysis of the Pore Dimensions of Ion Channel Structural Models," *J. Mol. Graph.*, vol. 14, no. 6, pp. 354–360, 1996.
- [184] W. A. Catterall, "From Ionic Currents to Molecular Mechanisms : The Structure and Function of Voltage-Gated Sodium Channels," *Neuron*, vol. 26, pp. 13–25, 2000.
- [185] X. Zhang, W. Ren, P. G. DeCaen, C. Yan, X. Tao, and L. Tang, "Crystal structure of an orthologue of the NaChBac voltage-gated sodium channel," *Nature*, 2012.
- [186] F. H. Yu and W. A. Catterall, "Overview of the voltage-gated sodium channel family.," *Genome Biol.*, vol. 4, no. 3, p. 207, 2003.

- [187] Y. Wu, H. W. Huang, and G. A. Olah, "Method of oriented circular dichroism," *Biophys. J.*, vol. 57, no. 4, pp. 797–806, 1990.
- [188] M. R. Yeaman and N. Y. Yount, "Mechanisms of antimicrobial peptide action and resistance," *Pharmacol. Rev.*, 2003.
- [189] D. Conte Camerino, D. Tricarico, and J.-F. Desaphy, "Ion Channel Pharmacology," *Neurotherapeutics*, vol. 4, no. 2, pp. 184–198, 2007.
- [190] K. M. Hillgren, D. Keppler, A. A. Zur, K. M. Giacomini, B. Stieger, C. E. Cass, and L. Zhang, "Emerging Transporters of Clinical Importance: An Update From the International Transporter Consortium," *Clin. Pharmacol. Ther.*, vol. 94, no. 1, pp. 52–63, Jul. 2013.
- [191] D. N. Langelaan, M. Wieczorek, C. Blouin, and J. K. Rainey, "Improved helix and kink characterization in membrane proteins allows evaluation of kink sequence predictors.," *J. Chem. Inf. Model.*, vol. 50, no. 12, pp. 2213–20, Dec. 2010.
- [192] A. Alam and Y. Jiang, "Structural analysis of ion selectivity in the NaK channel," *Nat. Struct. Mol. Biol.*, vol. 16, pp. 35–41, 2009.
- [193] N. Shi, S. Ye, A. Alam, L. Chen, and Y. Jiang, "Atomic structure of a Na<sup>+</sup>- and K<sup>+</sup>-conducting channel.," *Nature*, vol. 440, pp. 570–574, 2006.
- [194] L. Sanguet, Z. Fourati, T. Prang, M. Delarue, and N. Colloc'h, "Structural basis for xenon inhibition in a cationic pentameric ligand-gated ion channel," *PLoS One*, vol. 11, no. 2, 2016.
- [195] E. C. McCusker, C. Bagn eris, C. E. Naylor, A. R. Cole, N. D'Avanzo, C. G. Nichols, and B. A. Wallace, "Structure of a bacterial voltage-gated sodium channel pore reveals mechanisms of opening and closing," *Nat. Commun.*, vol. 3, p. 1102, 2012.
- [196] Y. Arinaminpathy, E. Khurana, and D. M. Engelman, "Computational analysis of membrane proteins: the largest class of drug targets," *Drug Discov. Today*, 2009.